Numerical analyses of frictional sliding on rate-and-state interfaces: Fluid effects, dynamic weakening, and potential-based formulation through machine learning

Thesis by
Shengduo Liu

In Partial Fulfillment of the Requirements for the
Degree of
Doctor of Philosophy in Mechanical Engineering

Caltech

CALIFORNIA INSTITUTE OF TECHNOLOGY
Pasadena, California

2025
Defended July 26, 2024

ACKNOWLEDGEMENTS

Thank you to everyone who has made my PhD journey possible.

First and foremost, I would like to express my deepest gratitude to my thesis advisors, Prof. Nadia Lapusta and Prof. Kaushik Bhattacharya. Their continued guidance, expertise, and natural curiosity have provided me with a mentor and motivation to grow as a researcher. My study at Caltech could not have even started five years ago without Nadia's tremendous support as the option representative, when I was stuck in China for months waiting for my visa to be approved. Through my work with Nadia, I have not only learned the technical aspects of computational modeling of complicated physical processes, but also how to think, explore and deal with unexpected difficulties and challenges, both in research projects and more broadly in life. Nadia always gives me insightful advice when I am faced with any challenge to take or decision to make during my PhD, and has been always supportive to what I wanted to explore in different fields of science. Through my work with Kaushik, I have not only learned advanced mathematics and how to apply it to hard problems in mechanics, but also how to keep challenging myself with bigger steps into unfamiliar areas during research. Kaushik has inspired me and helped me develop confidence on my ability to learn about and explore different fields, including mathematics, deep learning, etc. I am grateful for this time working with Nadia and Kaushik, which has shaped me into a better researcher, and more importantly, a better person.

I am also thankful to my thesis committee members, Prof. Guruswami Ravichandran, and Prof. Ruby Fu, for their generous time, valuable feedback, and academic advice.

I have been fortunate to work with wonderful collaborators: Dr. Elias Heimisson, Dr. Vito Rubino, Prof. Ares Rosakis, Dr. Brad Aagaard, and Dr. Taeho Kim. Elias together with Nadia first introduced me into the world of boundary integral methods applied to geophsyical problems, and was always there to offer help when I was stuck at various issues regarding coding, processing data, and writing. Vito and Ares have taught me the fundamentals of laboratory earthquakes, Brad introduced me to a community opensource software PyLith, which was a wonderful starting point for my computational modeling of laboratory earthquakes. Taeho and I have had many inspiring discussions during my PhD and he has taught me a lot about earth sciences. Taeho also has provided experimental and numerical fitting data of rate-and-state friction for my machine-learning project as a comparison.

I would like to thank the Caltech music program, especially my piano professor Robert Ward and the choral director Nancy Sulahian, for providing me with many generous opportunities to play piano and sing, which would have been impossible to do on my own.

I would like to thank all members of the Lapusta and Bhattacharya groups for the countless discussions and collaborations throughout the years. Many thanks to my friends and current/former office-mates Vatsa Gandhi, Andrew Akerson, Eric Ocegueda, Sathvik Sanagala, Aakila Rajan, Barry Lawlor, Adeline Wihardja, Mary Agajanian, Carter Cocke, Mayank Raj, Theresa Tsaggaris, Maximo Cravero Baraja, and Taeho Kim for keeping the office a fun place I always looked forward to, along with our food, snacks, and games.

Finally, I am extremely thankful to my girlfriend, Dr. Yuan Yao, and my parents (Haiyan Yu and Wenbin Liu), for their unconditional support and encouragement over the peaks and valleys of my life.

ABSTRACT

Rate-and-state friction formulations have been widely used to reproduce a number of observations on faulting in the earth's crust, including earthquake nucleation, creeping fault segments, dynamic earthquake rupture, aftershock sequences, and episodic slow slip events. The formulations have also been used to explain the motion of landslides and glaciers. In this thesis, we use numerical simulations to study various factors that can affect the stability of fault slip with rate-and-state friction, including poroelastic bulk properties and dilatation/compaction of the fault material in the presence of fluids, fault healing, injection rate when there is fluid injected into the fault, as well as dynamic weakening of the fault gouge. We also seek to optimize simulations with rate-and-state friction by developing a potential-based formulation using machine learning.

First, we study the stability of frictional fault slip in the presence of fluids, with a focus on fault loading due to fluid injection into the fault as done in many field and laboratory experiments. In Chapter 2, we present a boundary-integral approach on simulating frictional fault slip in a permeable shear layer surrounded by poroelastic bulk. The approach is then used to explore the effects of poroelasticity and inelastic dilatancy on the stability of frictional fault slip in a fluid-injection problem. We find that the diffusion into and poroelastic properties of the bulk can significantly stabilize fault slip, with the stabilization by bulk diffusion and poroelastic properties comparable to the well-known stabilizing effects of the dilatancy mechanism.

In Chapter 3, we further develop the boundary integral code to allow for purely elastic bulk with the same fluid transport properties as the poroelastic bulk material and consider the effect of fault healing and fluid injection rate on fault slip. We show that the poroelastic bulk effects can be very closely captured by using the undrained value of Poisson's ratio in an elastic bulk model with the same fluid mass diffusivity of the bulk. We find that fault healing significantly delays the onset of dynamic slip events and restricts their spatial extent, making the initial response of the fault to fluid injection much different than its longer-term response. While this is an expected conclusion, fault healing is not typically accounted for in fluid-injection modeling which often uses simpler slip-dependent friction laws. We also find that faster or intermittent injection rates lead to more frequent but more spatially constrained dynamic slip events, for the same injected fluid mass, motivating further investigations into injection strategies that would optimize fault stability.

Second, in Chapter 4, we numerically simulate a laboratory experiment of spontaneous dynamic rupture by developing a 3D finite-element model of the experiment with rate-and-state friction. In the experiment, a dynamic rupture is initiated on a Homalite-100 interface and then produces an intermittent slip in the rock gouge embedded into a part of the interface. Our simulations show that the laboratory findings are consistent with rock gouge which is rate-strengthening at low slip rates but dynamically weakening at high slip rates through the mechanism similar to flash heating. However, to fit the experimental results, the traditional flash-heating formulation needs to be substantially modified, potentially due to effects of localization and delocalization of slip in the rock gouge.

The third part of the thesis focuses on identifying a potential-based formulation for the rate-and-state friction laws. Due to their empirical derivation, the rate-and-state friction laws cannot be written as the gradients of a potential, which leads to difficulties in implicit solution of dynamic frictional problems. In Chapter 5, we present a potential-based formulation for the rate-and-state friction law through Neural Network approximation and training on datasets generated by a one-degree-of-freedom spring-slider system with the rate-and-state friction law. The learnt potential is able to reproduce the results with rate-and-state friction law, and indeed facilitates an implicit solution of dynamic problems. However, the training of the potential requires a much larger dataset than fitting the original rate-and-state friction law.

Overall, our modeling significantly advances our understanding of the factors that control stability of frictional sliding on natural faults and suggests promising machine-learning directions in replacing the empirical rate-and-state formulations with the ones based on thermodynamic potentials.

PUBLISHED CONTENT AND CONTRIBUTIONS

[1] E. R. Heimisson, S. Liu, N. Lapusta, and J. Rudnicki. "A Spectral Boundary-Integral Method for Faults and Fractures in a Poroelastic Solid: Simulations of a Rate-and-State Fault With Dilatancy, Compaction, and Fluid Injection." In: *Journal of Geophysical Research: Solid Earth* 127.9 (2022). DOI: `10.1029/2022JB024185`.

S.L. participated in checking and revising the original code developed by E.H., designed the examples of fluid injection, ran the simulations of fluid injection into faults with different dilatancy and poroelastic properties, etc., postprocessed results of the simulations, and made the figures for the simulation results.

TABLE OF CONTENTS

LIST OF ILLUSTRATIONS

LIST OF TABLES

Chapter 1

INTRODUCTION

1.1 Numerical modeling of frictional fault slip

Frictional fault slip is the key process of many geological activities, including slow slip events and dynamic earthquakes. Understanding the underlying physics of such frictional fault slip is important for predicting seismic hazards and preventing destructive induced earthquakes during industrial activities. Since it is usually difficult to conduct direct measurements through probing near geological faults, it is important to develop numerical modeling tools of frictional fault slip, which will help scientists verify their hypothesis and conjectures through numerical simulations with specific physical laws. In this thesis, we focus on two important problems of frictional fault slip. We first present our numerical modeling for frictional fault slip in the presence of fluids, which has wide applications in industry. Second, we focus on developing a numerical modeling method for frictional slip through fault gouge, a special interface material made up of particles that has significant dynamic weakening mechanism when undergoing high slip rate frictional sliding. Finally, we discuss a potential formulation for the original rate-and-state friction law that facilitates implicit solution of dynamic problems associated.

Frictional fault slip in the presence of fluids

Modeling of frictional fault slip in the presence of fluids has applications in a lot of geophysical problems, notably in the realms of earthquake mechanics, sequestration of CO_2, and extraction of geothermal energy. Understanding the dynamics of fault slip is essential for predicting seismic hazards and avoiding destructive induced seimicities during industrial activities. One key framework for modeling fault slip behavior is the rate-and-state friction (RSF) law, which characterizes the frictional resistance of a fault as a function of slip rate and the evolving state of the fault surface [9, 23, 17, 26]. The RSF law captures the complexities of both the direct effect once slip rate suddenly changes, and the evolution effect as fault slip accumulates afterwards, and with four parameters, the RSF law is capable of explaining the experimental results of stable and unstable frictional fault slip [17, 19].

Fluids play an important role in modulating fault slip by changing the effective normal stress through pore pressure changes [13, 5, 11]. Elevated pore fluid pressure can reduce the effective normal stress, potentially triggering slip on pre-existing faults. This mechanism is a primary concern in fluid injection activities, such as hydraulic fracturing, wastewater disposal, and geothermal energy extraction, which have been associated with induced seismicity [12, 10, 27, 6].

The poroelastic response of the bulk material surrounding a fault is also a critical factor in determining the slip behavior under fluid injection. Poroelasticity, the coupling of fluid flow and mechanical deformation, is described by Biot's theory [3], and has been applied to various geophysical problems [20, 22]. Poroelastic effects can lead to complicated interactions between fluid pressure diffusion and fault slip, influencing both the spatial and temporal patterns of induced seismicity.

In some previous studies, the bulk material surrounding geological faults has been modeled using linear elasticity, and fluid diffusion is assumed to be within the fault shear layer only. This approach has been employed to investigate the fundamental aspects of fault slip and stress transfer [18, 25, 14]. These models provide valuable insights, but may overlook critical solid-fluid interactions that are significant in poroelastic surrounding bulk, whose existence is non-negligible around pre-existing faults with large historic slip.

A previous study by Healy et al. [12] on the Denver earthquakes first highlighted the potential for fluid injection to induce seismicity. Subsequent studies, such as Ellsworth [10], have further elucidated the mechanisms by which fluid pressure changes can trigger fault slip. Laboratory experiments have also contributed significantly to our understanding, with Dieterich [9] and Ruina [23] establishing the foundational rate-and-state friction laws. These laws have been applied to various fault slip scenarios, including those induced by fluid injection [17, 26].

The interplay between fluid pressure and frictional fault slip has been explored in numerous studies. Hubbert and Rubey [13] provided early theoretical insights into the role of fluid pressure in fault mechanics, while Byerlee [5] and Marone [17] offered empirical evidence from rock friction experiments. More recent work by Guglielmi et al. [11] has demonstrated the triggering of seismicity by fluid-induced aseismic slip, underscoring the importance of pore pressure changes in the stability of fault slip.

Theoretical advancements have been complemented by numerical models that incorporate poroelastic effects. Rice and Cleary [20] and Rudnicki [22] provided early theoretical frameworks for poroelasticity, which have been further developed and applied to induced seismicity by Segall [28] and Cappa and Rutqvist [6]. These models account for the diffusion of pore pressure and its impact on fault slip, offering insights into the temporal and spatial evolution of induced seismicity.

In summary, the study of frictional fault slip in the presence of fluids involves a complex interplay of mechanical and hydraulic processes. The rate-and-state friction framework, combined with poroelastic modeling, provides an approach for physically understanding and predicting fault slip behavior under fluid injection.

Laboratory earthquakes propagating through fault gouge

Understanding the mechanics of earthquakes and fault slip is vital for mitigating seismic hazards, and laboratory experiments have been instrumental in advancing this knowledge. In particular, fault gouge, the finely ground rock material found within fault zones, plays a crucial role in earthquake propagation. The mechanical behavior of fault gouge is affected by various factors, including pressure, temperature, and the presence of fluids. Early studies, such as Marone1998, highlighted the frictional properties of fault gouge and its influence on fault slip stability. Subsequent research by Beeler et al. [1] demonstrated how higher pressures and temperatures could stabilize fault slip, while Di Toro, Goldsby, and Tullis [7] showed that high-velocity friction experiments could replicate dynamic weakening mechanisms in fault gouge, leading to unstable slip and earthquake propagation. Other notable contributions include the work of Brantut et al. [4], which examined the role of fluid saturation in reducing friction and enhancing slip propagation, and Samuelson, Elsworth, and Marone [24], which focused on the microstructural evolution of fault gouge during slip, emphasizing the importance of grain size reduction and comminution processes.

In this thesis, motivated by the recent study by Rubino, Lapusta, and Rosakis [21], which provides insightful experimental results of slip rate along the fault gouge during a laboratory earthquake, through detailed Digital-Image-Correlation measurement. Building on previous studies, their experimental setup involved a biaxial shear apparatus designed to replicate fault slip under controlled conditions. This apparatus allowed for the precise application of normal and shear stresses, simulating realistic fault conditions. The dynamic fault slip was triggered by bursting a electronic wire on the frictional interface, mimicking the conditions of dynamic earthquake rupture. Additionally, high-speed cameras were employed to capture and analyze the slip over the fault gouge during slip events through DIC, providing valuable real-time data on fault slip in the gouge zone.

Rubino et al. (2022) reported several key findings from their experiments. They observed that dynamic ruptures arrive into the fault gouge at speeds similar to shear wave speed. Their also found the first rupture of the fault gouge, leading to stress concentrations. The acoustic emissions recorded during slip events correlated with the onset and propagation of dynamic ruptures, suggesting a potential method for real-time monitoring of fault slip in natural settings. Furthermore, they identified thermal pressurization as a critical weakening mechanism during high-speed slip, where rapid temperature increases within the fault gouge reduced friction and facilitated slip propagation. These findings underscore the importance of fault gouge properties in controlling the dynamics of earthquake rupture and suggest that similar mechanisms may operate in natural fault zones.

Despite these advancements, there is a continued need for numerical modeling to complement laboratory experiments in understanding the propagation of earthquakes through fault gouge. Numerical models can help simulate a broader range of conditions and parameters that are challenging to replicate in the laboratory. They allow researchers to examine their hypothesis and conjectures for the underlying physics that governs the frictional behavior of the fault gouge. Better understanding of frictional fault slip over fault gouge with numerical modeling will in the long term enhance our ability to predict and mitigate the impacts of natural earthquakes, ultimately contributing to safer and more resilient communities.

Difficulties with implicit solution of rate-and-state friction

Since the rate-and-state friction law was originally derived empirically from laboratory experiments [9, 8, 16], the friction formulation as well as the evolution law cannot be obtained from taking the gradient of a scalar function, i.e., a potential. This can lead to difficulties in implicit solution of dynamic problems that involves rate-and-state friction law. With a potential formulation of rate-and-state friction, the incremental implicit solution of dynamic problems can be written as convex minimization problems, which have unique solutions and are usually computationally easy to solve.

To find appropriate potentials that behaves similarly enough to the original rate-and-state friction law, one way is to construct them as Recurrent Neural Operators (RNOs) [15, 2]. RNOs are fundamentally Neural Networks (NNs) that represent the right-hand-side of typical Ordinary Differential Equations (ODEs). They are powerful tools for modeling of history-dependent time sequences because of their excellent fitting capabilities and independence of time stepping. By applying the idea of RNOs, we aim to find the potentials corresponding to the rate-and-state friction law, which are able to capture the rate-and-state dependent features obserations, and the same.

1.2 Research objectives

Here we present three major research studies that attempt to solve various numerical modeling problems of frictional fault slip. In the first study included in Chapters 2 and 3, we focus on developing a Boundary Integral code that can simulate frictional fault sliding under plane-strain condition, with rate-and-state friction and poroelastic or elastic permeable bulk material surrounding the fault. we would like to investigate the effects of poroelastic bulk, inelastic dilatancy of the fault shear layer, extent of fault healing, or the initial slip rate over the fault, fluid diffusivities both within the shear layer and the bulk material, injection rate as a function of time on the stability of frictional fault slip. Moreover, we would like to identify a strategy of controlling the rate of fluid-injection such that the instability of the fault slip is minimized, and thus we minimize the destruction potentially caused by the injection.

In the second study presented by Chapter 4, we explore the numerical modeling of intermittent laboratory earthquakes propagating into fault gouge zone, which has not only rate-and-state frictional behavior but also dynamic weakening mechanism associated. We would like to develop a 3D finite element model for the laboratory experiment, and explore what frictional formulation of the fault gouge can reproduce the experimental observation of first arresting the rupture, while then allows for the propagation of another rupture the gouge zone. This study also aims to find a physical dynamic weakening rate-and-state friction model, such that self nucleation within the gouge zone can spontaneously occur after the first rupture arrives and gets arrested.

In the third study included in Chapter 5, we aim to find a potential formulation for the rate-and-state friction that can transform the incremental implicit solution of a dynamic problem into a convex minimization problem. We would like to construct the potentials using Recurrent Neural Operators and train them on sequences generated by the original rate-and-state friction law. We testify how well they can capture the rate-and-state dependencies of friction comparing with the original rate-and-state friction law, and whether or not the trained potentials actually facilitate implicit solution of dynamic problems.

Finally in Chapter 6, we conclude with a summary of results and contributions toward modeling and studying the stability of frictional fault slip with rate-and-state friction, as well as a newly proposed potential formulation of rate-and-state friction that facilitates implicit solution of dynamic problems. Lastly, we provide some suggestions for future work relevant to the studies we have presented in this thesis.

References

[1] N. M. Beeler et al. "Constitutive relationships and physical basis of fault strength due to frictional heating." In: *Journal of Geophysical Research: Solid Earth* 113.B1 (2008), B01401. DOI: `10.1029/2007JB004988`.

[2] K. Bhattacharya et al. "Learning Markovian homogenized models in viscoelasticity." In: *Multiscale Modeling & Simulation* 21.2 (2023), pp. 641–679. DOI: `10.1137/22M1499200`. eprint: `https://doi.org/10.1137/22M1499200`.

[3] M. A. Biot. "General theory of three-dimensional consolidation." In: *Journal of Applied Physics* 12.2 (1941), pp. 155–164. DOI: `10.1063/1.1712886`.

[4] N. Brantut et al. "High-velocity frictional properties of a clay-bearing fault gouge and implications for earthquake mechanics." In: *Journal of Geophysical Research: Solid Earth* 113.B10 (2008). DOI: `10.1029/2007JB005551`.

[5] J. D. Byerlee. "Friction of rocks." In: *Pure and Applied Geophysics* 116.4-5 (1978), pp. 615–626. DOI: `10.1007/BF00876528`.

[6] F. Cappa and J. Rutqvist. "Modeling of coupled deformation and permeability evolution during fault reactivation induced by deep underground injection of CO2." In: *International Journal of Greenhouse Gas Control* 5.2 (2011), pp. 336–346. DOI: `10.1016/j.ijggc.2010.08.005`.

[7] G. Di Toro, D. L. Goldsby, and T. E. Tullis. "Friction falls toward zero in quartz rock as slip velocity approaches seismic rates." In: *Nature* 427.6973 (2004), pp. 436–439. DOI: `10.1038/nature02249`.

[8] J. Dieterich. "Potential for geophysical experiments in large-scale tests." In: *Geophysical Research Letters* 8.7 (1981), pp. 653–656. ISSN: 0094-8276. DOI: `10.1029/GL008i007p00653`.

[9] J. H. Dieterich. "Modeling of rock friction: 1. Experimental results and constitutive equations." In: *Journal of Geophysical Research: Solid Earth* 84.B5 (1979), pp. 2161–2168. DOI: `10.1029/JB084iB05p02161`.

[10] W. L. Ellsworth. "Injection-induced earthquakes." In: *Science* 341.6142 (2013), p. 1225942. DOI: `10.1126/science.1225942`.

[11] Y. Guglielmi et al. “Seismicity triggered by fluid injection–induced aseismic slip.” In: *Science* 348.6240 (2015), pp. 1224–1226. DOI: `10.1126/science.aab0476`.

[12] J. H. Healy et al. “The Denver earthquakes.” In: *Science* 161.3848 (1968), pp. 1301–1310. DOI: `10.1126/science.161.3848.1301`.

[13] M. K. Hubbert and W. W. Rubey. “Role of fluid pressure in mechanics of overthrust faulting: I. Mechanics of fluid-filled porous solids and its application to overthrust faulting.” In: *Geological Society of America Bulletin* 70.2 (1959), pp. 115–166. DOI: `10.1130/0016-7606(1959)70[115:ROFPIM]2.0.CO;2`.

[14] S. Larochelle et al. “Constraining Fault Friction and Stability With Fluid-Injection Field Experiments.” In: *Geophysical Research Letters* 48.10 (2021). DOI: `10.1029/2020GL091188`.

[15] B. Liu et al. “Learning macroscopic internal variables and history dependence from microscopic models.” In: *Journal of the Mechanics and Physics of Solids* 178 (2023), p. 105329. ISSN: 0022-5096. DOI: `10.1016/j.jmps.2023.105329`.

[16] C. Marone. “Laboratory-derived friction laws and their application to seismic faulting.” In: *Annual Review of Earth and Planetary Sciences* 26 (1998), pp. 643–696. ISSN: 0084-6597. DOI: `10.1146/annurev.earth.26.1.643`.

[17] C. Marone. “Laboratory-derived friction laws and their application to seismic faulting.” In: *Annual Review of Earth and Planetary Sciences* 26.1 (1998), pp. 643–696. DOI: `10.1146/annurev.earth.26.1.643`.

[18] Y. Okada. “Internal deformation due to shear and tensile faults in a half-space.” In: *Bulletin of the Seismological Society of America* 82.2 (1992), pp. 1018–1040. DOI: `10.1785/BSSA0820021018`.

[19] J. Rice and A. Ruina. “Stability of steady friction slipping.” In: *Journal of Applied Mechanics-Transactions of the ASME* 50.2 (1983), pp. 343–349. ISSN: 0021-8936. DOI: `10.1115/1.3167042`.

[20] J. R. Rice and M. P. Cleary. “Some basic stress diffusion solutions for fluid-saturated elastic porous media with compressible constituents.” In: *Reviews of Geophysics* 14.2 (1976), pp. 227–241. DOI: `10.1029/RG014i002p00227`.

[21] V. Rubino, N. Lapusta, and A. J. Rosakis. “Intermittent lab earthquakes in dynamically weakening fault gouge.” In: *Nature* 606.7916 (June 2022), pp. 922–929. DOI: `10.1038/s41586-022-04749-3`.

[22] J. W. Rudnicki. “Fluid mass sources and point forces in linear elastic diffusive solids.” In: *Mechanics of Materials* 5.4 (1986), pp. 383–393. DOI: `https://doi.org/10.1016/0167-6636(86)90042-6`.

[23] A. Ruina. “Slip instability and state variable friction laws.” In: *Journal of Geophysical Research: Solid Earth* 88.B12 (1983), pp. 10359–10370. DOI: `10.1029/JB088iB12p10359`.

[24] J. Samuelson, D. Elsworth, and C. Marone. “Influence of dilatancy on the frictional constitutive behavior of a saturated fault zone under a variety of drainage conditions.” In: *Journal of Geophysical Research: Solid Earth* 116.B10 (2011). DOI: `https://doi.org/10.1029/2011JB008556`.

[25] J. C. Savage. “A dislocation model of strain accumulation and release at a subduction zone.” In: *Journal of Geophysical Research: Solid Earth* 88.B6 (1983), pp. 4984–4996. DOI: `10.1029/JB088iB06p04984`.

[26] C. H. Scholz. “Earthquakes and friction laws”. In: *Nature* 391.6662 (1998), pp. 37–42. DOI: `10.1038/34097`.

[27] P. Segall and S. Lu. “Injection-induced seismicity: Poroelastic and earthquake nucleation effects.” In: *Journal of Geophysical Research: Solid Earth* 120.7 (2015), pp. 5082–5103. DOI: `https://doi.org/10.1002/2015JB012060`.

[28] P. Segall. “Earthquakes triggered by fluid extraction.” In: *Geology* 17.10 (1989), pp. 942–946. DOI: `10.1130/0091-7613(1989)017<0942:ETBFE>2.3.CO;2`.

Chapter 2

A SPECTRAL BOUNDARY-INTEGRAL METHOD FOR FAULTS AND FRACTURES IN A POROELASTIC SOLID: SIMULATIONS OF A RATE-AND-STATE FAULT WITH DILATANCY, COMPACTION, AND FLUID INJECTION

2.1 Introduction

The role of fluids in seismic and aseismic faulting processes has been of significant interest in the last few years. Mounting evidence indicates that fluids may play an important role in a diverse set of mechanisms that alter fault slip behavior ranging from earthquake triggering to slow slip events.

The most prominent example of fluid and fault interactions is the clear link between fluid injection and induced seismicity, as originally pointed out by [49, 35] and remains a critical issue [25]. This phenomenon has a straightforward mechanical explanation: higher pore pressures, due to injection, reduce the effective normal stress and thus the frictional resistance of the fault. This causes increased slip rate on faults and may accelerate the generation of seismic instabilities. This problem has been frequently modeled with a straightforward implementation of one-way coupling of pore pressure and frictional strength where pore pressure perturbations are imposed and slip or number of seismic events are computed.

The coupling injection and fault slip is far from trivial, for example, injection into faults may also lead to sustained aseismic transients [69, 3, 22], which may trigger microseismicity [29, 71]. The aseismic slip itself may later become seismic depending on the frictional properties of the fault [38]. A more detailed investigation of this problem reveals considerable complexity in pore pressure evolution if heterogeneous permeability structures and poroelasticity are considered [73]

The poroelastic properties of the crust have lately been receiving more interest, most prominently as a long-ranging and fast-acting mechanism in which faults can be stressed due to injection or extraction [58]. However, there is also significant literature on the role of poroelasticity in influencing the nucleation or propagation of seismic and aseismic ruptures [53, 24, 36, 33, 34]. An effect of particular importance in regard to the influence of poroelasticity is that, during in-plane sliding, compression and dilation of the host rock induces pore pressure change in the shear zone [33, 34]; this effect is discussed further in Section 4.2. Thus the poroelastic response of the bulk, induced by an ongoing rupture, may influence the effective normal stress and hence shear resistance to the rupture, creating a feedback loop. Poroelasticity also influences and introduces a diffusion-dependent time-evolving shear stress on the fault plane with significant implications for the stability of sliding [34].

Processes other than poroelasticity may change pore pressure in an active shear zone and affect rupture and instability formation on faults. The generation of aseismic slip transients on faults is believed to be related to pore fluids. For example, transient slow slip events (SSEs) in subduction zones are thought to be related to high pore pressure conditions [41, 9]. A primary challenge in explaining the mechanics of transient slow slip is to understand why it starts, but does not become an earthquake. One potential mechanism is a geometric restriction, in which the high-pore-pressure region is large enough to cause slip acceleration, for example, due to rate-and-state velocity-weakening friction properties, but too small for that slip to become seismic [40, 41]. Another potential explanation is the change from velocity-weakening to velocity-strengthening friction with increasing slip rates [63, 30, 39]. Rate-and-state faults with velocity-strengthening friction and additional destabilizing effects can also produce SSEs in models with poroelasticity [33] and viscoplasticity [65]. Inelastic dilatancy of granular fault gouge [44, 48] can lead to a reduction in pore pressure and stabilize fault slip. This is a naturally present fluid-related mechanism that can explain how slow slip transients do not evolve into seismic events [60, 62]. Modeling of fault slip with inelastic dilatancy can explain many properties of slow slip events, including their scaling [19]. Dilatant behavior of rocks acts at many scales and does not just affect fine scale granular gouge, but for example larger scale brittle rock masses may undergo inelastic deformation [7]. Here we focus on in-elastic dilatancy of gouge and large scale elastic volumetric changes in the bulk.

Multiple mechanisms may act at a time. Recently, numerical simulations have started exploring the simultaneous injection and inelastic dilatancy in a diffusive shear zone [16, 72]. However, these efforts have been limited to a non-diffusive and elastic bulk. Coupling with a poroelastic bulk introduces another degree of complexity, where elastic dilation and compression of the bulk generate pore pressure transients. Further complexity is introduced by field observations indicating that permeability of the shear zone in a fault core may be very different from the surrounding damage zone and host rock [70]. In addition, the shearing of gouge material can dramatically reduce the permeability perpendicular to the shearing direction and thus result in the shear zone having a significantly anisotropic permeability [74].

When slip speed becomes high enough in a narrow enough shear layer with small enough permeability, then thermal pressurization of pore fluids due to shear heating may also become important, e.g., [52, 6]. While such effects may be critical for seismic rupture evolution [46], they may be negligible or at least much less pronounced in the nucleation phases of the seismic cycle [61, 59], which are primarily the focus of this study. Consequently, we do not account for thermal pressurization, although it can be added to the model and numerical implementation developed here, e.g., following the approach of [47].

A number of authors have presented dislocation solutions and boundary integral formulations for poroelasticity [51, 15, 14, 13, 64]. While these solutions have useful applications to fracture and faulting problems, they generally have not been formulated to account for processes where pressure inside the fracture or on the frictional surface may change. This limits applicability to a certain class of problems.

Here we present a spectral boundary-integral method (SBIM) and derive novel analytical spectral boundary integral solutions appropriate for faulting and induced seismicity problems in a poroelastic bulk where pressure inside a thin shear zone could be changing. The SBIM allows us to simulate quasi-dynamic slow and fast slip on a rate-and-state fault with dilatancy/compaction and fluid flow in a plane-strain poroelastic medium. We take a boundary layer approach where the outer solution, which is the spectral representation of the poroelastic bulk, treats the fault as a zero-thickness interface with suitable boundary conditions. However, the inner solution considers the fault to be a finite-width shear zone. We consider the frictional properties of the shear zone to be determined by their width-averaged properties. The bulk is an isotropic standard quasi-static Biot poroelastic solid with a hydraulic diffusivity c. The shear zone has frictional strength described by rate-and-state friction, with inelastic state-dependent dilatancy and compaction and anisotropic permeability: the permeability across the shear zone is different than the permeability along the shear zone. The inelastic state-dependent dilatancy and compaction of the shear zone are implemented using the [60] approach, as explained later. We frequently refer to this process only as "dilatancy" for the sake of brevity, and that is also how it is commonly referred to in the fault mechanics community. However, we remind the reader that the "dilatancy" law also predicts compaction under certain conditions. The pore pressure in the layer is simplified and assumed to be bi-linear where the two linear profiles are continuous at the center of the shear zone as in [34][see also Section 4.2]. The spectral representation uses analytical convolution kernels, which are truncated for efficiency similar to [37], but at time scales relevant for the bulk diffusion at the specific wavenumber.

Heimisson, Rudnicki, and Lapusta [34] presented an analytical and scaling analysis of a dilatant fault in a poroelastic medium under long terms steady-state loading, thus exploring the stability of such faults in the context of spontaneous event nucleation at steady-sliding conditions. That analysis was achieved by a linearized stability analysis around steady state and provided useful first-order insights into governing parameters of fault stability. Here we solve a much more general problem numerically, by developing a method that allows us to efficiently simulate the fully nonlinear response of such faults. For example, we can simulate fault response due to injection into the fault in a fully coupled manner, where we account for anisotropic shear zone diffusion, in-elastic dilatancy, coupling of shear zone and bulk, poroelastic response from fault leak-off into the bulk, and pore pressure coupling of slip. To date, such a multifaceted description of the fluid fault interaction problem has not been presented in an efficient boundary integral framework.

The paper first discusses the general problem setup (Section 4.2). There we touch on the general features of the SBIM. In Section 2.3, a more mathematically rigorous description is presented. In Section 2.3, we provide the analytical spectral boundary-integral solutions for sliding and opening of an interface in a plane-strain poroelastic solid. The numerical approach taken to solve the coupled problem with dilatancy, compaction, and injection in a poroelastic solid is described in Section 2.4, where we first discuss the inversion of the Fourier transform by introducing a spectral basis and then convolution truncation. We show an application of the SBIM (Section 2.5), where we use constraints from a field experiment [29] and a recent numerical study that modeled the field experiment data [38]. Section 2.6 contains a discussion on the role of poroelasticity, and other fluid-based mechanisms, in the dynamics of injection-induced seismic and aseismic slip. Finally the Appendix contains details on parameters choices (A), the time-stepping algorithm (B), and numerical method validation (C).

Problem description

The general problem setup can be divided into three domains. Two are isotropic poroelastic half-spaces, which we call the bulk, one in $y > \epsilon$ region and the other in $y < -\epsilon$ region. The third is a shear zone made from fault gouge, which separates the two half-spaces (Figure 2.1a). The two poroelastic half-spaces are assumed to have the same material properties, which we characterize with the shear modulus G, Skempton's coefficient B, drained Poisson's ratio ν, undrained Poisson's ratio ν_u, and hydraulic diffusivity c [12, 20, 51]. In some cases, other poroelastic parameters may be displayed for compactness, legibility, and intuition. However, the implementation of the method we present uses the aforementioned five.

Between the two poroelastic half-spaces is the third domain that we call the shear zone ($-\epsilon < y < \epsilon$). We do not consider the shear zone to be specifically a poroelastic material, but rather fluid-filled frictional elasto-plastic granular gouge. The elastic behavior of the shear zone is described with various compressibility relationships that affect the fluid and solid phase mass balance of the gouge. This is elaborated on in Section 2.2 - **Fluid mass balance** and 2.2 - **Solid gouge constituent mass balance**, as well as in [34]. Similar description was developed by [60]. Here we present a more complex physical system than [60], which includes total normal stress changes and fault perpendicular displacements. Thus, a more elaborate description is needed. This includes considering material compression under uniaxial normal stress. While defining a uniaxial compressibility is not often done, such compressiblity has been useful in problems related to stress transfer on faults in elastic and poroelastic medium [18].

Now we briefly review the most relevant parameters related to the shear zone description; a more complete mathematical description is provided in Section 2.2. The shear zone is a thin layer of half-width ϵ. Here thin indicates that ϵ should be much smaller than any significant variation in fields, such as slip or pressure, along the x-axis. This assumption is fundamental for the accuracy of the boundary-layer treatment of the shear zone. The properties of the shear zone or fault gouge are characterized by reference porosity ϕ_0, inelastic dilatancy coefficient γ [60], and pore pressure and normal stress dependent void volume compressibilities β_n^p and β_n^σ. In addition, the intact gouge material compressibilities are β_g^p and β_g^σ, and the fluid compressibilities are β_f^p and β_f^σ, where the β-coefficients represent linearized relationships between changes in volume and stress and pressure. These relationship can be considered as representing contribution of elastic or reversible processes, for example, β_n^p and β_n^σ describe the elastic component of the porosity change.

The frictional strength of the shear zone is determined by the reference coefficient of friction f_0, the characteristic state evolution distance D_{RS}, the constitutive parameter

a that scales the direct rate dependence of friction, and the constitutive parameter b that scales the state dependence of friction. A similar description of a shear zone was developed in [34], but here we include more physical processes that alter shear zone fluid flow. First, we consider that there may be a source of fluid mass in the layer, for example by injection, indicated by Q. Second, we include an anisotropic mobilities κ_{cx} and κ_{cy} (defined as permeability over dynamic fluid viscosity) assuming Darcy flow. In particular, the mobility in the y direction, κ_{cy} can be different from the mobility in the x direction κ_{cx}. Thus, fluids injected into the fault have multiple migration paths, along the shear zone, perpendicular to the shear zone, and in both x and y directions in the bulk. Furthermore, an increase in pore pressure in the bulk can migrate into the shear zone and also to the bulk on the other side (Figure 2.1a).

In terms of geological description of fault-zone permeability structures, our setup falls best in the category of a localized conduit as identified by [10]. That is a fault without a significant damage zone or fault core. Such simple faults are particularly relevant for field-scale fault injection experiments and have been targeted in previous experiments [29] and will be targeted in future [42] experiments. We suggest, however, that our problem setup could be reinterpreted and applied to a larger class of problems with minor modifications. For example, the shear zone could be interpreted to represent any thin diffusive structure that may undergo shear or dilatation. Thus our solutions, in particular the spectral boundary integral solutions, have a wider applicability than presented here and could be applied to problems related to damage zones or fault cores.

Motivation

A key question in induced seismicity is to understand when so-called runaway ruptures happen, that is ruptures that propagate well outside a pressurized region. This is a useful focal point to explain some of the general dynamics that we expect from the problem described above. When injection into a fault occurs, there are two important length scales along the x dimension (Figure 2.1) that can interact and explain the dynamics of the slip. First, how far the pressure front from the injection site has diffused, which we can define as the region of significantly elevated pore pressure. Second, how far the rupture tip has propagated, which can be understood as the region of significant fault slip. If a fault has relatively low shear stress, i.e., its shear stress over initial effective normal stress is significantly below its reference friction coefficient, or is well-healed, which may be common in injection experiments, the pore pressure front controls how far the rupture tip can move since the frictional resistance is too great outside the pressure front [38]. However, if a fault is relatively well-stressed, or if the slipping region enters a more well-stressed portion of the fault or a portion of the fault with lower friction, then the rupture may become self-sustained and rupture outside the pressure front. Thus the rupture may initially be contained by the pressure front, but evolve to become a runaway rupture.

The interplay of the rupture tip and pressure front provides a useful qualitative explanation of the transition from a confined to runaway rupture. However, additional complexity, which is related to the pressure profile across the fault, plays an important role in determining the if, when or how such a rupture can happen. If a rupture is initiated in a shear zone by injection, the pressure profile across the shear zone (i.e., pressure change with y, Figure 2.1b) can be dominated by different mechanisms depending on whether observing the profile at a x coordinate that is ahead of the rupture, at the tip or behind the tip (Figure 2.1b). This is particularly prominent for an in-plane rupture direction due to the volumetric straining of the bulk. If the pressurized zone is ahead of the rupture, the shear zone central pressure (p_c) would be elevated. The pore pressures adjacent to the shear zone (p^+ and p^-) would also be elevated due to the leak-off into the bulk. Near the tip region, the influence of dilatancy starts to lower the pore pressure p_c, but furthermore volumetric straining of the bulk causes an increase in pore pressure on the compressive side (p^+) and decrease on the dilating side (p^-) due to poroelastic coupling. Finally, behind the tip, dilatancy may have further reduced the pressure p_c and possibly reversed the sign compared to the background equilibrium pressure and caused flow back into the shear zone. We thus suggest that, in order to model rupture propagation, earthquake nucleation, and understand runaway ruptures in a fluid-saturated medium due to injection, we must consider coupling that arises from the interplay of several mechanisms that alter the pore pressure.

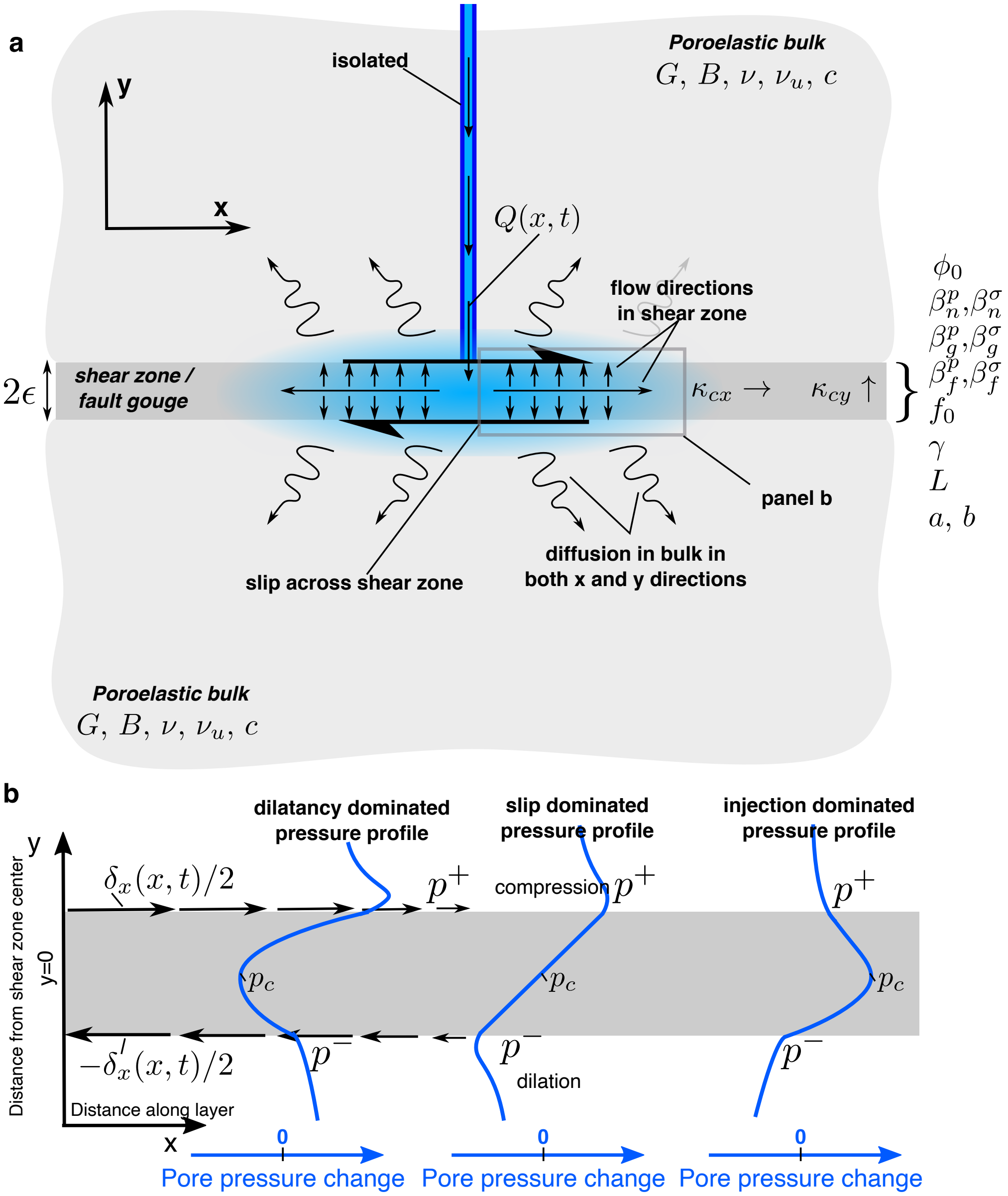

Figure 2.1: Schematic overview of the problems setup and possible pore pressure profiles scenarios in the shear zone. (a) Injection occurs in a thin shear zone embedded between two poroelastic halfspaces of the same properties. This injection causes fluid migration along the shear zone, across the shear zone, and into the bulk. The evolving pore fluid pressure leads to slip across the shear zone by reducing effective normal stress. (b) Pore pressure profiles that can occur during the propagation of a single rupture induced by injection. If the pore pressure diffusion is ahead of the rupture, then the shear zone has increased pressure compared to background (right-most profile). However, inelastic dilatancy may reduce the pressure. We call this a dilatancy dominated pore pressure (left-most profile). Between the two cases of injection and dilatancy dominated regimes, we expect at or near the rupture tip the two effects may cancel. However, the compression and dilation of the host rock induced by the inhomogeneous slip can significantly change the pore pressures on either side of the shear zone (p^+ and p^-). Fluid mass is introduced in practice as an arbitrary source term $Q(x,t)$ (see Section 2.2). The isolated pipe serves only visualization purposes.

2.2 Governing equations

This section describes the conservation laws, friction laws, and boundary conditions.

Poroelastic bulk

The quasi-static theory of poroelasticity can be described as four coupled partial differential equations written in terms of displacements u_i and fluid pressure changes p relative to an equilibrium pressure state [20, 12]:

$$Gu_{i,kk} + \frac{G}{1-2\nu}u_{k,ki} = \alpha p_{,i} \tag{2.1}$$

and

$$\frac{1}{M}p_{,t} - \kappa p_{,kk} = -\alpha u_{k,kt}, \tag{2.2}$$

where the material parameters are as follows: G: shear modulus, ν: drained Poisson's ratio, α: Biot-Willis parameter, M: Biot modulus, and κ is the mobility (the ratio between the permeability and fluid viscosity). In later expressions, a different set of poroelastic material parameter may be used for compactness and increased intuition, in particular Skempton's coefficient B and undrained Poisson's ratio ν_u. The Biot modulus M may not be as well know as the others, but it is defined as the change in amount of fluid per unit change in pressure at constant volumetric strain. It is inversely proportional to the storage coefficient. The Biot modulus offers a simple and useful relationship between mobility and hydraulic diffusivity in the poroelastic medium by $c = \kappa M$. This relationship can also be written without M as:

$$c = \kappa\frac{2GB(1+\nu)}{3\alpha(1-\alpha B)(1-2\nu)}. \tag{2.3}$$

Skempton's coefficient B and undrained Poisson's ratio ν_u can be related to the other aforementioned set of 5 parameters via:

$$B = \frac{3M\alpha(1-2\nu)}{2G(1+\nu)+3M\alpha^2(1-2\nu)}, \tag{2.4}$$

$$\nu_u = \frac{2G\nu + M\alpha^2(1-2\nu)}{2G+2M\alpha^2(1-2\nu)}. \tag{2.5}$$

Finally, Skempton's coefficient can then be expressed simply in terms of Poisson's ratios and the Biot-Willis parameter:

$$B = \frac{3(\nu_u - \nu)}{\alpha(1-2\nu)(1+\nu_u)}. \tag{2.6}$$

In this work, we assume plane strain deformation, in which case the governing equations can be reduced to three. Further simplification and decoupling of the governing equations is possible by using the McNamee-Gibson displacement functions [45, 67]. In obtaining solutions to equations (2.1) and (2.2), we follow the strategy explained in the Appendix of [33] using the McNamee-Gibson displacement functions but using the boundary conditions listed in the next section.

Boundary conditions

We apply the following boundary conditions at the interface, i.e., the shear zone, and at infinity.

$$\lim_{y\to 0^\pm} u_x^+ - u_x^- = \delta_x, \tag{2.7}$$

$$\lim_{y\to 0^\pm} u_y^+ - u_y^- = \delta_y, \tag{2.8}$$

$$\lim_{y\to \pm\infty} u_x^\pm = 0 \text{ and } u_y^\pm = 0, \tag{2.9}$$

$$\lim_{y\to \pm\infty} p^\pm = 0, \tag{2.10}$$

$$\lim_{y\to 0^\pm} \sigma_{xy}^+ - \sigma_{xy}^- = 0, \tag{2.11}$$

$$\lim_{y\to 0^\pm} \sigma_{yy}^+ - \sigma_{yy}^- = 0, \tag{2.12}$$

where we have dropped the index notation and used x and y (as represented in Figure 2.1a). The first two reflect displacement discontinuities, that is slip δ_x (Mode II) and opening (or layer dilation) δ_y (Mode I). The third and fourth conditions require the fields to decay at infinity. The final two conditions enforce continuity of stresses across the interface or the shear zone.

The pore pressure in the shear zone is assumed to be bi-linear [34]. In other words, we parameterize the pore pressure as two linear profiles that are fully constrained by the pore pressure at the center p_c at $y = 0$ and the pressure at the shear zone boundaries where the poroelastic bulk meets the shear zone, that is, $p^\pm$ at $y = \epsilon^\pm$ (Figure 2.1). We can explicitly write out the assumed pore pressure profile as:

$$
\begin{aligned}
p(y) =& \frac{y}{\epsilon}(p^{+} - p_c) + p_c \quad \text{if } 0 < y < \epsilon \\
p(y) =& \frac{y}{\epsilon}(p_c - p^{-}) + p_c \quad \text{if } -\epsilon < y < 0.
\end{aligned} \tag{2.13}
$$

Equation 2.13 is a generalization of the leaky interface used in the plane strain dislocation solution of [64]. There are two main benefits of using Equation 2.13 for the pore pressure in the shear zone. First, we can fully reduce the dimension of the shear zone in a computational sense, meaning that we only need to simulate a 1D problem, although we incorporate 2D physics. Reducing the dimension of a computational domain is also achieved with a boundary integral method and we use a boundary integral method to describe the bulk (the outer solution). Thus, it is also desirable to extend this dimension reduction to the shear zone physics, which is the inner solution of the boundary layer treatment. Second, if the layer is indeed thin, we may expect the across-shear-zone pressure profile to evolve to linear profiles since such a profile would satisfy the quasi-static limit of a standard diffusion equation. We can thus expect a more general solution, without a dimensional reduction, to evolve to the bilinear profile. How fast that evolution occurs would depend on ϵ and κ_{cy} and needs more work to quantify. That being said, we stress that a rigorous treatment of this problem without dimensional reduction in 2D is a fruitful and important topic for future work. We suggest that our approach is a good starting point for accounting for pressure being variable in the shear zone, which is mostly considered to be a constant in other simplified treatments.

Assuming the bi-linear pressure parameterization and equating the fluid mass flux into the shear zone and in the bulk, and vice versa, gives rise to a pressure gradient boundary condition for the bulk:

$$
\left.\frac{dp^{\pm}}{dy}\right|_{y=0^{\pm}} = \pm \frac{\kappa_{cy}}{\kappa}\frac{(p^{\pm} - p_c)}{\epsilon}, \tag{2.14}
$$

where κ_{cy} is the shear zone mobility in the y direction and κ is the poroelastic bulk mobility related to the bulk hydraulic diffusivity by $c = M\kappa$.

We highlight that boundary conditions for the bulk are applied at $y = 0^{\pm}$ but, in the description of the shear zone, we treat it as a finite layer with thickness between $y = \pm\epsilon$. This is because we take a boundary layer approach similar to Appendix B of [54] where the inner solution, the shear zone, is assumed to have a finite thickness. However, the outer solution, the bulk, approximates the layer as having an infinitesimal thickness. Thus the assumption that any variation along the length of the shear zone occurs over a length scale much smaller than ϵ is implicit. In other words, we always require that $\epsilon k \ll 1$, with k representing the wavenumber (inverse of a wavelength) of any field that varies along the x-dimension.

Frictional properties

We represent the frictional strength of the layer in an averaged sense (as in [34]). We assume that the frictional strength of every point in the layer can be represented as follows:

$$\frac{\tau(x,t)}{\sigma(x,t) - p(x,y,t)} = f(x,y,t) \quad \text{for} - \epsilon < y < \epsilon, \tag{2.15}$$

where $\tau(x,t)$ is the sum of all contributions to the shear stress, both initial background value and slip contributions. We note that the shear stress is assumed to be spatially constant across the layer. $\sigma(x,t)$ represents background initial effective normal stress (normal stress minus the ambient pore pressure) plus the slip-induced changes in normal stress and it is also assumed to be spatially constant across the layer. However, we separate from $\sigma(x,t)$ the perturbation in pore pressure $p(x,y,t)$ since, as previously discussed, it cannot be assumed to be constant in y. Using equation (2.13) and averaging over the layer, we obtain:

$$\tau \frac{(p_c - p^+) \log\left(\frac{\sigma - p^-}{\sigma - p_c}\right) + (p_c - p^-) \log\left(\frac{\sigma - p^+}{\sigma - p_c}\right)}{2(p_c - p^-)(p_c - p^+)} = \langle f \rangle, \tag{2.16}$$

with $\langle f \rangle$ representing the frictional coefficient of the layer. We have explored using the equation above for modeling the interface frictional strength, but we find that it renders results similar to a linearized approximation valid in the limit of the pore pressure changes being small compared to the background normal stress:

$$\tau = (\sigma - \langle p(t) \rangle)\langle f \rangle, \tag{2.17}$$

where $\langle p(t) \rangle$ is the average pressure across the layers and can be computed directly

$$\langle p \rangle = \frac{1}{2\epsilon} \int_{-\epsilon}^{\epsilon} p(y) dy = \frac{1}{2}\left(p_c + \frac{p^+ + p^-}{2}\right). \tag{2.18}$$

Equation (2.17) further offers a simpler interpretation of the role of the pore pressure in the effective normal stress compared to equation (2.16), which helps to understand the simulation results.

We interpret the averaged friction coefficient $\langle f \rangle$ of the shear zone as being represented by the rate-and-state friction law [21, 56, 43]:

$$\langle f \rangle = \frac{1}{2\epsilon}\int_{-\epsilon}^{\epsilon} f(x,y,t)dy = a\text{arcsinh}\left[\frac{V}{2V_0}\exp\left(\frac{f_0 + b\log(V_0\theta/D_{RS})}{a}\right)\right], \quad (2.19)$$

where we use the regularized form of the friction law that is also valid for slip speeds V much smaller than the reference slip speed V_0 [50, 2, 37]. Here a and b are constitutive parameters that describe the rate dependence and state dependence of friction, respectively. Further, f_0 is the reference coefficient and D_{RS} is the characteristic slip distance over which the state evolves. The state variable is described by the aging law [56]:

$$\frac{d\theta}{dt} = 1 - \frac{\theta V}{D_{RS}}. \quad (2.20)$$

We note that here we introduce a difference to the treatment of the frictional properties of the shear zone in [34]. Here we represent friction using the regularized friction law whereas the non-regularized version was discussed by [34]. In the linearized analysis treated by [34], there is no difference between the two versions.

Shear zone

Here we analyze the fluid and solid constituent mass balance of the shear zone gouge. Although we offer a complete description of the governing equations, we highlight that more details may be found in [34]. Note that we build upon the shear zone description of [34] and introduce several new processes.

Fluid mass balance

Beyond previous work [34], we introduce two additional physical processes to the fluid mass balance of the shear zone. The two processes incorporate an injection or source term and allow for lateral diffusion along the shear zone.

Within the shear zone, the fluid mass balance is:

$$\frac{\partial m}{\partial t} + \frac{\partial q_y}{\partial y} + \frac{\partial q_x}{\partial x} = \frac{\partial}{\partial t}(Q(x,t)), \quad (2.21)$$

where m is the fluid mass content, q_y is fluid mass flux perpendicular to the fault (y-axis), q_x is the fluid mass flux parallel to the fault (x-axis), and $Q(x,t)$ is the cumulative fluid mass injected per unit volume of the shear zone.

We note that $m = \rho_f n$, where ρ_f is fluid density, and we follow [60] in assuming that the total void volume fraction can be described as $n = n^e + n^{pl}$, that is the sum of elastic and plastic void volume fraction. The rate of change in fluid mass fraction is then:

$$\dot{m} = \dot{\rho}_f n + \rho_f \dot{n}. \tag{2.22}$$

Following [34], we linearize $\dot{n}^e = \phi_0(\beta_n^p \dot{p} - \beta_n^\sigma \dot{\sigma})$ and $\dot{\rho}_f = \rho_{fo}(\beta_f^p \dot{p} + \beta_f^\sigma \dot{\sigma})$, where β_f^p and β_n^p are fluid and elastic void compressibilities, respectively, and $\sigma > 0$ means increased compression, also know as "the compression positive" convention. The compressibilities are mathematically defined in Appendix A. The reference compressibilities are defined at the reference void volume fraction ϕ_0 and fluid density ρ_{fo}. We assume the reference void volume fraction is the same as the porosity. Similarly, we assume plastic void fraction is equal to the plastic porosity: $n^{pl} = \phi^{pl}$. Thus equation (2.22) becomes:

$$\dot{m} = \rho_{fo}\phi_0(\beta_f^p \dot{p} + \beta_f^\sigma \dot{\sigma}) + \rho_{fo}\phi_0(\beta_n^p \dot{p} - \beta_n^\sigma \dot{\sigma} + \dot{\phi}^{pl}/\phi_0). \tag{2.23}$$

Darcy's law provides:

$$q_x = -\rho_{fo}\kappa_{cx}\frac{\partial p}{\partial x}, \tag{2.24}$$

where κ_{cx} is the mobility (permeability over dynamic viscosity) for fluid flux along the x-axis within the shear zone, which is assumed to be spatially constant with respect to x.

Combining equations (2.21), (2.23), and (2.24) and integrating with respect to the y-axis gives:

$$\begin{aligned} 2\epsilon\rho_{fo}\phi_0 &\left[(\beta_f^p + \beta_n^p)\langle\dot{p}\rangle + (\beta_f^\sigma - \beta_n^\sigma)\dot{\sigma} + \langle\dot{\phi}\rangle^{pl}/\phi_0)\right] \\ &+ q_y^+ - q_y^- - 2\epsilon\rho_{fo}\kappa_{cx}\frac{\partial^2\langle p\rangle}{\partial x^2} = 2\epsilon\dot{Q}(x,t), \end{aligned} \tag{2.25}$$

where the source term Q is assumed constant with respect to y.

Inserting for the fluid mass flux in y direction, given the bi-linear pressure distribution, in the shear zone (equations (2.14) and (2.13)) provides:

$$\langle \dot{p} \rangle + \frac{\beta_f^\sigma - \beta_n^\sigma}{\beta_f^p + \beta_n^p}\dot{\sigma} = -\frac{\langle \dot{\phi} \rangle^{pl}}{\phi_0(\beta_f^p + \beta_n^p)} + \frac{\kappa_{cy}}{\epsilon^2 \phi_0(\beta_f^p + \beta_n^p)}(\frac{1}{2}(p^+ + p^-) - p_c)$$
$$+ \frac{\kappa_{cx}}{\phi_0(\beta_f^p + \beta_n^p)}\frac{\partial^2 \langle p \rangle}{\partial x^2} + \frac{\dot{Q}(x,t)}{\rho_{fo}\phi_0(\beta_f^p + \beta_n^p)}. \tag{2.26}$$

We have thus derived an equation that relates average pressure, normal stress, dilatancy, along shear zone diffusion, and fluid mass injection. The inelastic change in porosity ϕ^{pl} is taken as

$$\langle \phi \rangle^{pl} = \phi_0^{pl} - \gamma \log\left(\frac{V_0 \theta}{D_{RS}}\right), \tag{2.27}$$

where ϕ_0^{pl} could reflect an initial value of the inelastic porosity change. However, such a constant could also be interpreted as a part of the reference porosity ϕ_0. Equation (2.27) is based on [60] and [62], which proposed that the inelastic porosity is a function of the frictional state variable, $\phi^{pl}(\theta)$, based on analyzing experimental data by [44]. We assume here that the frictional state variable θ is related to the average porosity change in the shear zone. The other approach is to relate the porosity change to the instantaneous slip rate $\phi^{pl}(V)$, but both interpretations of the [44] data are equivalent when linearized around steady-state sliding. Showing the two are the same at steady state is simple. At steady-state slip rate V_{ss}, one gets $\theta = D_{RS}/V_{ss}$, so equation 2.27 becomes $\langle \phi \rangle^{pl} = \phi_0^{pl} + \gamma \log(V_{ss}/V_0)$, which corresponds to the steady state of the slip rate dependent formulation of [60]. Equation 2.27 can also be written directly to represent the rate of change in plastic porosity [59]: $\langle \dot{\phi} \rangle^{pl} = -\gamma \dot{\theta}/\theta$.

The interpretation of linking inelastic dilatancy and state has gained more observational support recently where experiments by [48] suggest that the state variable and dilatancy are directly linked. [48] suggest the state could be cast as dilatancy or vice versa as is reflected by equation (2.27). It is worth noting that although the experiments by [48] show agreement with the [60] dilatancy relationship based on the experimental work of [44], more complex behavior emerges at higher velocity steps. Equation (2.27) does thus not offer a complete description of how fault gouge dilatancy and compaction evolve, an important question that requires future experimental and theoretical study.

Before implementing equation (2.26) numerically, we analytically integrate it to obtain:

$$\langle p\rangle + \frac{\beta_f^\sigma - \beta_n^\sigma}{\beta_f^p + \beta_n^p}\sigma = \frac{1}{\phi_0(\beta_f^p + \beta_n^p)}\left(\frac{Q(x,t)}{\rho_{fo}} - \langle\phi\rangle^{pl} + \int_0^t \frac{\kappa_{cy}}{\epsilon^2}(\frac{1}{2}(p^+ + p^-) - p_c) + \kappa_{cx}\frac{\partial^2\langle p\rangle}{\partial x^2}dt'\right), \tag{2.28}$$

where it is assumed that all fields are 0 at $t = 0$.

Solid gouge constituent mass balance

Similar to the fluid mass balance (equation 2.21), we can state the conservation of solid mass (gouge material) in the shear zone:

$$\frac{\partial m_g}{\partial t} + \frac{\partial}{\partial y}\left((1-n)\rho_g\dot{u}_y\right) + \frac{\partial}{\partial x}\left((1-n)\rho_g\dot{u}_x\right) = 0, \tag{2.29}$$

where ρ_g is the density of the intact gouge and u_x and u_y are the x and y components of displacement of the gouge in the shear zone.

The mass of the solid material (gouge) in a control volume within the shear zone is $m_g = (1-n)\rho_g$ and thus the rate of change in solid mass is given by

$$\dot{m}_g = -\rho_g\dot{n} + (1-n)\dot{\rho}_g. \tag{2.30}$$

Following the same linearization proceedure and integration across the shear zone as before (see [34] for details on procedure and assumptions), we obtain a constitutive relationship for fault perpendicular displacements:

$$\dot{\delta}_y = 2\epsilon\left(\frac{\phi_0}{1-\phi_0}\beta_n^p - \beta_g^p\right)\left[\langle\dot{p}\rangle - \frac{\left(\frac{\phi_0}{1-\phi_0}\beta_n^\sigma + \beta_g^\sigma\right)}{\left(\frac{\phi_0}{1-\phi_0}\beta_n^p - \beta_g^p\right)}\dot{\sigma}\right] + 2\epsilon\frac{\langle\dot{\phi}\rangle^{pl}}{1-\phi_0}. \tag{2.31}$$

Assuming that that all fields are zero at $t = 0$, such that no net dilatancy or compaction occurs, then the equation can be integrated

$$\delta_y = 2\epsilon\left(\frac{\phi_0}{1-\phi_0}\beta_n^p - \beta_g^p\right)\left[\langle p\rangle - \frac{\left(\frac{\phi_0}{1-\phi_0}\beta_n^\sigma + \beta_g^\sigma\right)}{\left(\frac{\phi_0}{1-\phi_0}\beta_n^p - \beta_g^p\right)}\sigma\right] + 2\epsilon\frac{\langle\phi\rangle^{pl}}{1-\phi_0}. \tag{2.32}$$

The additional compressibilities β_g^p and β_g^σ are mathematically defined in Appendix A. In the parameter regime studied in this paper (Appendix A), we do not expect the

δ_y mode I displacements to be significant, but we include this here for completeness and because this effect is included in the computational code that accompanies this paper [31]. More information on the parameter regime when opening mode contributions can significantly influence fault slip is discussed in [34].

2.3 Solutions for a poroelastic bulk coupled to a shear zone

Let us develop solutions in the Fourier-Laplace domain given the boundary conditions in Section 2.2. We define the joint Fourier-Laplace transform:

$$\bar{\hat{\delta}}_x(s,k) = \int_0^\infty \int_{-\infty}^\infty \delta_x(t,x) e^{-ikx-st} dx dt, \tag{2.33}$$

applied here on the slip $\delta_x(x,t)$, or displacement discontinuity across the layer in the x direction, where the bar symbol represents the Laplace transform in time and the hat the Fourier transform along the x spatial axis. Some symbols may not carry the hat symbol if they are explicitly written out in terms of the wavenumber k.

We follow the procedure outlined by [33] and derive solutions in the Fourier-Laplace domain for shear stress, pore pressure, and normal stress change at the slip surface ($y \to 0^\pm$). The relationships between change in shear stress $\bar{\hat{\tau}}'$, pore pressure change on either side of the layer $\bar{\hat{p}}^\pm$, and change in total normal stress $\bar{\hat{\sigma}}_{yy}$ in terms of $\bar{\hat{\delta}}_x$, $\bar{\hat{\delta}}_y$, and $\bar{\hat{p}}_c$ are given by the following equations [34]:

$$\bar{\hat{\tau}} = -\frac{G|k|\bar{\hat{\delta}}_x}{2(1-\nu_u)} \bar{H}_1(s,k) \tag{2.34}$$

and

$$\bar{p}^\pm = \mp \frac{ikGB\bar{\hat{\delta}}_x}{3} \frac{1+\nu_u}{1-\nu_u} \bar{H}_2(s,k) - \bar{\hat{p}}_c \frac{\mathcal{F}}{\mathcal{F}+1} \left(\bar{H}_2(s,k) - 1\right) + \frac{|k|GB\bar{\hat{\delta}}_y}{3} \frac{1+\nu_u}{1-\nu_u} \bar{H}_2(s,k), \tag{2.35}$$

and

$$\bar{\hat{\sigma}}_{yy} = \bar{\hat{p}}_c \frac{3}{2B(1+\nu_u)} \frac{\mathcal{F}}{\mathcal{F}+1} (\bar{H}_1(s,k) - 1) - \frac{G|k|\bar{\hat{\delta}}_y}{2(1-\nu_u)} \bar{H}_1(s,k), \tag{2.36}$$

where

$$\bar{H}_1(s,k) = 1 - \frac{2(\nu_u - \nu)}{1-\nu} \frac{ck^2}{s} \frac{1+\mathcal{F}}{\mathcal{F} + \sqrt{1+s/ck^2}} \left(\sqrt{1+s/ck^2} - 1\right), \tag{2.37}$$

and

$$\bar{H}_2(s,k) = \frac{\sqrt{1+s/ck^2}-1}{\sqrt{1+s/ck^2}+\mathcal{F}}. \tag{2.38}$$

$\mathcal{F}$ is a dimensionless group that characterizes the importance of flux across the fault:

$$\mathcal{F} = \frac{\kappa_{cy}}{\kappa}\frac{1}{|k|\epsilon}. \tag{2.39}$$

In order to obtain the spectral boundary integral solutions, these solutions are not sufficient since we need to invert the Laplace transform. We begin this process by defining:

$$\bar{K}_1 = \bar{H}_1 - 1 \text{ and } \bar{K}_2 = \bar{H}_2 - 1. \tag{2.40}$$

As shown by [33], $\bar{H}_1$ and $\bar{H}_2$ approach unity in the limit of short time or negligible diffusion, which reduces Eqs. (2.34), (2.35), and (2.36) to their corresponding undrained limits. $\bar{K}_1$ and $\bar{K}_2$ thus represent the transient changes in shear stress and pore pressure on the fault that arise due to pore pressure diffusion.

$\bar{H}_1$ and $\bar{H}_2$ are related by $\bar{H}_1 = 1-2(\nu_u-\nu)/(1-\nu)(1+\mathcal{F})(ck^2/s)\bar{H}_2$. Thus, in the time domain, the inverse transform of $\bar{H}_1$ is closely related to the time integral of the inverse transform of $\bar{H}_2$. Using the convolution theorem for Laplace transforms, we find that Eqs. (2.34) and (2.35) take the form:

$$\hat{\tau}' = -\frac{G|k|}{2(1-\nu_u)}\left(\hat{\delta}_x + \int_0^t \hat{\delta}_x(t')K_1(t-t',k)dt'\right), \tag{2.41}$$

$$\begin{aligned} \hat{p}^{\pm} = &\mp \frac{ikGB}{3}\frac{1+\nu_u}{1-\nu_u}\left(\hat{\delta}_x + \int_0^t \hat{\delta}_x(t')K_2(t-t',k)dt'\right) \\ &- \frac{\mathcal{F}}{\mathcal{F}+1}\int_0^t \hat{p}_c(t')K_2(t-t',k)dt' \\ &+ \frac{|k|GB}{3}\frac{1+\nu_u}{1-\nu_u}\left(\hat{\delta}_y + \int_0^t \hat{\delta}_y(t')K_2(t-t',k)dt'\right), \end{aligned} \tag{2.42}$$

and equation (2.36) becomes

$$
\begin{aligned}
\hat{\sigma}_{yy} = & \frac{3}{2B(1+\nu_u)} \frac{\mathcal{F}}{\mathcal{F}+1} \int_0^t \hat{p}_c(t') K_1(t-t',k) dt' \\
& - \frac{G|k|}{2(1-\nu_u)} \left(\hat{\delta}_y + \int_0^t \hat{\delta}_y(t') K_1(t-t',k) dt' \right).
\end{aligned} \tag{2.43}
$$

We have thus separated the undrained response and the transient diffusional behavior. This behavior is characterized by the convolution kernels K_1 and K_2 that represent the inverse Laplace transforms of $\bar{K}_1$ and $\bar{K}_2$, respectively. In other words, $K_1(t) = \mathcal{L}^{-1}\left\{\bar{K}_1\right\}(t)$ and $K_2(t) = \mathcal{L}^{-1}\left\{\bar{K}_2\right\}(t)$.

The convolution kernels for fault slip problems in poroelastic medium can be constructed numerically and this may be the only option for more complex bulk rheology such as accounting for full inertial effects [32]. The numerical inversion of the Laplace transform is, however, a difficult and numerically intensive task. Here we derived analytical expressions for K_1 and K_2 through repeated application of the convolution theorem to separate $\bar{K}_1$ and $\bar{K}_2$ into factors of known inverse Laplace transforms.

$$
\begin{aligned}
K_1(t,k) = & - \frac{2(\nu_u - \nu)}{1-\nu} ck^2 (1+\mathcal{F}) \\
& \left(1 + \frac{1}{\mathcal{F}-1} \left[\mathcal{F} e^{(\mathcal{F}^2-1)ck^2 t} \operatorname{erfc}\left(\mathcal{F}\sqrt{ck^2 t} \right) - \mathcal{F} + \operatorname{erf}\left(\sqrt{ck^2 t} \right) \right] \right)
\end{aligned} \tag{2.44}
$$

$$
K_2(t,k) = - ck^2 (1+\mathcal{F}) \left[\frac{e^{-ck^2 t}}{\sqrt{\pi ck^2 t}} - \mathcal{F} e^{(\mathcal{F}^2-1)ck^2 t} \operatorname{erfc}\left(\mathcal{F}\sqrt{ck^2 t} \right) \right]. \tag{2.45}
$$

We note that kernel K_2 is singular when $t \longrightarrow 0$. However, this is an integrable singularity and the convolution kernel can be integrated in the sense of taking a Cauchy principal value. K_1 and K_2 reveal directly that fluid transport in and into the bulk is governed by two characteristic timescales,

$$
t_b = \frac{1}{ck^2} \tag{2.46}
$$

and

$$
t_f = \frac{1}{\mathcal{F}^2 ck^2} = \frac{\kappa^2 \epsilon^2}{\kappa_c^2 c}, \tag{2.47}
$$

where t_b can be understood as a traditional length-scale-dependent diffusional time scale, while t_f represents a scale of flux through and from the shear zone and is independent of the length scale as long as $k\epsilon \ll 1$.

Equations (2.41), (2.42), and (2.43) offer several other interesting insights into how the bulk couples to the shear zone. We first observe that shear stress only depends on the slip (2.41). However, pore pressure at the interfaces between the shear zone and bulk (2.42) has a complex dependence on both slip and opening mode as well as the shear-zone center pressure p_c. In the limit $\mathcal{F} \rightarrow 0$, the pressure in the bulk and shear-zone center decouples. This could happen in the limit of $\kappa_{cy} \rightarrow 0$ or when the shear zone is impermeable for flux along the y dimension. $\mathcal{F}$ depends on the mobility or permeability contrast of the bulk and shear zone κ_{cy}/κ, where bulk mobility $\kappa = c/M$ has been previously explained. But the requirement $\kappa_{cy}/\kappa \ll 1$ is not sufficient for fluids to remain in the shear zone because $\mathcal{F} \propto 1/|k|\epsilon$ (equation 2.39) and $|k|\epsilon \ll 1$. Equation (2.43) shows an interesting coupling to normal stress. The relationship between opening mode δ_y and normal stress change is obvious; however, the coupling of shear zone center pressure p_c to σ_{yy} is a poroelastic response as fluids flow from the shear zone into the bulk. This coupling is removed if $\mathcal{F} \rightarrow 0$ and fluids cannot enter the bulk from the shear zone.

In summary, (2.41), (2.42), and (2.43) represent analytical solutions for the shear stress, pore pressure (at shear zone boundary), and normal stress given a time-history of slip δ_x, opening δ_y and/or shear zone center pore pressure p_c which have been transformed in the wavenumber (Fourier) domain. Alternatively, these expressions represent analytical solutions for a single plane wave perturbation in slip δ_x, δ_y and/or p_c of generic form $f(t)\exp(ikx)$, where $f(t)$ is some time-dependent function. In Section 2.4, we use this property to construct general solutions for arbitrary histories of slip δ_x, opening δ_y and/or shear zone center pore pressure p_c.

2.4 Numerical method

Fourier series representation of poroelastic relations

We represent δ_x, δ_y and p_c as Fourier series

$$\delta_x(x,t) = \sum_{n=-N/2}^{N/2-1} D_{x,n}(t) e^{ik_n x}, \quad k_n = \frac{2\pi n}{\lambda}, \tag{2.48}$$

$$\delta_y(x,t) = \sum_{n=-N/2}^{N/2-1} D_{y,n}(t) e^{ik_n x}, \quad k_n = \frac{2\pi n}{\lambda}, \tag{2.49}$$

and

$$p_c(x,t) = \sum_{n=-N/2}^{N/2-1} P_n(t) e^{ik_n x}, \quad k_n = \frac{2\pi n}{\lambda}, \tag{2.50}$$

where N is even and equal to the number of points at which $\delta(x,t)$ and $p_c(x,t)$ are evaluated, and λ represents the length of the simulation domain. The Fourier transform is given by

$$\hat{\delta}_x(k,t) = \sum_{n=-N/2}^{N/2-1} 2\pi D_{x,n}(t) \delta_D(k - k_n), \tag{2.51}$$

and corresponding relations exist for $\hat{p}_c$ and $\hat{\delta}_y$ where δ_D is the Dirac delta function. Inserting the transformed series into equations (2.41), (2.42) , and (2.43) and performing the trivial inverse Fourier transforms provide

$$\tau' = -\frac{G}{2(1-\nu_u)} \sum_{n=-N/2}^{N/2-1} |k_n| \left(D_{x,n}(t) + \int_0^t D_{x,n}(t') K_1(t-t', k_n) dt' \right) e^{ik_n x}, \tag{2.52}$$

$$\begin{aligned} p^{\pm} = \sum_{n=-N/2}^{N/2-1} \Bigg(&\mp \frac{iGB}{3} \frac{1+\nu_u}{1-\nu_u} k_n \left[D_{x,n}(t) + \int_0^t D_{x,n}(t') K_2(t-t', k_n) dt' \right] + \ldots \\ &\frac{GB}{3} \frac{1+\nu_u}{1-\nu_u} |k_n| \left[D_{y,n}(t) + \int_0^t D_{y,n}(t') K_2(t-t', k_n) dt' \right] - \ldots \\ &\frac{\mathcal{F}(k_n)}{\mathcal{F}(k_n)+1} \int_0^t P_n(t') K_2(t-t', k_n) dt' \Bigg) e^{ik_n x}, \end{aligned} \tag{2.53}$$

and

$$\begin{aligned} \sigma_{yy} = \frac{3}{2B(1+\nu_u)} \sum_{n=-N/2}^{N/2-1} \Bigg(&\frac{\mathcal{F}(k_n)}{\mathcal{F}(k_n)+1} \int_0^t P_n(t') K_1(t-t', k_n) dt' - \ldots \\ &\frac{G}{2(1-\nu_u)} |k_n| \left[D_{y,n}(t) + \int_0^t D_{y,n}(t') K_1(t-t', k_n) dt' \right] \Bigg) e^{ik_n x}. \end{aligned} \tag{2.54}$$

Testing and validation of this approach reveals that the first term of the pore pressure (2.53) is prone to developing the Gibbs phenomenon in the presence of steep gradients. This may stem from how the sign of the pore pressure depends on k_n and not the absolute value of $|k_n|$ as for other terms. Oscillations, such as the Gibbs phenomena, are somewhat mitigated by the diffusional nature of the pore pressure where short-wavelength oscillations diffuse rapidly. However, a much improved convergence of the series in (2.35) and nearly complete removal of the Gibbs phenomenon can be achieved with a Lanczos sigma factor [23]:

$$\begin{aligned} p^{\pm} = \sum_{n=-N/2}^{N/2-1} \Bigg(&\mp \frac{iGB}{3}\frac{1+\nu_u}{1-\nu_u} k_n \operatorname{sinc}\left(\frac{n}{N/2}\right) \left[D_{x,n}(t) + \int_0^t D_{x,n}(t') K_2(t-t', k_n) dt' \right] + \ldots \\ &\frac{GB}{3}\frac{1+\nu_u}{1-\nu_u} |k_n| \left[D_{y,n}(t) + \int_0^t D_{y,n}(t') K_2(t-t', k_n) dt' \right] - \ldots \\ &\frac{\mathcal{F}(k_n)}{\mathcal{F}(k_n)+1} \int_0^t P_n(t') K_2(t-t', k_n) dt' \Bigg) e^{ik_n x}, \end{aligned} \tag{2.55}$$

where $\operatorname{sinc}(x) = \sin(\pi x)/(\pi x)$ is the normalized sinc function. It is worth noting that an inverse FFT of the Fourier coefficients in (2.52, 2.53, 2.54, and 2.55) is an efficient way to compute the stresses and pore pressure at each value of x.

Comparison to Song and Rudnicki (2017)

We partially validate the solutions in the previous section by comparing them to the analytical solution provided for a single edge dislocation on a leaky plane by [64] (Figure 2.2). In the problem analyzed by [64], $\delta_x = \mathcal{H}(t)\mathcal{H}(-x)$ with $\mathcal{H}(\cdot)$ being the Heaviside step function, $\delta_y = 0$, $p_c = 0$, in which case $\sigma_{yy} = 0$. We use equations (2.52) and (2.55) after retrieving the Fourier series coefficients using a fast Fourier transform (FFT) algorithm of $\delta_x = \mathcal{H}(t)\mathcal{H}(-x)$ evaluated on a domain size ranging from $x = -50$ to $x = 50$ m. Comparison in Figure 2.2 reveals excellent agreement between the two approaches. Further discussion of the method validation is in Appendix C.

Convolution kernel computation and truncation

Along with time stepping all relevant equations, which is detailed in Appendix B, we update and calculate the convolution in equations (2.52), (2.54), and (2.55). In computing the convolution, we first compute kernel values at lag times t_i for each wavenumber k_n, i.e., $K_1(t_i, k_n)$ and $K_2(t_i, k_n)$, where t_i are selected to span

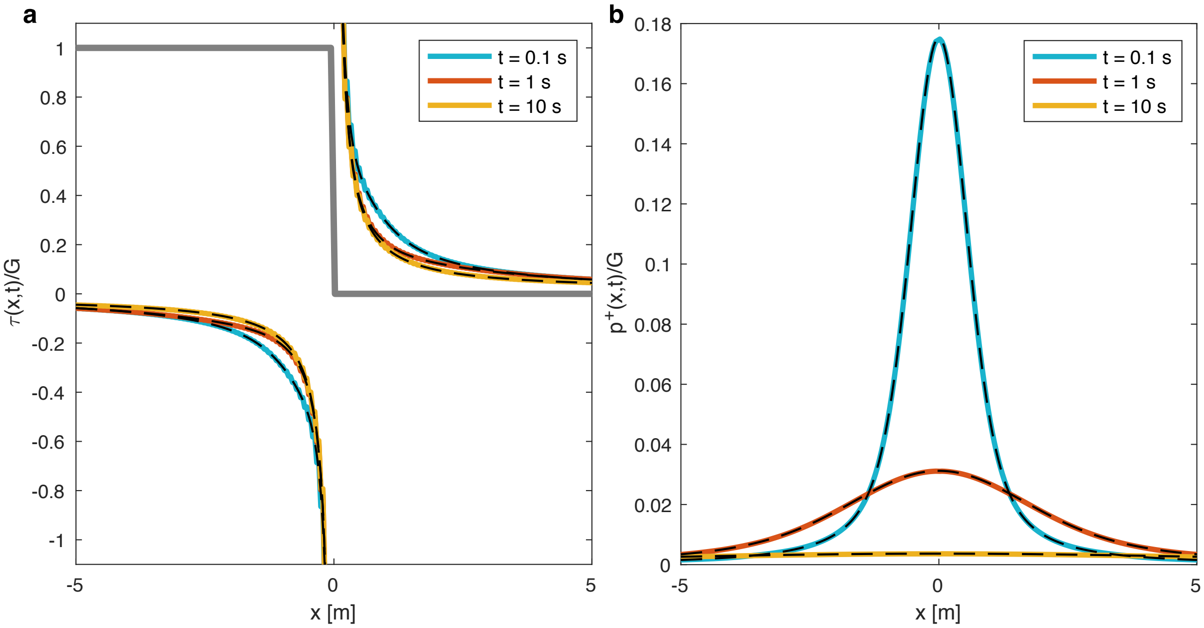

Figure 2.2: Comparison of our solution based on equations (2.52) and (2.55) and the analytical solution (equations (A1) and (72), respectively) for a problem in [64]. Colored lines represent the spectral boundary-integral solution and overlapping dashed black lines represent the [64] solution. (a) Shear stress normalized by shear modulus G near the dislocation edge (indicated in gray) of unit slip amplitude at three different times, which span approximately the undrained, drained limits as well as an intermediate stage. (b) Pore pressure change due to the same edge dislocation. Results are shown for $c = 1$ m^2/s, $B = 0.5$, $\kappa_{cy}/(\kappa\epsilon) = 1$ m^{-1}, $\nu = 0.15$, $\nu_u = 0.45$.

a time interval from $\zeta_l \min(t_b, t_f)$ to $\zeta_u \min(t_b, t_f)$. In practice we take $\zeta_l = 10^{-6}$ and $\zeta_u = 20$ and t_b and t_f are the diffusion time-scales of the bulk and of the flux through the shear zone given by equations (2.46) and (2.47).

We thus evaluate the convolution kernels between a time that is negligible compared to the diffusional time-scales $\zeta_l \min(t_b, t_f)$, up to a time that is long compared to the diffusional time scales $\zeta_u \min(t_b, t_f)$. Evaluation points t_i are selected by combining both points at a linearly equally spaced times, and logarithmically equally spaced times. Here we use 1024 evaluation points, but we find that in some cases, such as the benchmarking against the linear stability analysis of [34], much fewer evaluation points are needed.

Since we pre-compute the convolution kernels, we need to determine the values of the Fourier coefficients $D_{x,n}$, $D_{y,n}$, P_n at times $t - t_i$. This is done by storing the Fourier coefficients' values at selected times and then determining their values at the convolution times t_i by linear interpolation.

The criteria for storing a Fourier coefficient value are implemented by setting an integer N_{st}, which is the maximum number of time-steps that can be taken without storing the Fourier coefficients. We compute

$$N_{st} = \left\lfloor \min(1 + \min(t_f, t_b)/\Delta t; 1 + \min(a\sigma_0/(p_c^n - p_c^{lst}))/20; N_{st}^{\max}) \right\rfloor, \qquad (2.56)$$

where p_c^{lst} is the vector of p_c values when the Fourier coefficients were last stored and $N_{st}^{\max}$ is a user-determined value that makes sure the coefficients are sampled at least every $N_{st}^{\max}$ time-step. The first criterion in the equation makes sure that the minimum diffusion time is resolved in the stored Fourier coefficients. Testing has suggested that under-sampling here may not be an issue since the shortest diffusion times correspond to the largest wavenumbers (shortest wavelengths) and if the simulation is well resolved, then the influence of these wavelengths is negligible. The second criterion makes sure that if the pore pressure is changing rapidly, then the information of these rapid changes is preserved in the stored coefficients. This is particularly important for injection problems. However, for efficiency, we overwrite the value above for N_{st} if $t^n - t^{lst} < \zeta_l \min(t_b, t_f)$, where t^{lst} is the time when the coefficients were last stored, in which case we set $N_{st} = N_{st}^{\max}$. This procedure makes sure that we do not store coefficients over time scales too short for any diffusional process to occur, making the seismic phase of the simulations much more efficient.

2.5 Application

Here we show an application of the numerical approach by simulating the [29] experiment, in which fluid was injected into a shallow fault and slip and pressure were monitored. The code (available here [31]) uses the spectral boundary integral solution, shear zone constitutive relationship, and a numerical method to simulate slow and fast slip on a rate-and-state fault in a poroelastic medium.

The slip and pressure data were previously analyzed by [38] by modeling 1D diffusion in a plane strain linear elastic bulk with rate-and-state friction. We use their parameter estimates (see also Table A.1) and their simplified pore pressure history (Figure 2.3a) as input, but we vary some of other processes and parameters that were not accounted for by [38], or in most comparable studies, including poroelastic properties, bulk diffusivity, and inelastic dilatancy. Specifically, we explore a set of parameters where the bulk hydraulic diffusivity is $c = 4{\cdot}10^{-8}$ or $4{\cdot}10^{-7}$ m^2/s; the undrained Poisson's ratio is ν_u =0.262 or 0.35 (while the drained Poisson's ratio ν is 0.24); and the dilatancy coefficient takes values γ =0 , $1.7{\cdot}10^{-5}$, and $1.7{\cdot}10^{-4}$. We implement the injection by setting $Q(x,t) = Q_s(x)Q_t(t)$, where the spatial part $Q_s(x)$ is a boxcar function between $x = \pm 0.5$ and $Q_t(t)$ is such that p_c matches the simplified pore pressure history (Figure 2.3a). Further discussion of parameters is given in Appendix A.

We follow the setup and initial conditions as implemented by [38]. However, some critical differences in the model setup and characterization of fluid flow are worth mentioning. [38] implemented 1D isotropic diffusion along the shear layer, corresponding to the pressure in the shear zone spatially constant in y; there is no fluid diffusion or coupling of the flow and deformation in the bulk. Here we assume that the pressure measured in the experiment [29] reflects the shear zone center pressure p_c, whereas in [38] this would be a constant value along the y-dimension at $x = 0$.

We stress that we do not aim either to replicate the simulations and results of [38] or to model the experiments of [29] explicitly. Our goal is to use these previous results to guide us in finding the relevant part of the parameter space consistent with experimental findings. Then we wish to vary other properties that are generally not tested in comparable studies - such as poroelastic properties of the bulk - to understand if they significantly affect the slip process and nucleation during fluid injection.

We take the simulation shown in Figure 2.4a, with $\gamma = 0$, $\nu_u = 0.262$, and $c = 4{\cdot}10^{-8}$, as our reference simulation. This simulation has most similarity with previous work since the poroelastic response is reduced (with $\nu_u = 0.262$ and $\nu = 0.24$ being close in value), the diffusivity of the bulk is small, and no inelastic dilatancy occurs.

The importance of leak-off into bulk

Before investigating the details of the slip in each simulation, we first look at the fluid leakoff in response to pressurization.

Without any dilatancy, the reference case (Figure 2.3b purple) has the least amount of leakoff into the bulk as expected since we consider this to be the most similar to elastic simulations with no bulk diffusion. Nevertheless about 23% of the injected mass is lost. It is curious to compare the $\nu_u = 0.262$, $c = 4{\cdot}10^{-7}$ m^2/s and $\nu_u = 0.35$, $c = 4{\cdot}10^{-8}$ m^2/s (Figure 2.3b yellow and orange, respectively). One would expect that changing the bulk diffusivity by a factor of 10 would have much

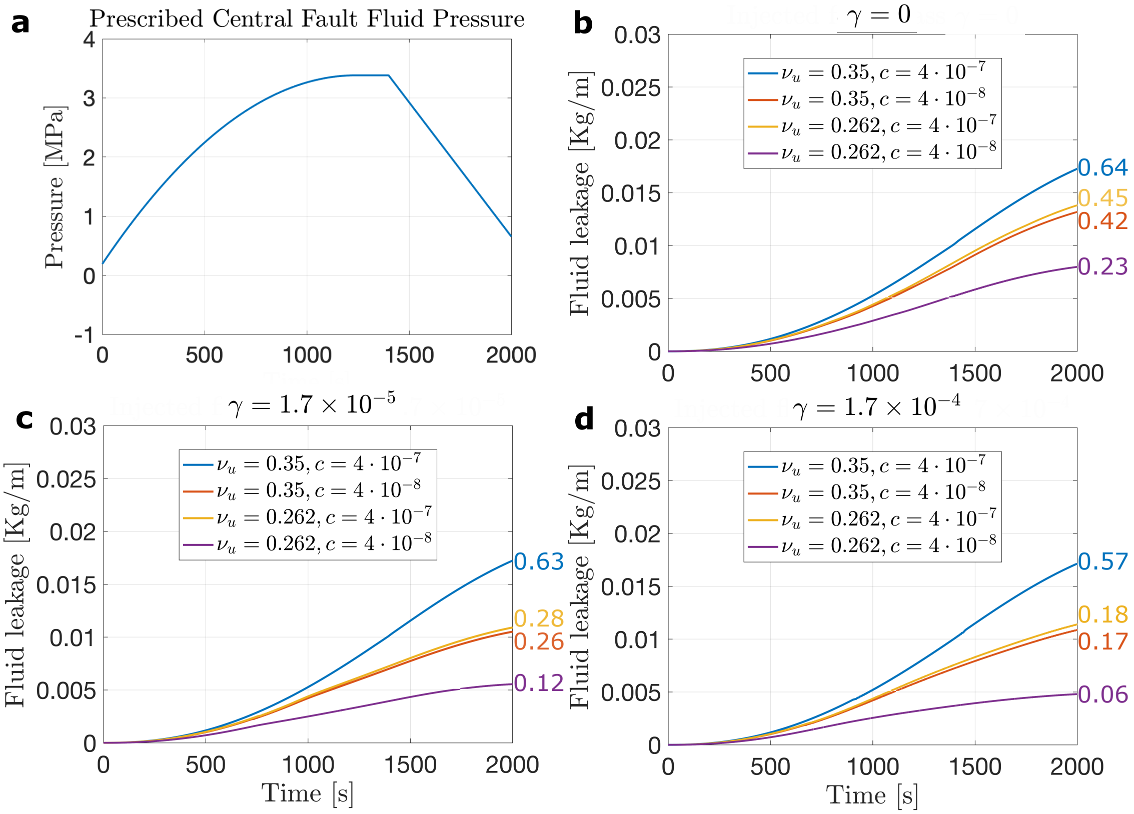

Figure 2.3: Comparison of (a) imposed pressurization at the fault center (a) and (b,c,d) fluid leakoff per unit length in the invariant dimension into the bulk. The numbers in color indicate, at 2000 s, how much net fluid mass had moved into the bulk compared to the injected amount. Substantial lag is observed between fault pressurization and onset of significant leak off. We find that different bulk parameter combinations lead to very different amount of leakage. As dilatancy is introduced (c,d), the net leakoff decreases due to the dilatancy causing flow back into the shear zone from the bulk.

greater influence on leakage than changing the undrained Poisson's ratio, yet the leakage is similar. Changing ν_u from 0.262 to 0.35 increases M by a factor of 2.75, thus, if c is constant, then for consistency $\kappa = c/M$ is reduced by about 1/2.75. For reference, $\kappa = 3.1502 \cdot 10^{-19}$ m^2/(Pa s) when $\nu_u = 0.262$, $c = 4 \cdot 10^{-8}$ m^2/s and thus the bulk mobility κ is about an order of magnitude larger than the mobility $\kappa_{cy} = 8.7584 \cdot 10^{-20}$ m^2/(Pa s) across the shear layer. As mentioned previously, and apparent from inspecting the convolution kernels K_1 and K_2, the flow into the bulk has two timescales $t_b = 1/ck^2$ and $t_f = (\kappa^2 \epsilon^2)/(\kappa_c^2 c)$. We thus see that t_f is reduced by about 0.13. These considerations explain the observed similar leakoff. Further, this highlights the importance of multiple time-scales in the simulated problem and in real faults where multiple diffusion times undoubtedly exist.

When simulations without and with dilatancy are compared (Figure 2.3b vs. Figure 2.3c,d), a consistent behavior is revealed but with the leakage universally reduced as γ is increased, although to a different degree for different simulations. The reduction in net leakage occurs because the dilatancy reduces pressure and causes flow back, or suction, from the bulk into the shear zone.

The following two sections investigate slip behavior as the poroelastic and dilatancy parameters are varied, making some of the effects discussed here even more apparent.

Effects of poroelasticity and bulk diffusivity on slip evolution

First, we explore the simplest case, and the one most studied in the literature, where pore pressure change in the shear zone is introduced by injection and evolves through diffusion, but does not change due to dilatancy. In most cases, this would mean that the pore pressure change is one-way coupled. In other words, the pore pressure changes slip by affecting the frictional strength, but the slip does not change the pore pressure [3, 11, 38]. However, in the case of poroelastic bulk that we are investigating, there is potential for slip to affect the pore fluid pressure even in the absence of dilatancy effect, due to the poroelastic coupling. For example, slip induces changes in pore fluid pressure in the bulk, leading to variations in p^+ and p^- on the boundary between the bulk and the shear layer, affecting both the average pressure in the layer and, eventually p_c through diffusion.

The simulations (Figure 2.4) demonstrate a wide spectrum of slip stability due to variations in two parameters that have not been explored much in the literature: bulk diffusivity and undrained Poisson's ratio. First, in the reference simulations, a smaller undrained Poisson's ratio ν_u and bulk diffusivity c (panel a) results in highly unstable behavior with four seismic ruptures. In contrast, with larger bulk diffusivity c and undrained Poisson's ratio ν_u (panel d) we observe very limited slip in response to the injection. Clearly, the fault is not slipping in a seismically unstable manner. In the two intermediate cases, where one value is larger and the other smaller (panels b and c), we see somewhat stabilized behavior, with three ruptures instead of four and later onset of seismic slip. Clearly, neither parameter alone is controlling the stability characteristics of the fault. We discuss how the undrained parameters can play a significant role in the stability in Section 2.6.

Figure 2.4 shows that although in all cases the average pore pressure in the shear zone is similar, lower average values correlate with increased stability. This is also

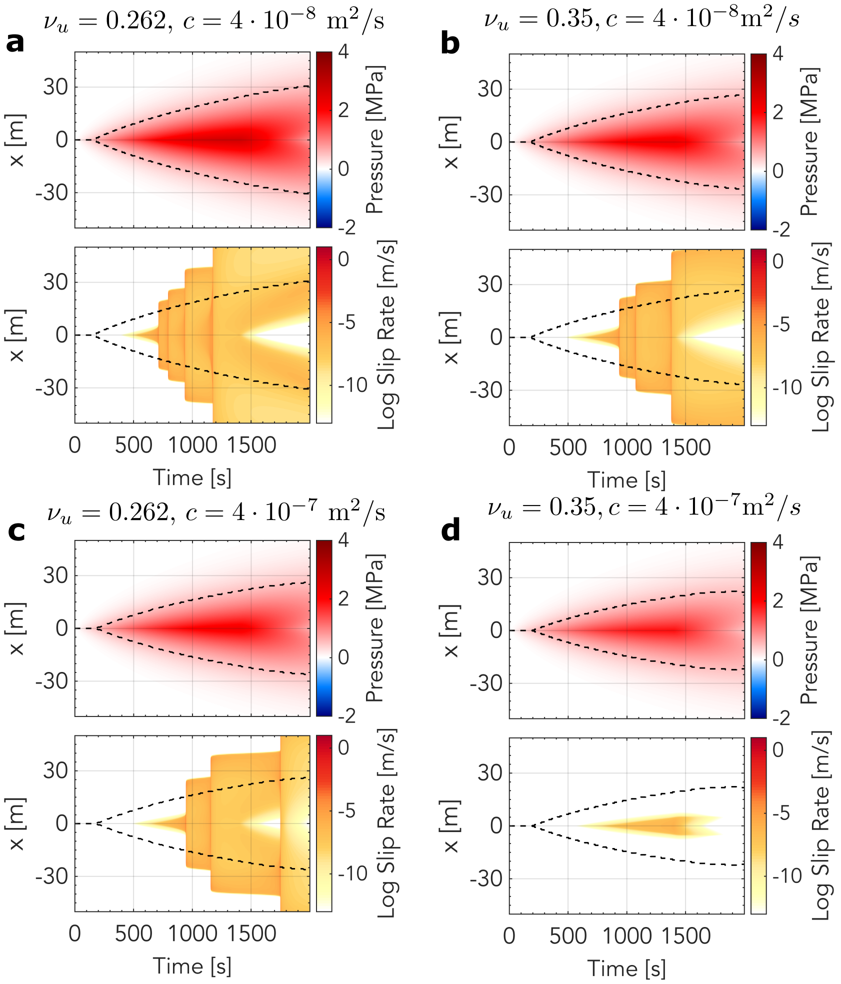

Figure 2.4: Simulations of fault fields with time and space for varied bulk diffusivity c and undrained Poisson's ratio ν_u as listed above each panel (and no dilatancy, $\gamma = 0$). Each panel shows the average shear zone pressure $\langle p \rangle$ and log slip rate $\log_{10} V$. x indicates location along the length of the fault, but we note that the simulation domain is 5 times larger (400 m) than shown. The black dashed lines are the 0.5 MPa pressure contours, which we take as representative of the pressure front distance. The reference simulation with small difference in ν_u and ν and low c shows highly unstable slip in panel (a) (four seismic events). But we observe highly stabilized slip in panel (d), where the undrained Poisson's ratio and bulk diffusivity are larger.

directly reflected in the leakage reported in Figure 2.3b.

While Figure 2.4 offers a good view of the total fault dynamics, it is hard to see the seismic slip rates since dynamic events are short-lived, and the components of the average pressure $\langle p \rangle$ are hidden. Figure 2.5 shows the slip rate and various pressures at $x = 17$ m in the reference simulation (Figure 2.4a), where the first seismic rupture

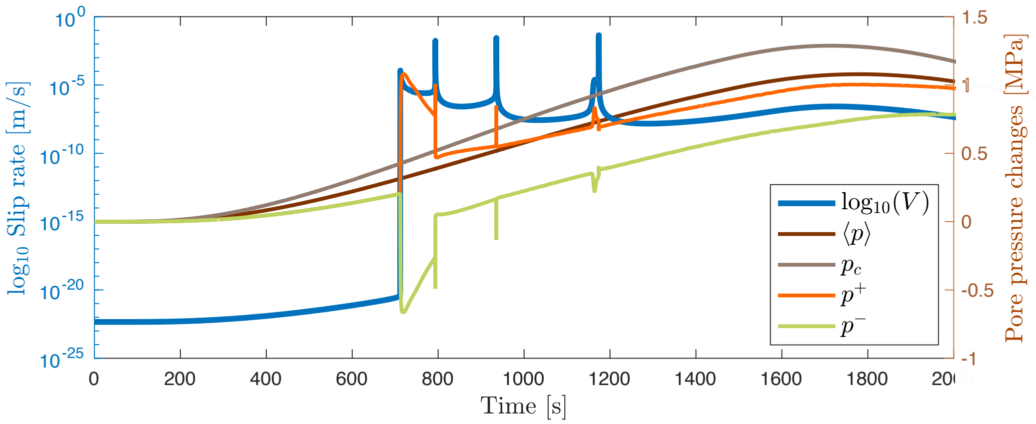

Figure 2.5: Variability of slip rate (blue, left axis) and pore pressure (other colors, right axis) at $x = 17$ m in the reference simulation ($\nu_u = 0.262$, $c = 1.7 \cdot 10^{-8}$ m^2/s, Figure 2.4a).

approximately arrests. The simulated slip rates vary by orders of magnitude, from the near-zero initial values corresponding to a locked fault, to significant slow slip with sustained slip rates of 10^{-7} to 10^{-5} m/s, to dynamic slip rates of the order of 0.1 m/s. Note that the first seismic event is arresting at this fault location, with the peak slip rate of 10^{-4} m/s. We observe a striking dependence of $p^{\pm}$ on the slip, with the jumps in pressure indicating the poroelastic response associated with rapidly spreading rupture. Further, even in the absence of any active rupturing, seen as spikes in slip rate, there are nevertheless substantial differences in the values of p^+, p^-, and p_c. The shear zone half-width is $\epsilon = 1$ mm (Appendix A), and thus the simulation indicates pressure differences around 1 MPa across this thin shear zone. Figure 2.5 shows that our choice of using $\langle p \rangle$ as the relevant pressure when computing the effective normal stress is quite conservative as it averages out significant part of the poroelastically induced pressure change, especially during episodes of rapid slip.

Combined effects of poroelasticity and dilatancy

Here we explore the same parameter combinations, initial conditions, imposed injection, and overall setup as in the previous section. However, we now include dilatancy with $\gamma = 1.7 \cdot 10^{-5}$ first (Figure 2.6) and then $\gamma = 1.7 \cdot 10^{-4}$. The latter value was derived by [60] from the experiments of [44]. $\gamma = 1.7 \cdot 10^{-4}$ is typically used in the literature. We explore a smaller value as well, since it reveals an intermediate regime and there is no general reason to believe that the dilatancy coefficient could not vary significantly.

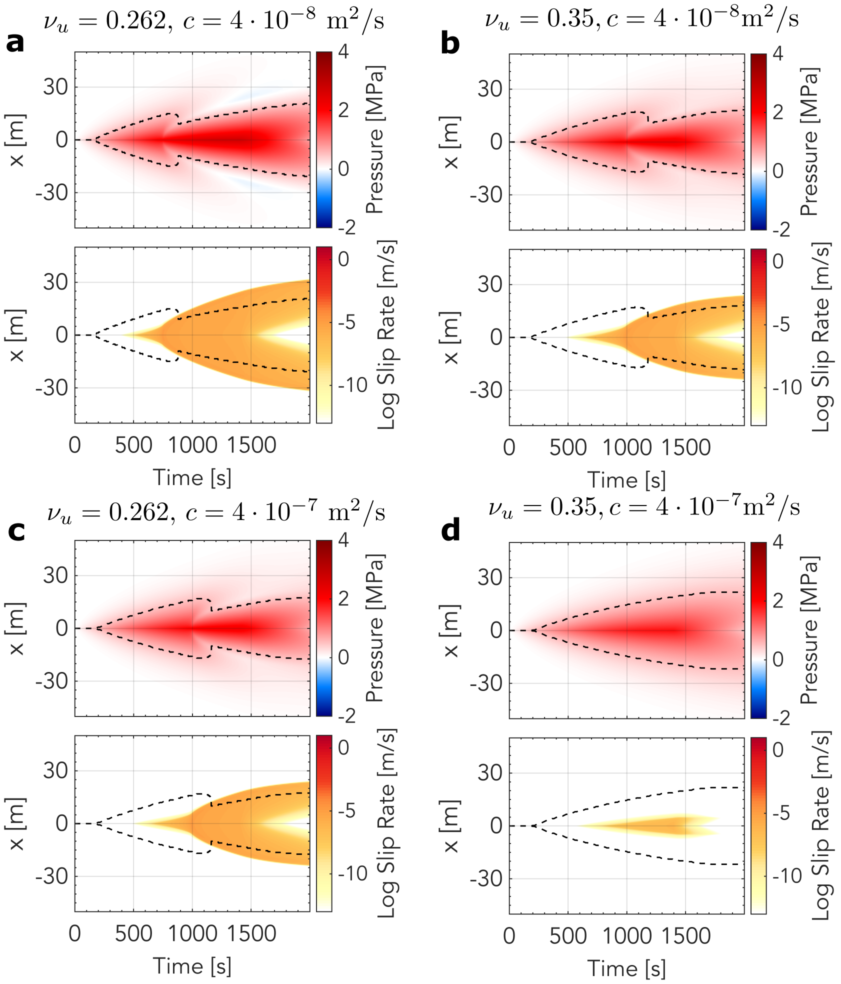

Figure 2.6: Simulations of fault fields with time and space for varied bulk diffusivity c and undrained Poisson's ratio ν_u as listed above each panel, with dilatancy $\gamma = 1.7 \cdot 10^{-5}$. The panels and simulation setup are the same as in Figure 2.4 but with dilatancy. We observe highly stabilized slip in panel d, where the undrained Poisson's ratio and the bulk diffusivity are larger. Overall, the results are largely consistent with those of Figure 2.4, where panel (d) shows the most stable behavior, panel (a) is the least stable, and parameter combinations in panels (b) and (c) show intermediate stability. However, here all simulations show gradual migration of a slow slip front and no seismic event. Thus all simulations are substantially stabilized, as expected from introducing dilatancy. We note negative pore pressure change at the slip-front in panel (a) (blue colors), and strong overall deviation from the square-root characteristic growth of the pore pressure front.

Notable in Figure 2.6 are similar effects of slip stabilization due to increasing c and ν_u, as in Figure 2.4. However, with even relatively mild dilatancy, the style of slip is very different. We observe no seismic events but slow slip migration, with significant stabilization of slip by dilatancy as expected from prior studies [60, 62, 19]. In all cases, except panel (d), the slow slip eventually outpaces the pore pressure front as indicated by the dashed 0.5 MPa contour. However, the slip closely tracks the contour, which suggests that a different definition of the pore pressure front - i.e., with a lower threshold than 0.5 MPa - may actually lead to slip and pore pressure front being nearly coincident.

Strikingly, the slip in the presence of dilatancy is drastically altering the pore pressure front. The influence of dilatancy on the fault pore pressure is most prominent in panel a, where the average pressure at the rupture tip is decreased compared to a background value, i.e., negative pore pressure change. Furthermore, the pore pressure front does not follow the classic square-root-of-time diffusion profile seen in Figure 2.4 and Figure 2.6d. Rather, the profile is square-root characteristic initially, but once the slip rate is significant, the dilatancy decreases the pore pressure and effectively creates suction at the tip, leading to the perturbed pore pressure front. The resulting shape of the fault pore pressure contour resembles the outline of a squid's head. As seen in Figure 2.3, inclusion of a non-zero γ reduces the net leak-off into the bulk. Figure 2.6 demonstrates why, with the dilatancy-induced pore pressure change causing mass transfer into the fault from the bulk. Our simulations thus show agreement with the theorized flow into the rupture tip from the bulk [8]. Lateral flow from the adjacent shear zone is likely also occurring [16], but it cannot be the only transfer since that would not affect the net leakoff into the bulk. The case of Figure 2.6d is already very stabilized by the choices of ν_u and c and thus dilatancy does not play a significant stabilizing role. This explains why the blue leakage curve in Figure 2.3 is not much influenced by the dilatancy.

Finally, we show simulations using the value of the dilatancy coefficient $\gamma = 1.7 \cdot 10^{-4}$ as inferred by [60].

For $\gamma = 1.7 \cdot 10^{-4}$, the slip is further stabilized (Figure 2.7). There is no seismic rupture and the slow slip front is well within the region of the pore pressure increase, except in the case of panel a where the slow slip catches up with the pore pressure front towards the end of the simulation. In other words, the rupture is driven by high pore pressure and thus grows quasi-statically within the pressure front. Compared to Figure 2.6, we observe significant additional dilatancy-induced changes in pore pressure, with the extent and values of pore pressure in the pressurized zone significantly modified and generally reduced. Yet the non-monotonic pore-pressure front features are less prominent in Figure 2.7, with the exception of case (a) where

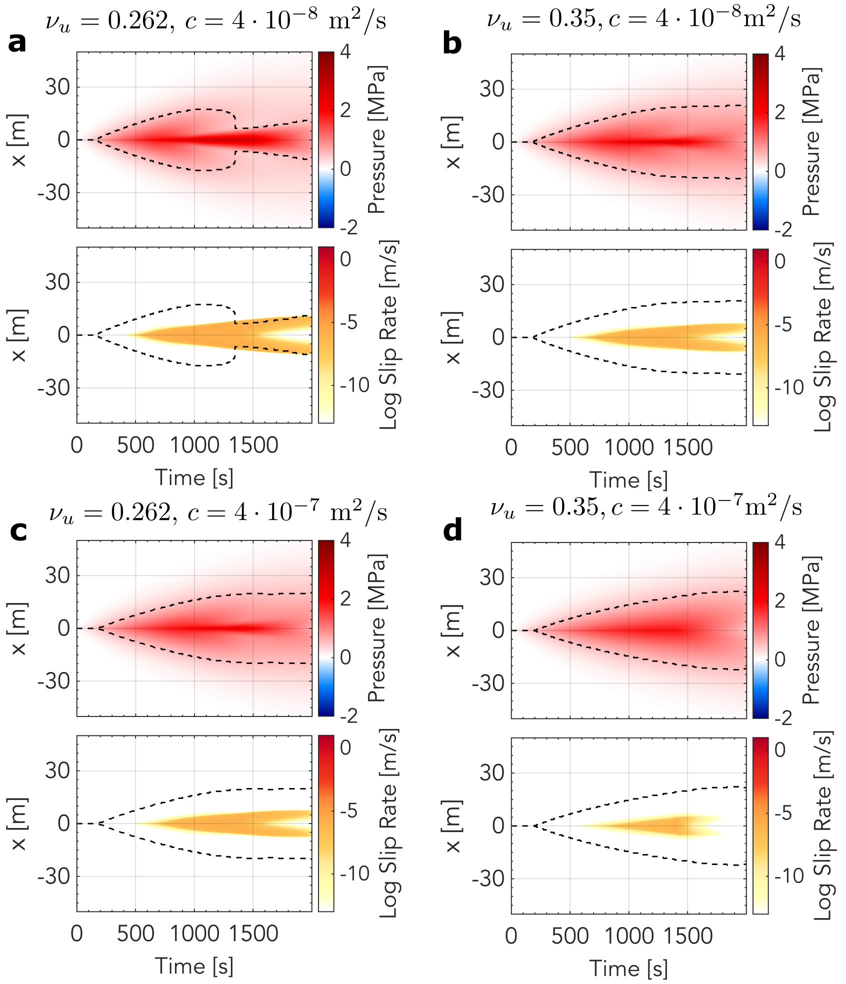

Figure 2.7: Simulations of fault fields with time and dilatancy $\gamma = 1.7 \cdot 10^{-4}$. Otherwise the figures and simulation setup is the same as in Figure 2.4. We observe highly stabilized slip in all cases. Unlike the previous two cases, the rupture only grows in a region of significantly elevated pore pressure.

they are similar. This may be somewhat counter-intuitive given that the dilatancy coefficient is an order of magnitude larger in Figure 2.7. However, the effect of dilatancy also depends on the slip rates that are able to develop. The case of Figure 2.7a is still the most unstable due to the choices of ν_u and c, and hence the dilatancy has a more pronounced effect on the shape of the rupture front. Since the dilatancy coefficient is smaller in Figure 2.6, a larger slip patch can develop before the stabilization becomes significant. This slip patch is less stiff or alternatively one might state that it produces a higher energy release rate. Thus it is able to drive rupture propagation at a higher slip rate, which ultimately results in increased pore pressure response at the front than when the dilatancy coefficient is larger and suppresses instability development at an earlier time.

We emphasize that selecting $\gamma = 1.7 \cdot 10^{-4}$ does not generally mean unconditionally stable ruptures. One could achieve seismic rupture by choosing a more rate-weakening (and hence instability-promoting) friction properties or by altering the injection strategy; for example, injecting at a higher rate may lead to a seismic event [28].

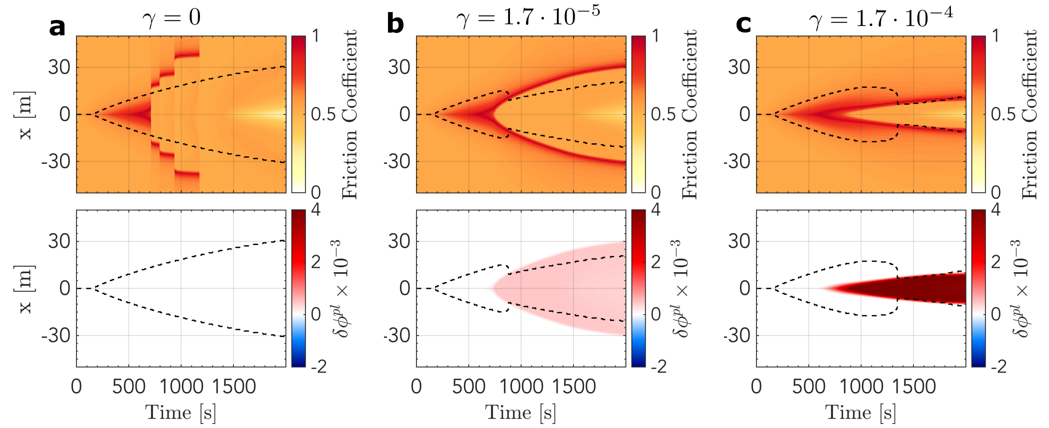

Figure 2.8: Changes in the coefficient of friction and inelastic dilatancy for $\nu_u = 0.262$ and $c = 4\cdot10^{-8}$ m^2/s as γ is varied. Panel (a) represents the reference simulation without any dilatancy. We see that the largest change in porosity from inelastic dilatancy is about 0.004, which is substantially less than the reference value of 0.068.

For further insight, we explore how the friction coefficient and change in inelastic dilatancy evolve in space and time for the reference case of poroelastic properties (Figure 2.8). For cases with inelastic dilatancy, we observe that change in inelastic dilatancy is occurring nearly uniformly within the ruptured part of the fault (Figure 2.8bc), in particular in the time span of 1000 s to 1500 s before the pressure is lowered again. Contrasting Figure 2.8b and 2.6a shows clearly that the average pore pressure is not uniform and primarily dropping at the rupture tip. Note that the p_c value is prescribed between $x = \pm 0.5$ as described in Figure 2.3a, but this does not mean that $\langle p \rangle$ (which is plotted) is constant, due to bulk leakoff affecting $p^{\pm}$. We can deduce that the inflow back from the bulk and through injection maintains pressure within the ruptured region except at the propagating tip. This suggests that the propagation of the rupture tip may depend on how fast fluids can diffuse into the tip region [16, 8]. We suggest that further simulations and analysis that incorporates rate-and-state effects are needed to fully understand this phenomenon.

The work by [26] may offer a useful starting point for such analysis, however, our results indicate that the addition of dilatancy and bulk diffusion significantly affect the phenomenon. Moreover, such analysis would have to grapple with healing and other effects of rate-and-state friction that make the evolution of the friction coefficient qualitatively different from linear slip weakening. For example, consider how the friction coefficient varies with slip at the center point for one simulation with several seismic events (Figure 2.9). The initial rupture shows friction behavior analogous to linear slip-weakening friction, but subsequent ruptures show behavior that cannot be modeled with the same linear slip-weakening friction since the peak frictional strength is clearly strongly history-dependent. In this particular case, we observe non-monotonic peak strength as slip accumulates. This reflects in part differences in time-dependent healing, with the first event occurring on a well-healed fault, and then the time between the third and second rupture being larger than between the second and first ones (Figure 2.9b inset). It also depends on how abrupt the increase of slip rate is at the rupture front, with sharper increases (as in the third event vs. the second event) corresponding to a larger direct effect.

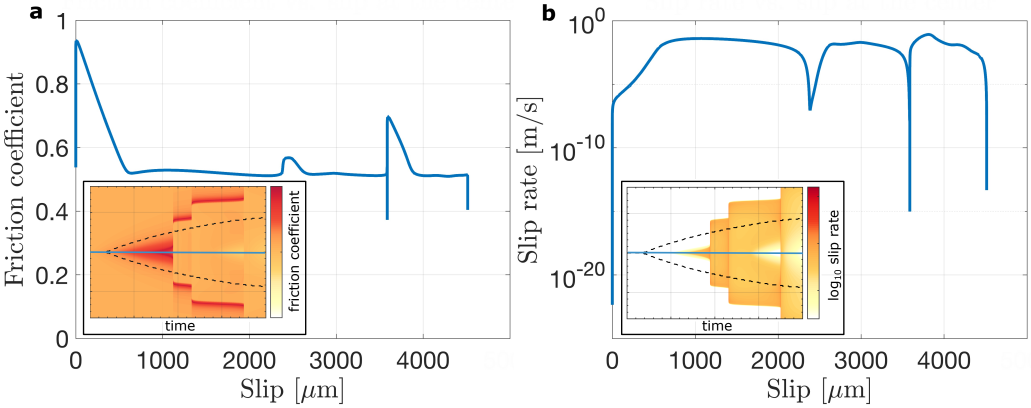

Figure 2.9: Changes in (a) friction coefficient and (b) slip rate as a function of slip at the mid-point of the fault ($x = 0$) with $\nu_u = 0.262$, $c = 1.7 \cdot 10^{-7}$ m^2/s, $\gamma = 0$ (also shown in Figure 2.4c). Insets show the corresponding space-time evaluations, with the blue line marking the location of the center point, inset scales are the same as in Figures 2.4 and 2.8. The observed evolution of the friction coefficient suggests significant differences from a simpler linear slip-weakening model, with a clear history dependence of the peak frictional strength.

2.6 Discussion

The application of our method has had two main themes. First, how altering the bulk diffusivity and undrained Poisson's ratio influences the fault slip response from fluid injection. Second, how dilatancy affects the fault response due to injection. Dilatancy is already understood to be a stabilizing mechanism [55, 60, 62], although only a limited study of coupled injection and dilatancy has been carried out [16, 72]. Thus our general finding, that fault slip is stabilized and aseismic slip is promoted when dilatancy is included is not surprising. We have thus chosen to contrast this well-known stabilizing mechanism with less explored parameters that we are uniquely positioned to investigate with the method described in this paper. Namely we vary parameters c and ν_u. Indeed the latter has meaning only for a poroelastic solid. A purely elastic solid, as considered in most studies, with some exceptions, e.g., [36, 66, 33] has only a single Poisson's ratio.

Our selection of three different γ values that parameterize dilatancy reveals different modes of rupture. First, highly unstable response with repeated seismic ruptures of the same part of the fault. Second, slow, quasi-static slip migration that propagates at the boundaries and perhaps beyond the pressurized region, depending on its definition. Finally, quasi-statically growing slip only in regions of high pressure. This can be observed in Figures 2.4, 2.6, and 2.7, respectively. The [29] experiment reported primarily aseismic slip and significant dilatant behavior. Some micro-earthquakes were reported, but they seemed to occur off the main fault and represent only a small fraction of the moment released. Thus our findings show, given the experimental constraints and information from a previous modeling study [38], that inclusion of dilatancy results in behavior qualitatively similar to what was reported by [29]. However, further study is needed for quantitative matching. We highlight that the method presented predicts fault opening from dilatancy or pressurization and thus may provide additional constraints in data application when that is directly measured [11].

Our reported influence of bulk diffusivity and undrained Poisson's ratio is more novel. We observe that increasing the bulk diffusivity by an order of magnitude significantly stabilizes the fault in the simulations, even in the absence of dilatancy. It is important to emphasize that this result is also contingent on the shear zone mobility, which we have not varied. This is due to the time scales of fluid diffusion in the bulk and shear zone not being independent as discussed by [34]. The bulk diffusivity has an important control on the stability of the fault as it controls how rapidly fluids can escape the shear zone. It thus controls the average pressure of the shear zone even though we maintain a fixed injection pressure. Our parameter choices (Appendix A) are such that we consider a fault initially far from steady-state or, in other words, not critically stressed. Although the changes in average pressure in Figures 2.4, 2.6, and 2.7 are subtle, they are sufficient to cause significant stabilization in fault behavior. This can be observed by comparing panels b and d, or a and c in Figures 2.4, 2.6, and 2.7.

Bulk diffusivity is often considered to be the same as that of the shear zone or the bulk is simply taken to be impermeable. In this study, we have taken what we consider to be small values of $c \sim 10^{-8} - 10^{-7}$ m^2/s, yet we observe a very significant effect with significant stabilisation at higher diffusivity. Granites are more likely to fall into the $c \sim 10^{-5} - 10^{-6}$ m^2/s and many rocks types are even more diffusive except shales that can have $c \sim 10^{-7}$ m^2/s [12]. Further, as seen in equation (2.26), the flux into the bulk scales with κ_{cy}/ϵ^2. Since we expect ϵ, the shear zone half-thickness, to be small, we can expect that flux into the bulk occurs rapidly. Indeed, in this study, we set the κ_{cx}, along shear zone mobility, to be a factor 10^9 larger than κ_{cy} such that the fluid migration along the shear zone is significant compared to the flux into the bulk. This highlights that how rapidly the bulk can transport fluids is critical for the fault dynamics. As discussed in [34], and can be seen in the SBI solutions in this paper, the characteristic time of bulk diffusion is $\sim 1/(ck^2)$. Thus the bulk fluid transport is highly dependent on the length scale, and idealizations of an impermeable bulk may only be valid at a certain length scale.

The dependence on the undrained Poisson's ratio may be surprising, and it may not be clear why having a pronounced undrained poroelastic response would result in a greater stabilization. As we discussed in relation to Figure 2.3, changing ν_u but keeping c fixed requires that κ is reduced. Thus the t_f (equation 2.47), the timescale that fluids can move or flow through the shear zone, is changed but not t_b (equation 2.46), the time scale of fluid migration in the bulk. Thus by changing ν_u we increase the speed of fluid flow in the shear zone, which could lead to more rapid leakoff into the bulk and lower shear zone pressure.

But is this the only influence of changing ν_u? The analysis of [34] provides some insight. The undrained critical wavenumber is

$$|k_{cr}^{un}| \simeq \frac{2\sigma_0(b-a)(1-\nu_u)}{GD_{RS}}\left(1 - \frac{f_0\gamma}{\beta\sigma_0(b-a)} + O(\epsilon)\right), \tag{2.57}$$

and the corresponding drained wavenumber is

$$|k_{cr}^{d}| \simeq \frac{2\sigma_0(b-a)(1-\nu)}{GD_{RS}}\left(1 - \frac{f_0\gamma}{\beta\sigma_0(b-a)} + O(\epsilon)\right), \tag{2.58}$$

assuming the shear zone mobility tends to zero. Thus, the ratio of the minimum unstable wavelengths in the drained and undrained limits is

$$\frac{\lambda_d}{\lambda_{un}} = \frac{1-\nu}{1-\nu_u}. \tag{2.59}$$

Thus, at most, this ratio can be 2, but more commonly around 1 – 1.5. In simple terms, it means that a perturbation or a slip patch on the fault of length ΔL may be unstable if the bulk responds in a drained manner. However, the patch or perturbation may need to be up to $2\Delta L$ to be unstable if the bulk responds in an undrained manner. There are a few things to note about this stabilization. First, the transition from a drained to undrained response depends on the characteristic bulk and shear zone diffusion times t_b and t_f relative to how fast the fault is slipping and the slip patch length scale (due to the k^2 dependence of t_b). Thus the timing of stabilization by a transition from drained to undrained response is nontrivial. Second, the drained and undrained limits are inadequate to characterize the stabilization fully. [34] showed that, in an intermediate (neither drained nor undrained) regime, the fault could be more stable than in the undrained regime. Finally, since anti-plane sliding does not depend on Poisson's ratio, the same kind of stabilization would not occur in Mode III. This may lead to interesting directional effects in 3D simulations.

In summary, changing an undrained poroelastic parameter not only influences the fluid flow and the undrained elastic response but also the timing when the fault slip can be considered undrained. We suspect that this feedback may sometimes lead to surprising and even counter-intuitive stability characteristics and needs careful consideration in future work.

Panels b and c in Figures 2.4, 2.6, and 2.7 consistently show similar rupture propagation and stabilization. This suggests that, in a certain sense, that setting $\nu_u = 0.35$ is approximately equally stabilizing as setting $c = 4\cdot 10^{-7}$ m^2/s relative to the respective lower values in the simulation setup. Due to the many complexities mentioned in the previous paragraph, we do not expect this to hold generally. However, simulations with combined $\nu_u = 0.35$ and $c = 4\cdot 10^{-7}$ m^2/s are nearly identical regardless of the γ value (panels d in Figures 2.4, 2.6, and 2.7). This observation highlights that the bulk effects, through combined diffusion and poroelasticity, can be so stabilizing that dilatancy cannot become significant enough to affect the rupture propagation and nucleation.

While we do not aim to precisely match the fault slip observed in the field experiment of [29], it is clear that multiple models would be able to reproduce the stable slip measured in the injection site during the experiment. The study of [38] already found multiple potential parameter sets that match the observed slip behavior nearly identically, by varying the friction properties and along-fault diffusivity. Given the significant stabilizing effects of bulk diffusivity, undrained Poisson's ratio, and dilatancy, none of which were included in [38] - it is clear that many additional models can be created, for example, by choosing more unstable fault friction properties and adding one or more of the stabilizing mechanisms discussed in this study. To distinguish between different possible models, we need field experiments with multiple measurement locations of pore fluid pressure and slip/deformation.

For example, one distinguishing characteristic that highlights the interaction of poroelastic effects with dilatancy is the non-standard, non-monotonic evolution of the pore-pressure front that we observe, as in Figures 2.6-2.7. Dilatancy, and the associated reduction in pore fluid pressure, is not uniform along the slipping fault but rather is strongly affected by the slip-rate spatio-temporal distribution. Hence it can create local suction that induces pore fluid flow reversals, which in turn would depend on the transport and poroelastic properties. Additional measurements away from the injection location would thus help constrain the range of applicable models.

One important observation from our simulations is how a single injection can cause multiple seismic re-ruptures of the same part of the fault (Figure 2.4). With each re-rupture, the lateral extent of the rupture increases and the probability of a runaway rupture, which is not confined to the high pore pressure region, increases as well. If observed in injection experiment, such re-rupturing pattern may be a precursor for a runaway rupture and thus may be important to analyze further. We see that during such repeated rupturing the frictional strength is not well explained by the simpler linear slip-weakening friction law (Figure 2.9) or other friction laws where healing is not accounted for. This fact challenges most common analysis strategies applied to injection induced frictional slip used today [27, 16, 26, 8, 68, 57, 17] if intended for analyzing repeated ruptures on the same interface. However, the initial rupture may be well explained by linear slip weakening, provided its parameters are chosen to account for pre-slip healing (which changes the effective slip-weakening behavior, e.g., the peak friction), and those methods would work well to understand, for example, how far the rupture propagates. Note, however, that there are alternative formulations of rate-and-state friction, with different state-variable evolution laws such as the slip law [56] as well as various composite laws, and the formulation that best describes various laboratory experiments is a topic of ongoing research [4, 5]. The slip law, in particular, results in non-linear effective slip weakening of friction at the rupture tip [1]. The effect of the alternative rate-and-state formulations on the fault slip due to fluid injection can be studied by the approach developed in this work and the code provided (see Data Availability Statement) incorporates both aging and slip law.

2.7 Conclusions

We have presented novel spectral boundary-integral (SBI) solutions applicable to frictional and fracture mechanics problems in a plane-strain linear poroelastic solid. The solutions consider that the interface of two poroelastic half-spaces may undergo mode I and II displacement discontinuity as well as pressurization. We have applied the solutions to develop a method and code implementation of a rate-and-state fault that has simultaneous poroelastic bulk repsonse, inelastic dilatancy, and injection. We apply this code to data from a field experiment, which has been previously analyzed by modeling. We explore the role of bulk diffusion and poroelastic properties of the bulk with and without inelastic dilatancy of the gouge. We find, surprisingly, that bulk diffusion and poroelastic properties of the bulk, which are parameters that are rarely explored, can qualitatively affect rupture stability and propagation. Further, we find the stabilization by bulk diffusion and poroelastic properties can be comparable to the well-known stabilizing dilatancy mechanism. We find that dilatancy can strongly alter the pore presssure distribution on the fault as slip evolves which, if measured, would help constrain hydrological and mechanical properties of the fault and bulk. A further numerical and analytical study is needed to fully characterize the different stability regimes that we have observed. However, our results show that a rich spectrum of slip behavior can be obtained during injection into a fault depending on bulk properties that are frequently left out in previous studies.

References

[1] J.-P. Ampuero and A. M. Rubin. “Earthquake nucleation on rate and state faults – Aging and slip laws.” In: *Journal of Geophysical Research: Solid Earth* 113.B1 (2008). DOI: `https://doi.org/10.1029/2007JB005082`.

[2] Y. Ben-Zion and J. R. Rice. “Dynamic simulations of slip on a smooth fault in an elastic solid.” In: *Journal of Geophysical Research: Solid Earth* 102.B8 (1997), pp. 17771–17784. DOI: `https://doi.org/10.1029/97JB01341`.

[3] P. Bhattacharya and R. C. Viesca. “Fluid-induced aseismic fault slip outpaces pore-fluid migration.” In: *Science* 364.6439 (2019), pp. 464–468. ISSN: 0036-8075. DOI: `10.1126/science.aaw7354`.

[4] P. Bhattacharya et al. “Critical evaluation of state evolution laws in rate and state friction: Fitting large velocity steps in simulated fault gouge with time-, slip-, and stress-dependent constitutive laws.” In: *Journal of Geophysical Research: Solid Earth* 120.9 (2015), pp. 6365–6385.

[5] P. Bhattacharya et al. “The evolution of rock friction is more sensitive to slip than elapsed time, even at near-zero slip rates.” In: *Proceedings of the National Academy of Sciences* 119.30 (2022), e2119462119. DOI: `10.1073/pnas.2119462119`.

[6] A. Bizzarri and M. Cocco. “A thermal pressurization model for the spontaneous dynamic rupture propagation on a three-dimensional fault: 1. Methodological approach.” In: *Journal of Geophysical Research: Solid Earth* 111.B5 (2006). DOI: `https://doi.org/10.1029/2005JB003862`.

[7] W. F. Brace, B. W. Paulding Jr., and C. Scholz. “Dilatancy in the fracture of crystalline rocks.” In: *Journal of Geophysical Research (1896-1977)* 71.16 (1966), pp. 3939–3953. DOI: `https://doi.org/10.1029/JZ071i016p03939`.

[8] N. Brantut. “Dilatancy toughening of shear cracks and implications for slow rupture propagation.” In: *Journal of Geophysical Research: Solid Earth* 126.11 (2021), e2021JB022239. DOI: `https://doi.org/10.1029/2021JB022239`.

[9] R. Bürgmann. “The geophysics, geology and mechanics of slow fault slip.” In: *Earth and Planetary Science Letters* 495 (2018), pp. 112–134.

[10] J. S. Caine, J. P. Evans, and C. B. Forster. “Fault zone architecture and permeability structure”. In: *Geology* 24.11 (Nov. 1996), pp. 1025–1028. ISSN: 0091-7613. DOI: `10.1130/0091-7613(1996)024<1025:FZAAPS>2.3.CO;2`.

[11] F. Cappa et al. “Stabilization of fault slip by fluid injection in the laboratory and in situ.” In: *Science Advances* 5.3 (2019), eaau4065. DOI: `10.1126/sciadv.aau4065`.

[12] A. H.-D. Cheng. *Poroelasticity.* Vol. 877. Springer, 2016.

[13] A. H.-D. Cheng and E. Detournay. “On singular integral equations and fundamental solutions of poroelasticity.” In: *International Journal of Solids and Structures* 35.34 (1998), pp. 4521–4555. ISSN: 0020-7683. DOI: `https://doi.org/10.1016/S0020-7683(98)00082-1`.

[14] A. H.-D. Cheng and E. Detournay. “A direct boundary element method for plane strain poroelasticity.” In: *International Journal for Numerical and Analytical Methods in Geomechanics* 12.5 (1988), pp. 551–572. DOI: `https://doi.org/10.1002/nag.1610120508`.

[15] A. H.-D. Cheng and J. A. Liggett. “Boundary integral equation method for linear porous-elasticity with applications to fracture propagation.” In: *International Journal for Numerical Methods in Engineering* 20.2 (1984), pp. 279–296. DOI: `https://doi.org/10.1002/nme.1620200207`.

[16] F. Ciardo and B. Lecampion. “Effect of Dilatancy on the Transition From Aseismic to Seismic Slip Due to Fluid Injection in a Fault.” In: *Journal of Geophysical Research: Solid Earth* 124.4 (2019), pp. 3724–3743. DOI: `https://doi.org/10.1029/2018JB016636`.

[17] F. Ciardo and A. P. Rinaldi. “Impact of injection rate ramp-up on nucleation and arrest of dynamic fault slip.” In: *Geomechanics and Geophysics for Geo-Energy and Geo-Resources* 8.1 (2022), pp. 1–27. DOI: `https://doi.org/10.1007/s40948-021-00336-4`.

[18] M. Cocco and J. R. Rice. “Pore pressure and poroelasticity effects in Coulomb stress analysis of earthquake interactions.” In: *Journal of Geophysical Research: Solid Earth* 107.B2 (2002), ESE 2-1-ESE 2–17. DOI: `https://doi.org/10.1029/2000JB000138`.

[19] L. Dal Zilio, N. Lapusta, and J.-P. Avouac. “Unraveling scaling properties of slow-slip events.” In: *Geophysical Research Letters* 47.10 (2020). DOI: `10.1029/2020GL087477`.

[20] E. Detournay and A. H.-D. Cheng. “Fundamentals of poroelasticity.” In: *Analysis and Design Methods.* Elsevier, 1995, pp. 113–171.

[21] J. H. Dieterich. “Modeling of rock friction: 1. Experimental results and constitutive equations.” In: *Journal of Geophysical Research: Solid Earth* 84.B5 (1979), pp. 2161–2168. DOI: `10.1029/JB084iB05p02161`.

[22] P. Dublanchet. “Fluid driven shear cracks on a strengthening rate-and-state frictional fault.” In: *Journal of the Mechanics and Physics of Solids* 132 (2019), p. 103672. ISSN: 0022-5096. DOI: `https://doi.org/10.1016/j.jmps.2019.07.015`.

[23] C. E. Duchon. “Lanczos filtering in one and two dimensions.” In: *Journal of applied meteorology* 18.8 (1979), pp. 1016–1022.

[24] E. M. Dunham and J. R. Rice. “Earthquake slip between dissimilar poroelastic materials.” In: *Journal of Geophysical Research: Solid Earth* 113.B9 (2008). B09304. ISSN: 2156-2202. DOI: `10.1029/2007JB005405`.

[25] W. L. Ellsworth. “Injection-induced earthquakes.” In: *Science* 341.6142 (2013), p. 1225942.

[26] D. I. Garagash. “Fracture mechanics of rate-and-state faults and fluid injection induced slip.” In: *Philosophical Transactions of the Royal Society A: Mathematical, Physical and Engineering Sciences* 379.2196 (2021), p. 20200129. DOI: `10.1098/rsta.2020.0129`.

[27] D. I. Garagash and L. N. Germanovich. “Nucleation and arrest of dynamic slip on a pressurized fault.” In: *Journal of Geophysical Research: Solid Earth* 117.B10 (2012). DOI: `https://doi.org/10.1029/2012JB009209`.

[28] M. Gori et al. “Dynamic rupture initiation and propagation in a fluid-injection laboratory setup with diagnostics across multiple temporal scales.” In: *Proceedings of the National Academy of Sciences* 118.51 (2021), e2023433118. DOI: `10.1073/pnas.2023433118`.

[29] Y. Guglielmi et al. “Seismicity triggered by fluid injection–induced aseismic slip.” In: *Science* 348.6240 (2015), pp. 1224–1226. DOI: `10.1126/science.aab0476`.

[30] J. C. Hawthorne and A. M. Rubin. “Laterally propagating slow slip events in a rate and state friction model with a velocity-weakening to velocity-strengthening transition.” In: *Journal of Geophysical Research: Solid Earth* 118.7 (2013), pp. 3785–3808. DOI: `https://doi.org/10.1002/jgrb.50261`.

[31] E. R. Heimisson. *eliasrh/Poro_SBIM: Poro_SBIM_v1.0*. Version v1.0. Feb. 2022. DOI: `10.5281/zenodo.6010353`. URL: `https://doi.org/10.5281/zenodo.6010353`.

[32] E. R. Heimisson and A. P. Rinaldi. “Spectral boundary integral method for simulating static and dynamic fields from a fault rupture in a poroelastodynamic solid.” In: *Geomechanics and Geophysics for Geo-energy and Geo-resources* 8.2 (2022), pp. 1–20. DOI: `https://doi.org/10.1007/s40948-022-00368-4`.

[33] E. R. Heimisson, E. M. Dunham, and M. Almquist. “Poroelastic effects destabilize mildly rate-strengthening friction to generate stable slow slip pulses.” In: *Journal of the Mechanics and Physics of Solids* (2019). DOI: `10.1016/j.jmps.2019.06.007`.

[34] E. R. Heimisson, J. Rudnicki, and N. Lapusta. “Dilatancy and Compaction of a Rate-and-State Fault in a Poroelastic Medium: Linearized Stability Analysis.” In: *Journal of Geophysical Research: Solid Earth* 126.8 (2021), e2021JB022071. DOI: `https://doi.org/10.1029/2021JB022071`.

[35] P. A. Hsieh and J. D. Bredehoeft. “A reservoir analysis of the Denver earthquakes: A case of induced seismicity.” In: *Journal of Geophysical Research: Solid Earth* 86.B2 (1981), pp. 903–920. DOI: `https://doi.org/10.1029/JB086iB02p00903`.

[36] B. Jha and R. Juanes. “Coupled multiphase flow and poromechanics: A computational model of pore pressure effects on fault slip and earthquake triggering.” In: *Water Resources Research* 50.5 (2014), pp. 3776–3808. DOI: `10.1002/2013WR015175`.

[37] N. Lapusta et al. “Elastodynamic analysis for slow tectonic loading with spontaneous rupture episodes on faults with rate- and state-dependent friction.” In: *Journal of Geophysical Research: Solid Earth* 105.B10 (2000), pp. 23765–23789. DOI: `https://doi.org/10.1029/2000JB900250`.

[38] S. Larochelle et al. “Constraining Fault Friction and Stability With Fluid-Injection Field Experiments.” In: *Geophysical Research Letters* 48.10 (2021), e2020GL091188. DOI: `https://doi.org/10.1029/2020GL091188`.

[39] J. Leeman et al. “Laboratory observations of slow earthquakes and the spectrum of tectonic fault slip modes.” In: *Nature Communications* 7.1 (2016), pp. 1–6. DOI: `https://doi.org/10.1038/ncomms11104`.

[40] Y. Liu and J. R. Rice. “Aseismic slip transients emerge spontaneously in three-dimensional rate and state modeling of subduction earthquake sequences.” In: *Journal of Geophysical Research: Solid Earth* 110.B8 (2005). DOI: `https://doi.org/10.1029/2004JB003424`.

[41] Y. Liu and J. R. Rice. “Spontaneous and triggered aseismic deformation transients in a subduction fault model.” In: *Journal of Geophysical Research: Solid Earth* 112.B9 (2007). DOI: `https://doi.org/10.1029/2007JB004930`.

[42] X. Ma et al. “Multi-disciplinary characterizations of the BedrettoLab – a new underground geoscience research facility”. In: *Solid Earth* 13.2 (2022), pp. 301–322. DOI: `10.5194/se-13-301-2022`. URL: `https://se.copernicus.org/articles/13/301/2022/`.

[43] C. Marone. “Laboratory-derived friction laws and their application to seismic faulting.” In: *Annual Review of Earth and Planetary Sciences* 26.1 (1998), pp. 643–696.

[44] C. Marone, C. B. Raleigh, and C. H. Scholz. “Frictional behavior and constitutive modeling of simulated fault gouge.” In: *Journal of Geophysical Research: Solid Earth* 95.B5 (1990), pp. 7007–7025. DOI: `10.1029/JB095iB05p07007`.

[45] J. McNamee and R. E. Gibson. “Plane strain and axially symmetric problems of the consolidation of a semi-infinite clay stratum.” In: *The Quarterly Journal of Mechanics and Applied Mathematics* 13.2 (1960), pp. 210–227.

[46] H. Noda and N. Lapusta. “Stable creeping fault segments can become destructive as a result of dynamic weakening.” In: *Nature* 493.7433 (2013), pp. 518–521. DOI: `https://doi.org/10.1038/nature11703`.

[47] H. Noda and N. Lapusta. “Three-dimensional earthquake sequence simulations with evolving temperature and pore pressure due to shear heating: Effect of heterogeneous hydraulic diffusivity.” In: *Journal of Geophysical Research: Solid Earth* 115.B12 (2010). DOI: `https://doi.org/10.1029/2010JB007780`.

[48] B. Proctor et al. “Direct evidence for fluid pressure, dilatancy, and compaction affecting slip in isolated faults.” In: *Geophysical Research Letters* 47.16 (2020), e2019GL086767. DOI: `10.1029/2019GL086767`.

[49] C. Raleigh, J. Healy, and J. Bredehoeft. “An experiment in earthquake control at Rangely, Colorado.” In: *Science* 191.4233 (1976), pp. 1230–1237. DOI: `10.1126/science.191.4233.1230`.

[50] J. R. Rice and Y. Ben-Zion. “Slip complexity in earthquake fault models.” In: *Proceedings of the National Academy of Sciences* 93.9 (1996), pp. 3811–3818. ISSN: 0027-8424. DOI: `10.1073/pnas.93.9.3811`.

[51] J. R. Rice and M. P. Cleary. “Some basic stress diffusion solutions for fluid-saturated elastic porous media with compressible constituents.” In: *Reviews of Geophysics* 14.2 (1976), pp. 227–241. DOI: `10.1029/RG014i002p00227`.

[52] J. R. Rice. “Heating and weakening of faults during earthquake slip.” In: *Journal of Geophysical Research: Solid Earth* 111.B5 (2006). DOI: `10.1029/2005JB004006`.

[53] J. W. Rudnicki and D. A. Koutsibelas. “Steady propagation of plane strain shear cracks on an impermeable plane in an elastic diffusive solid.” In: *Int. J. Solids Struct.* 27.2 (1991), pp. 205–225.

[54] J. W. Rudnicki and J. R. Rice. “Effective normal stress alteration due to pore pressure changes induced by dynamic slip propagation on a plane between dissimilar materials.” In: *Journal of Geophysical Research: Solid Earth* 111.B10 (2006). DOI: `10.1029/2006JB004396`.

[55] J. W. Rudnicki and C.-H. Chen. “Stabilization of rapid frictional slip on a weakening fault by dilatant hardening.” In: *Journal of Geophysical Research: Solid Earth* 93.B5 (1988), pp. 4745–4757. DOI: `10.1029/JB093iB05p04745`.

[56] A. Ruina. “Slip instability and state variable friction laws.” In: *Journal of Geophysical Research: Solid Earth* 88.B12 (1983), pp. 10359–10370. DOI: `10.1029/JB088iB12p10359`.

[57] A. Sáez et al. “Three-dimensional fluid-driven stable frictional ruptures.” In: *Journal of the Mechanics and Physics of Solids* 160 (2022), p. 104754. ISSN: 0022-5096. DOI: `https://doi.org/10.1016/j.jmps.2021.104754`.

[58] P. Segall and S. Lu. “Injection-induced seismicity: Poroelastic and earthquake nucleation effects.” In: *Journal of Geophysical Research: Solid Earth* 120.7 (2015), pp. 5082–5103.

[59] P. Segall. *Earthquake and volcano deformation.* Princeton University Press, 2010.

[60] P. Segall and J. R. Rice. “Dilatancy, compaction, and slip instability of a fluid-infiltrated fault.” In: *Journal of Geophysical Research: Solid Earth* 100.B11 (1995), pp. 22155–22171. DOI: `10.1029/95JB02403`.

[61] P. Segall and J. R. Rice. “Does shear heating of pore fluid contribute to earthquake nucleation?.” In: *Journal of Geophysical Research: Solid Earth* 111.B9 (2006). DOI: `https://doi.org/10.1029/2005JB004129`.

[62] P. Segall et al. “Dilatant strengthening as a mechanism for slow slip events.” In: *Journal of Geophysical Research: Solid Earth* 115.B12 (2010).

[63] B. Shibazaki and T. Shimamoto. “Modelling of short-interval silent slip events in deeper subduction interfaces considering the frictional properties at the unstable—stable transition regime”. In: *Geophysical Journal International* 171.1 (Oct. 2007), pp. 191–205. ISSN: 0956-540X. DOI: `10.1111/j.1365-246X.2007.03434.x`.

[64] Y. Song and J. W. Rudnicki. “Plane-Strain shear dislocation on a leaky plane in a poroelastic solid.” In: *Journal of Applied Mechanics* 84.2 (2017), p. 021008.

[65] X. Tong and L. L. Lavier. “Simulation of slip transients and earthquakes in finite thickness shear zones with a plastic formulation.” In: *Nature communications* 9.1 (2018), pp. 1–8. DOI: `https://doi.org/10.1038/s41467-018-06390-z`.

[66] K. Torberntsson et al. “A finite difference method for earthquake sequences in poroelastic solids”. In: *Computational Geosciences* 22.5 (July 2018), pp. 1351–1370. ISSN: 1573-1499. DOI: `10.1007/s10596-018-9757-1`.

[67] A. Verruijt. “Displacement functions in the theory of consolidation or in thermoelasticity.” In: *Zeitschrift für angewandte Mathematik und Physik ZAMP* 22.5 (1971), pp. 891–898.

[68] R. C. Viesca. “Self-similar fault slip in response to fluid injection.” In: *Journal of Fluid Mechanics* 928 (2021), A29. DOI: `10.1017/jfm.2021.825`.

[69] R. C. Viesca and P. Dublanchet. “The slow slip of viscous faults.” In: *Journal of Geophysical Research: Solid Earth* 124.5 (2019), pp. 4959–4983. DOI: `https://doi.org/10.1029/2018JB016294`.

[70] C. A. Wibberley and T. Shimamoto. “Internal structure and permeability of major strike-slip fault zones: the median tectonic line in Mie prefecture, southwest Japan.” In: *Journal of Structural Geology* 25.1 (2003), pp. 59–78.

[71] N. Wynants-Morel et al. “Stress perturbation from aseismic slip drives the seismic front during fluid injection in a permeable Fault.” In: *Journal of Geophysical Research: Solid Earth* 125.7 (2020), e2019JB019179. DOI: `https://doi.org/10.1029/2019JB019179`.

[72] Y. Yang and E. M. Dunham. “Effect of porosity and permeability evolution on injection-induced aseismic slip.” In: *Journal of Geophysical Research: Solid Earth* 126.7 (2021), e2020JB021258. DOI: `https://doi.org/10.1029/2020JB021258`.

[73] A. Yehya, Z. Yang, and J. R. Rice. “Effect of fault architecture and permeability evolution on response to fluid injection.” In: *Journal of Geophysical Research: Solid Earth* 123.11 (2018), pp. 9982–9997. DOI: `https://doi.org/10.1029/2018JB016550`.

[74] S. Zhang, T. E. Tullis, and V. J. Scruggs. “Permeability anisotropy and pressure dependency of permeability in experimentally sheared gouge materials.” In: *Journal of Structural Geology* 21.7 (1999), pp. 795–806. ISSN: 0191-8141. DOI: `https://doi.org/10.1016/S0191-8141(99)00080-2`.

Chapter 3

STABILITY OF FRICTIONAL FAULT SLIP UNDER FLUID INJECTION: COUPLED EFFECTS OF FAULT HEALING, POROELASTICITY AND INJECTION RATE

3.1 Introduction

Here, we use and further develop the approach of Chapter 2 to allow for purely elastic, permeable bulk with the same fluid transport mechanisms and properties. Building on several examples in Chapter 2, we conduct more systematic parametric studies on the effects of fault healing, poroelasticity and injection profile on the stability of fault slip. Understanding the significance of fault healing on stability of slip is crucial to avoiding large destructive earthquakes during industrial activities such as underground fluid injection. Though in Chapter 2 we have done some investigations into the effect of poroelasticity in the bulk, a more direct comparison with elastic bulk would further confirm the stability effects of poroelastic bulk. Besides, it is important to understand the effects of injection rates on the stability of fault slip. In the future, one can potentially optimize the injection rate vs. time profile, to achieve maximum injection flux with optimal fault stability.

3.2 Methodology

The equations and numerical approach that we use are described in Chapter 2. Here, we provide some additional comments relevant to our study. The governing equations for the poroelastic solid bulk are given by (2.1-2.2), repeated here for convenience:

$$Gu_{i,kk} + \frac{G}{1-2\nu}u_{k,ki} = \alpha p_{,i} \tag{3.1}$$

$$\frac{1}{M}p_{,t} - \kappa p_{,kk} = -\alpha u_{k,kt}, \tag{3.2}$$

where G and ν are elastic shear modulus and Poisson's ratio in drained condition. M and α are poroelastic Biot modulus and Biot coefficient, respectively. κ is the mobility of fluid in porous medium. The apparent fluid diffusivity from (3.2) is $c = M\kappa$. However, since u on the right hand side of (3.2) is coupled with p, the apparent c does not directly reflect the diffusion of fluid content. Through a change of variable, the actual fluid diffusion for the fluid mass content ζ is given by [7]

$$\zeta_{,t} - c_{mass}\zeta_{,kk} = 0, \tag{3.3}$$

where c_{mass} is given by

$$c_{mass} = c\frac{K_d + \frac{4}{3}G}{K_u + \frac{4}{3}G}. \tag{3.4}$$

In (3.4), K_d and K_u are drained and undrained bulk modulus, respectively.

In this study, we also consider elastic but permeable bulk, to understand the importance of poroelastic effects in comparison with an elastic problem supplemented with bulk fluid diffusion. The governing equations for elastic permeable bulk are

$$Gu_{i,kk} + \frac{G}{1-2\nu}u_{k,ki} = 0 \tag{3.5}$$

$$p_{,t} - cp_{,kk} = 0, \tag{3.6}$$

where c is the bulk diffusivity associated with the elastic permeable bulk. Note that for elastic permeable solid, since (3.6) is independent of u, the apparent diffusivity coincides with the mass diffusivity, i.e., $c_{mass} = c$. The numerical approach developed in Chapter 2 could not be directly applied to elastic bulk because directly setting $\nu_u = \nu$ will cause numerical problems in the poroelastic kernels, due to dividing by 0.

To allow for simulations with elastic bulk, we first verify the existence and then take the analytical limit of $\nu_u \longrightarrow \nu$ for each poroelastic kernel, and get the corresponding elastic kernel for the spectral boundary integral method. The permeability, diffusivity of the bulk material, as well as the continuity condition of fluid flux from the shear layer into the bulk are kept unchanged from the poroelastic case.

We aim to study the effect of injection rate and injection-time profile. Since the total injected volume has been proposed as one of the important controls (Ref), we switch from the pore-pressure controlled injection studied in Chapter 2 to a baseline case with the total mass of injected fluid controlled. Motivated by the pressure-controlled injection in Chapter 2, we take the corresponding averaged flux over the experimental window (1400 s), and use that as our baseline flux. Figure 3.1 shows the comparison between the evolution of pore fluid pressure and slip rate over the fault under pressure-control injection and flux-control injection with the same average flux. The material properties which are kept the same in both cases can be found in Table B.1 and B.2. We find that the flux-control injection case has qualitatively similar response compared with the pressure-control injection, while the pore fluid pressures p^+, p^- and p_c increase faster with time upon the start of the injection. In the following discussion, we refer to the flux-control case with baseline flux 1×10^{-4} Kg/(m · s) as the baseline case.

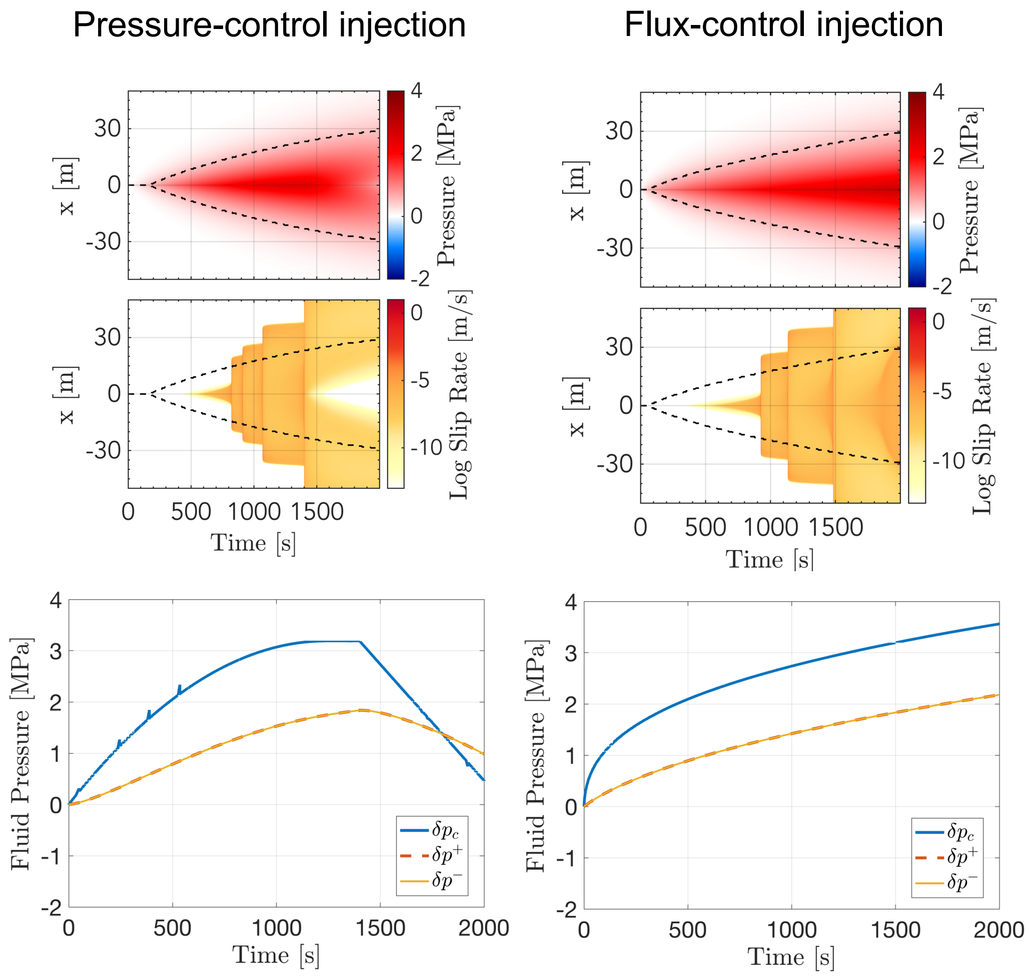

Figure 3.1: Comparison of slip rate and pore pressure evolution under pressure-control injection (left column) and flux-control injection (right column) with baseline flux $c_{base} = 10^{-4}$ Kg/(m · s). The evolution of pore pressure (top row) and fault slip rate (middle row) as functions of time and distance along the fault indicates that both cases result in qualitative similar behavior. The dashed lines indicate the profile of $\delta p_m = 0.5$ MPa. The near-vertical extension of slip rates indicate dynamic events. The time history of changes in fluid pressure in the middle of the shear layer (δp_c) and on its top and bottom edge (δp^+ and δp^-) are shown in the bottom row. For our baseline case, the flux is set to be the average flux from the pressure-controlled injection case of Chapter 2.

3.3 Results and discussion

In this section, we present and discuss results that reveal the effect of fault healing, poroelastic coupling between the volumetric deformation and pore fluid pressure, injection rate and more generally injection-time profile on frictional fault slip under fluid injection.

Significant effect of fault healing on the stability of fault slip

It is clear that fault stress plays an important role in fault slip due to fluid injection, an effect well-studied in prior simulations, mostly with the slip-weakening friction [10, 2, 1]. In the commonly used slip-weakening formulation, there is no slip until $\tau/(\sigma - p)$ reaches the peak (also often called "static") friction coefficient. The closer the stress conditions are to failure in such models, the easier it is for the fault to slip in response to fluid injection of the same properties.

In the rate-and-state formulations, peak friction is a function of the history of fault slip. In particular, a more healed fault with a larger value of θ at the initiation of fluid injection, which should result in a larger peak friction during sliding, should behave in a more stable manner, for the same initial conditions of $\tau/(\sigma - p)$.

Let us study the importance of this effect in our model. A larger value of θ for the same $\tau/(\sigma - p)$ results in a lower initial slip rate V_{ini}. Let us consider the evolution of fault slip and friction for $V_{ini} = 0.45 \times \{10^{-22}, 10^{-19}, 10^{-16}, 10^{-13}\}$ m/s under our base-case flux-controlled injection with a flux of 10^{-4} Kg/(m $\cdot$ s) constant in time. The other model properties are listed in Table B.1 and B.2. The initial slip rate of 10^{-22} m/s corresponds to the base case shown in Figure 3.1. Note that these initial slip rates correspond to the initial values of the state variable given by $2.38 \times 10^{12}, 1.85 \times 10^{10}, 1.44 \times 10^{8}, 1.12 \times 10^{6}$ s or $75469, 586, 4.56, 0.0355$ years, which, for the aging formulation we use in this work, give the approximate healing time. Here we parameterize the healing through the decreased initial slip rate because this is the measurable consequence of healing, as demonstrated by recent laboratory experiments on PMMA interfaces (Sirorattanakul et al., 2024, [9]).

We find that for less-healed faults with higher initial slip rate V_{ini}, the first dynamic event happens earlier in time and dynamic events occur more frequently (Figure 3.2). Furthermore, the events sooner expand farther into the fault (along the x direction in the Figure). For a more quantitative look, let us compare the evolution of the slip rate and friction coefficient the at the center of the fault, $x = 0$ (Figure 3.3a, b). As expected, the peak friction is substantially higher for the more healed faults with the smaller V_{ini}, ranging from more than 0.9 to 0.7. We emphasize that these values are reached for the same rate-and-state friction properties, including the reference friction coefficient of 0.55, with the only difference being prior slip history of the fault (not modeled here but assumed through the initial value of slip rate). Consistently with higher friction, more healed faults reach significant slow slip rates and produce dynamic events later in the injection history.

These behaviors can be quantitatively understood by the following considerations (Larochelle et al., 2021 [5]): At the beginning of the fluid injection, slip rates are low and both inertial effects and elastic stress transfers are negligible, which means that the shear stress remains nearly unchanged, i.e.,

$$f(V,\theta)\,(\sigma - p_m(x,t)) = \tau_{ini}. \tag{3.7}$$

As p increases from the injection, f has to increase through increasing V for (3.7) to hold, resulting in a balance between the direct frictional effect and changes in pore pressure. f and p continue to increase until V reaches its significant value $V_s \sim 10^{-7}$ m/s. Once V reaches V_s, within a relevant time scale of 10 s, the local slip is on the order of 1 μm, which is of the same order as our $D_{RS} = 16.75$ μm. With this consideration, one can reason that significant slip has occurred once V reaches V_s. According to the evolution law (2.20) of the state variable θ, the significant slip would allow for the decrease of state variable and hence weakening of friction. Therefore, the onset of this significant slip approximately coincides with when f reaches its peak value f_p. f_p can be approximately calculated by

$$f_p = f_* + a\log\left(\frac{V_s}{V_*}\right) + b\log\left(\frac{V_*\theta_{ini}}{D_{RS}}\right). \tag{3.8}$$

θ_{ini} is used here in (3.8) because it has not evolved significantly yet due to negligible slip and short healing time compared to its large initial value. Moreover, from (3.7) we can also approximate f_p through

$$f_p = \frac{\tau_{ini}}{\sigma - p_m(0,t_s)}, \tag{3.9}$$

assuming σ has not changed significantly because of negligible slip and thus negligible poroelastic effects.

Note that these considerations do not predict whether the resulting significant slip post-peak that results in weakening would be seismic or aseismic. For the parameters studied in Larochelle et al., 2021 [6], the induced slip was aseismic throughout the weakening. In our case, the slip rate at peak friction is of the order 10^{-7} m/s, and the peak slip rate of $10^{-3} \sim 10^{-1}$ m/s is reached further along the weakening curve, as shown by Figure 3.3 (a-b, e) and 3.4 (a-b). Figure 3.3 (c) and Figure 3.4 (c) further confirm that the state variable θ has not evolved significantly when friction reaches its peak and significant slip has just happened. After the onset of significant slip, θ starts evolving significantly from θ_{ini}, and later V reaches its peak of $10^{-3} \sim 10^{-1}$ m/s in all four cases.

One consideration that may explain the instability happening in cases shown in Figure 3.2 is through the comparison between local nucleation size and local slip zone. Through linear stability analysis with rate-and-state friction, previous studies [8, 4] have shown that the critical length for nucleation of dynamic events is given by

$$L_{nu}(x) = \frac{G D_{RS}}{(b-a)(\sigma - p_m)(1-\nu)}. \tag{3.10}$$

Take the first case in Figure 3.2 which has $V_{ini} \sim 10^{-22}$ m/s as an example, the first dynamic event happens around $t = 923$ s, as shown by Figure 3.5(a). We define the total slip zone to be the portion along the fault such that $\dot{\theta} = 1 - V\theta/D_{RS} \leq 0$, which gives us a closed interval $[x_{B1}, x_{B2}]$ as shown by Figure 3.5(b). Let us further define the local slip zone at x $L_{slip}(x)$ to be twice the distance between x and the closer boundary of the total slip zone, i.e.,

$$L_{slip}(x) = \min_{i \in \{1,2\}} 2|x - x_{Bi}|. \tag{3.11}$$

For a dynamic event to nucleate at x, linear stability analysis requires that the local slip zone $L_{slip}(x)$ needs to be larger than the critical nucleation size $L_{nu}(x)$. Figure 3.5(c) confirms that before the nucleation of the first dynamic event at $t = 920$ s, everywhere along the fault $L_{slip} < L_{nu}$ while only at $x = 0$ L_{slip} is approaching and exceeding L_{nu}. Then a dynamic event nucleates at $x = 0$ and we have a region along the fault that satisfies $L_{slip} > L_{nu}$ at $t = 926$ s. This result confirms that it is necessary to have the local slip zone exceeding the local nucleation size for the nucleation of a dynamic event. In summary, we find that within the typical notion of "close to zero" initial slip rate, the stability of fault slip under fluid injection depends significantly on the initial slip rate, and that less healed faults tend to have earlier, more frequent dynamic events that expand farther in space.

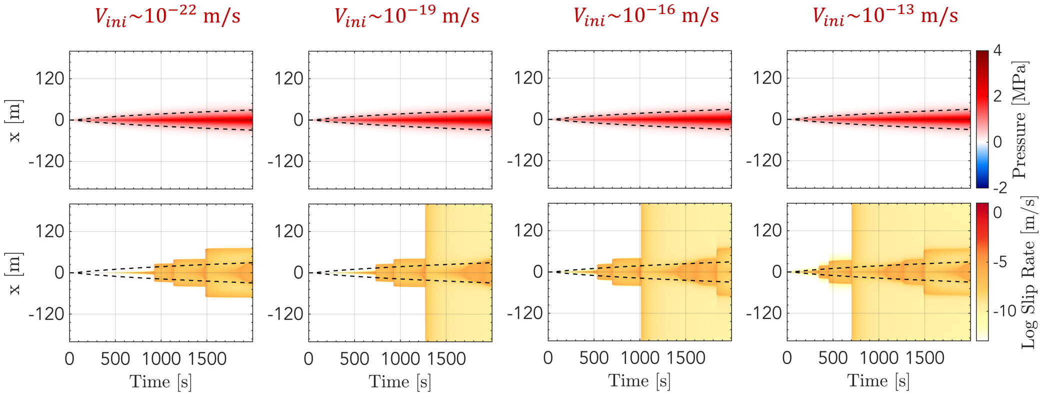

Figure 3.2: More healed faults with lower initial slip rate tend to be more stable under the same flux-controlled injection. Comparison of average pore pressure change δp_m (upper row) and slip rate (lower row) vs. time along the fault for $V_{ini} \approx 10^{-22}, 10^{-19}, 10^{-16}, 10^{-13}$ m/s. The pressure evolution is similar due to the same flux-controlled injection process, while the onset of slow slip (yellow color and the first dynamic event (nearly vertically spreading slip regions) occurs earlier for larger V_{ini}. The spatial extent of the dynamic events also becomes larger earlier for larger V_{ini}.

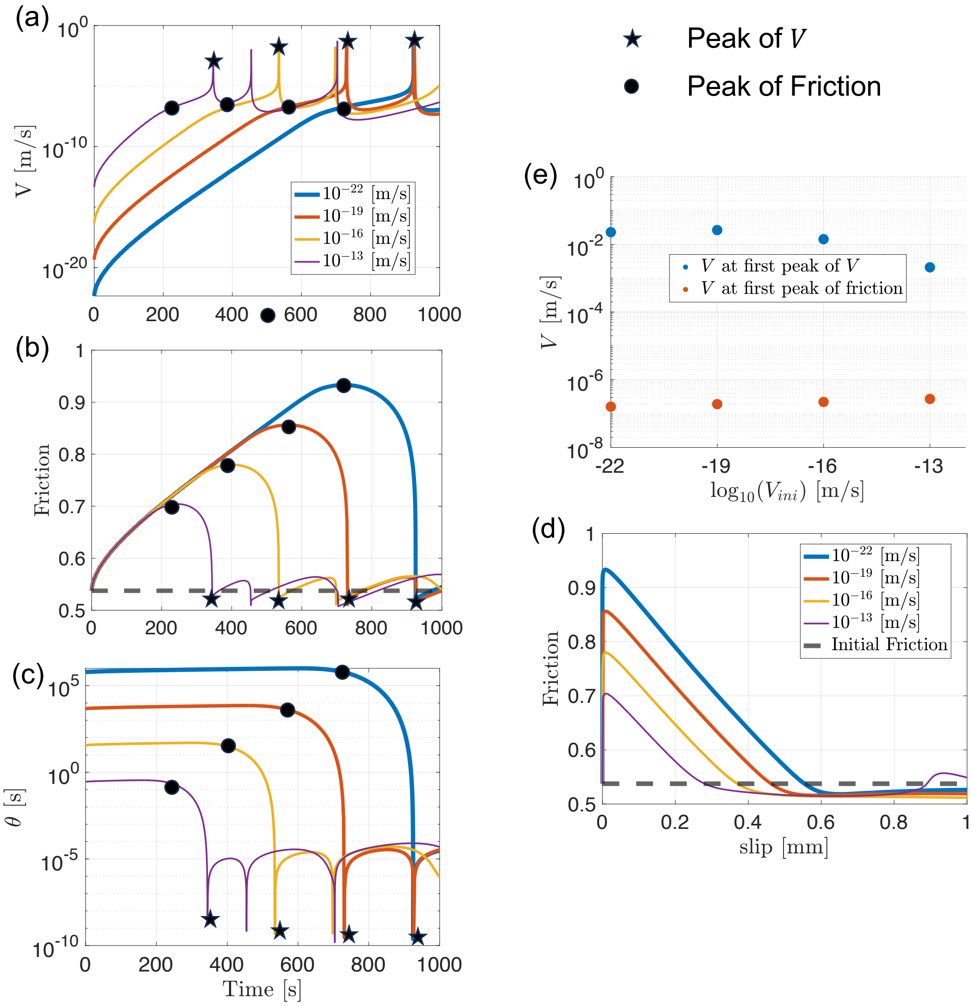

Figure 3.3: (a, b, c) Slip rate vs. time, friction vs. time, *theta* vs. time at $x = 0$ m for the 4 cases. The stars and circles mark the peaks of slip rate V and friction in each case. The friction peak arrives earlier than the peak in slip rate V, after which the evolution of θ becomes significant. (d) Friction vs. slip at $x = 0$ m for the 4 cases. (e) Slip rate V at the first peak of V and at the first peak of friction. The peak slip rate decreases as V_{ini} increases, and is of the order $10^{-3} \sim 10^{-1}$ m/s. The slip rate V at which the friction peaks is of the order 10^{-7} m/s, close to the V after which the state variable θ starts evolving significantly.

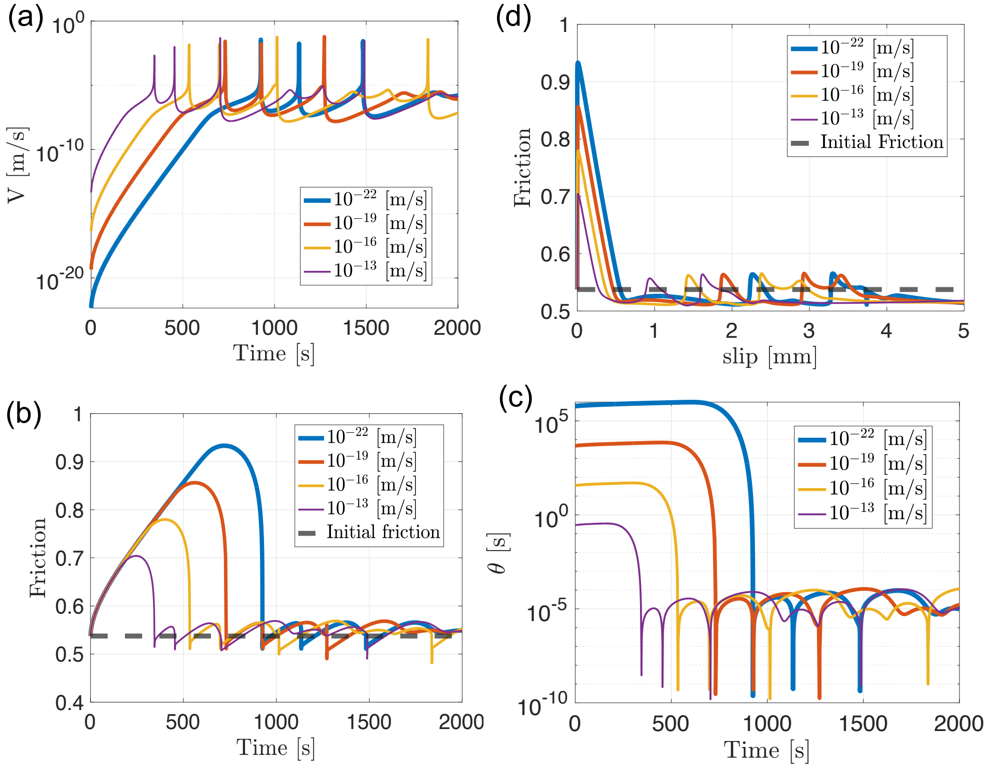

Figure 3.4: Full time plots of slip rate, friction and state variable θ vs. time and friction vs. slip over longer distances. (a, b, c) Slip rate vs. time, friction vs. time, θ vs. time at $x = 0$ m for the 4 cases. (d) Friction vs. slip at $x = 0$ m for the 4 cases. Note that in all cases, friction reduces to a value that is smaller than the initial friction.

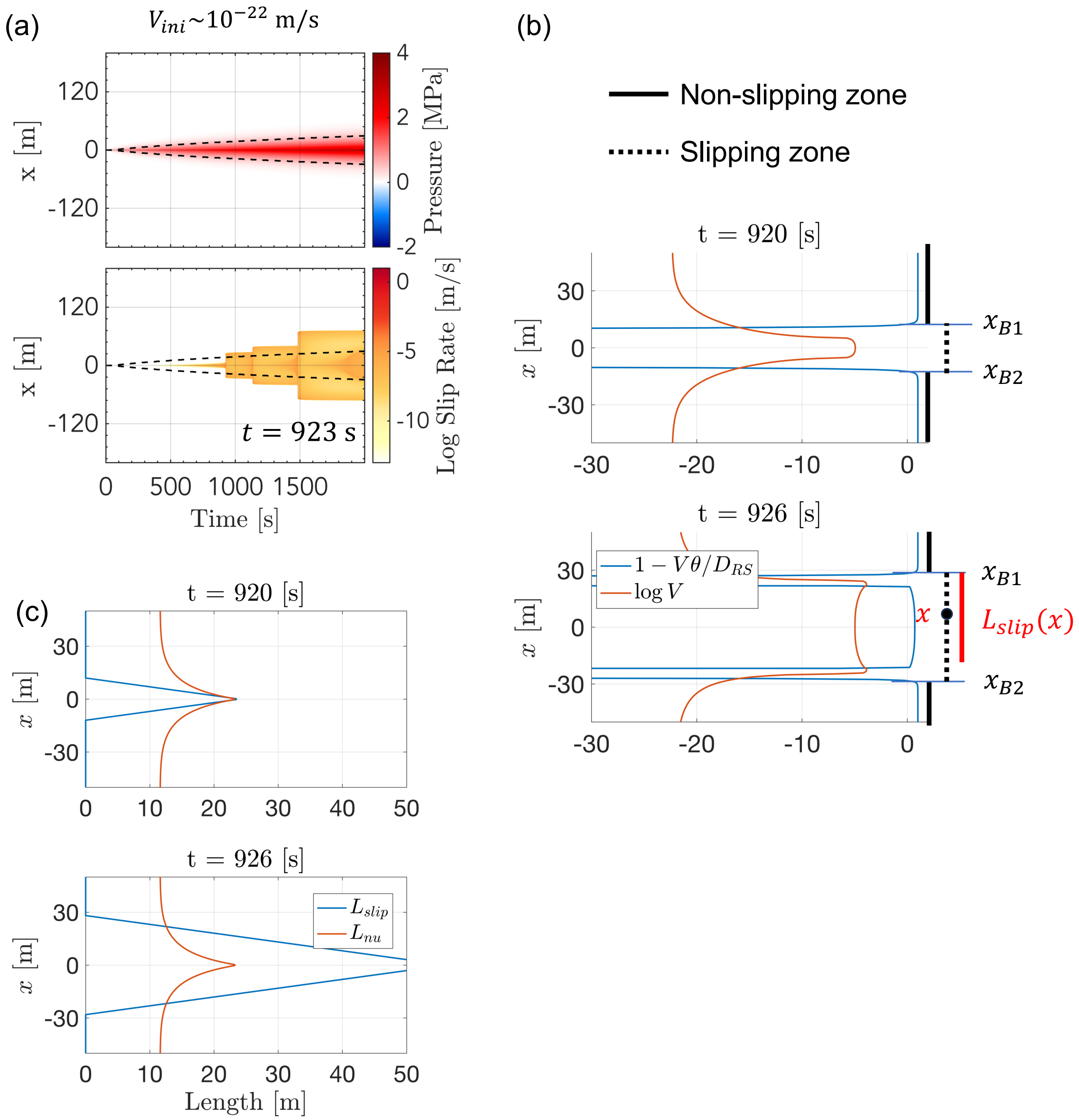

Figure 3.5: Dynamic fault slip can nucleate when slip zone exceeds the local nucleation size. (a) Average pore pressure change and slip rate vs. time along the fault for V_{ini} 10^{-22} m/s with poroelastic bulk. Note that the first dynamic event happens around $t = 923$ s. (b) $\log(V)$ and $\dot{\theta} = 1 - V\theta/D_{RS}$ along the fault at $t = 920, 926$ s. We define the total slip zone to be the region where $\dot{\theta} < 0$, and the local slip zone at x, $L_{slip}(x)$ to be twice the distance between x and the closer boundary of the total slip zone. (c) A comparison between $L_{slip}(x)$ and $L_{nu}(x)$ as defined by (3.10). Before the nucleation of a dynamic event at $t = 920$ s, everywhere along the fault $L_{slip} < L_{nu}$ while only at $x = 0$ L_{slip} is approaching and exceeding L_{nu}. Then a dynamic event nucleates at $x = 0$ and we have a region along the fault that satisfies $L_{slip} > L_{nu}$ at $t = 926$ s.

Effects of poroelasticity

The work of Heimisson et al.(2022) [3] has shown that fault slip becomes more unstable as the undrained Poisson's ratio ν_u decreases and gets closer to drained Poisson's ratio ν, under the same fluid injection. And thus it was inferred that poroelasticicty stabilizes fault slip under fluid injection. However, due to the limitations in the code, that work was not able to achieve the elastic limit, i.e., $\nu_u = \nu$. Here, we implement the elastic kernels such that we can indeed simulate cases with $\nu_u = \nu$, which equivalently sets $\alpha = 0$, and results in the poroelastic equations reduced to elastic equations as given by (3.5, 3.6). To compare elastic and poroelastic cases, the governing equations and material properties of the shear layer are kept the same. The fluid mobility of the bulk κ is kept the same between elastic and poroelastic cases, whereas the fluid diffusivity in the bulk is set to either $c = M\kappa$ or c_{mass} given by (3.4).

Since there are two end-member Poisson's ratios in the poroelastic problem, namely the undrained ν_u and the drained ν, we consider two elastic cases with Poisson's ratio set to ν_u and ν, and compare them to the poroelastic case. The material properties are given in Tables B.1 and B.2.

Let us compare the results of the poroelastic and two elastic cases while keeping the same apparent bulk diffusivity c (Figure 3.6) vs. the same true fluid diffusivity c_{mass} as given by (3.4) (Figure 3.7. We find that, under the same flux-control injection and with the same apparent bulk diffusivity, the poroelastic case is more stable than the elastic, permeable case with $\nu = 0.24$, and is slightly more stable than, but quite similar to, the elastic, permeable bulk with $\nu = 0.35$. This suggests that under such injection and dynamic fault slip condition, the poroelastic bulk is close to being undrained. If the elastic case with the Poisson's ratio $\nu = 0.35$ corresponding to the undrained value of the poroelastic case is additionally modified to have bulk fluid diffusivity incorporate some poroelastic effects through c_{mass}, then the resulting simulation matches the poroelastic one almost exactly (Figure 3.7). Hence one can very closely mimic the poroelastic solution by using elastic, permeable bulk with the c_{mass}, κ, ν_u and G from the poroelastic problem.

The results suggest that the poroelastic effects near a slipping fault are always close to their undrained limit. A simple analysis shows why this would be the case for realistic properties of the bulk and the frictional interface. The region of the modified pore fluid pressure due to the poroelastic effect occurs where there are significant slip gradients that result in transient fault-parallel compression of dilation (Figure 3.8).

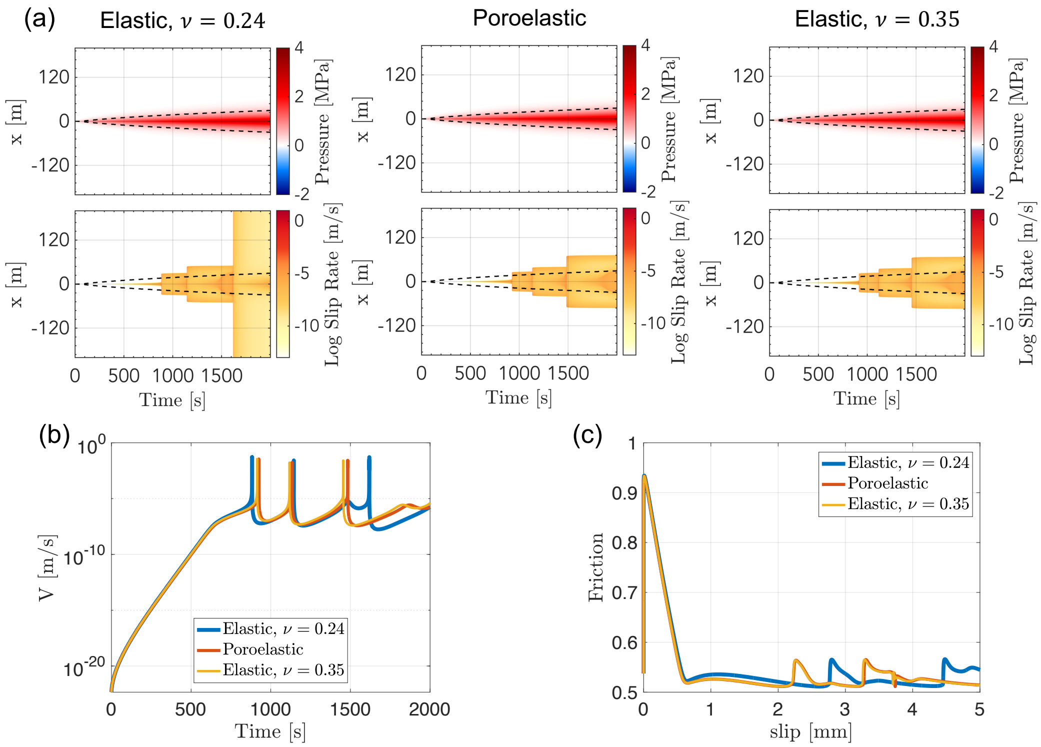

Figure 3.6: Results for elastic permeable vs. fully poroelastic bulk when the apparent bulk diffusivity c is kept unchanged. (a) Comparison of average fluid pore pressure change δp_m (upper row) and slip rate V (lower row) vs. time along the fault for elastic bulk with $\nu = 0.24$ (left column), poroelastic bulk with $\nu = 0.24$, $\nu_u = 0.35$ (middle column), and elastic bulk with $\nu = 0.35$ (right column). (b) Slip rate vs. time at $x = 0$ m for the above 3 cases. (c) Friction vs. slip at $x = 0$ m for the 3 cases. All the three cases develop dynamic events at similar times, with the elastic case with the lower $\nu = 0.24$ being the most unstable, both in terms of earlier onset of seismic slip and in terms of larger spatial extent of seismic events. The case with poroelastic bulk looks similar to the elastic case with the Poisson's ratio $\nu = 0.35$ corresponding to the undrained value.

Let us denote the characteristic length scale of the pressurized region by L_{ch}, as shown in Figure 3.8, which is usually a fraction of the fault length. Denote the propagation speed of the pressure front as V_{pro}, which is usually a fraction of the shear wave speed of the bulk. For any material point adjacent to the fault in the poroelastic bulk, the time it is affected by the pressure front is $t_{ch} = D_{ch}/V_{pro}$, in which time, by 1-D diffusion approximation, the fluid can diffuse a distance approximated by $D_{sp} = \sqrt{t_{ch}c}$ into the bulk. For the poroelastic increases in pore fluid pressure to be affected by the diffusion processes, one needs $D_{sp} \approx D_{ch}$, which

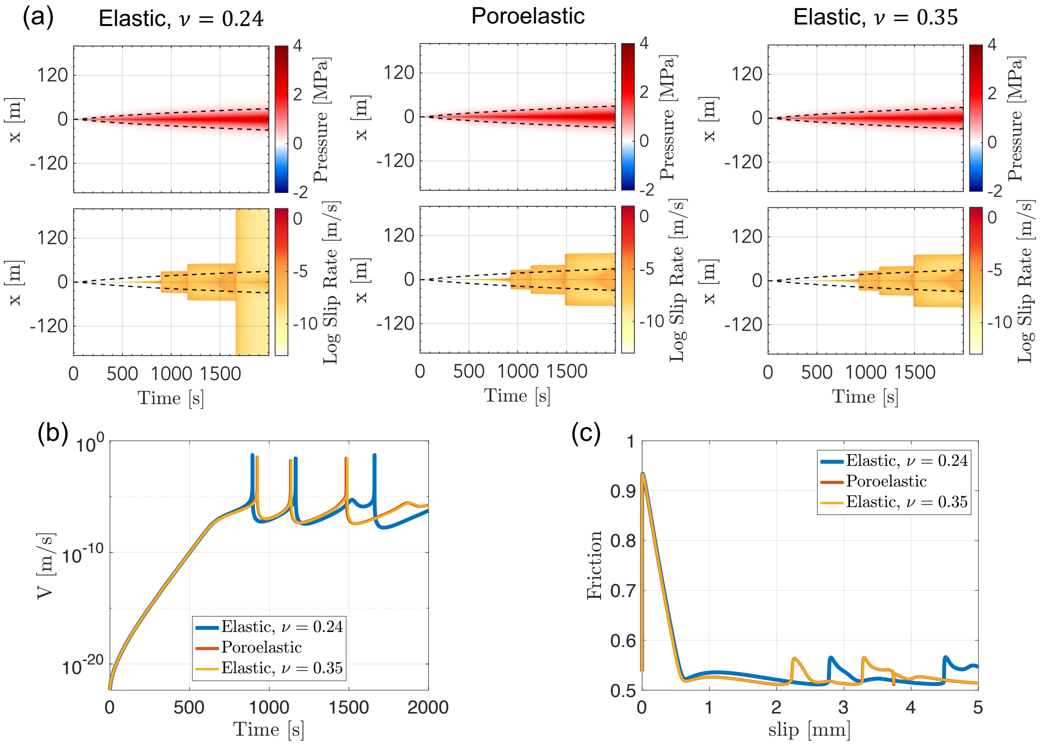

Figure 3.7: Rseults of elastic permeable vs. fully poroelastic bulk when the bulk diffusivity for fluid mass content c_{mass} is kept unchanged. (a) Comparison of average fluid pore pressure change δp_m (upper row) and slip rate V (lower row) vs. time along the fault for elastic bulk with $\nu = 0.24$ (left column), poroelastic bulk with $\nu = 0.24$, $\nu_u = 0.35$ (middle column), and elastic bulk with $\nu = 0.35$ (right column). (b) Slip rate vs. time at $x = 0$ m for the 3 cases. Note that the first dynamic event nucleates slightly earlier in the case with elastic, $\nu = 0.24$ bulk than the other two, but compared with Figure 3.6 (b), the difference is smaller. (c) Friction vs. slip at $x = 0$ m for the 3 cases. When c_{mass} is kept the same, the poroelastic case looks nearly identical to the elastic case with the Poisson's ratio $\nu = 0.35$ corresponding to the undrained value. This indicates that one can account for poroelastic effects by considering the elastic bulk with the fluid diffusivity modified to c_{mass} and Poisson's ratio modified to its undrained value.

requires the hydraulic diffusivity in the bulk to be:

$$\begin{aligned} D_{sp} &= \sqrt{t_{ch} c_{req}} \approx D_{ch} \\ c_{req} &\approx D_{ch} V_{pro}, \end{aligned} \tag{3.12}$$

where c_{req} denotes the required bulk hydraulic diffusivity. If D_{ch} is 1 m or more, and V_{pro} is 1 m/s or more (it is usually much faster for dynamic events), then the required hydraulic diffusivity would be more than 1 m^2/s, which is already higher than typical hydraulic diffusivities for rocks, even under low comfining pressure. In the case of our simulation shown in Figure 3.8, $D_{ch} \approx 6$ m and $V_{pro} \approx 100$ m/s, in which case the required bulk diffusivity has to be ≈ 600 m^2/s to singificantly affect the poroelastic pore pressure increases, a clearly unphysical value. In our simulation, the hydraulic diffusivity is given by 10^{-8} m^2/s.

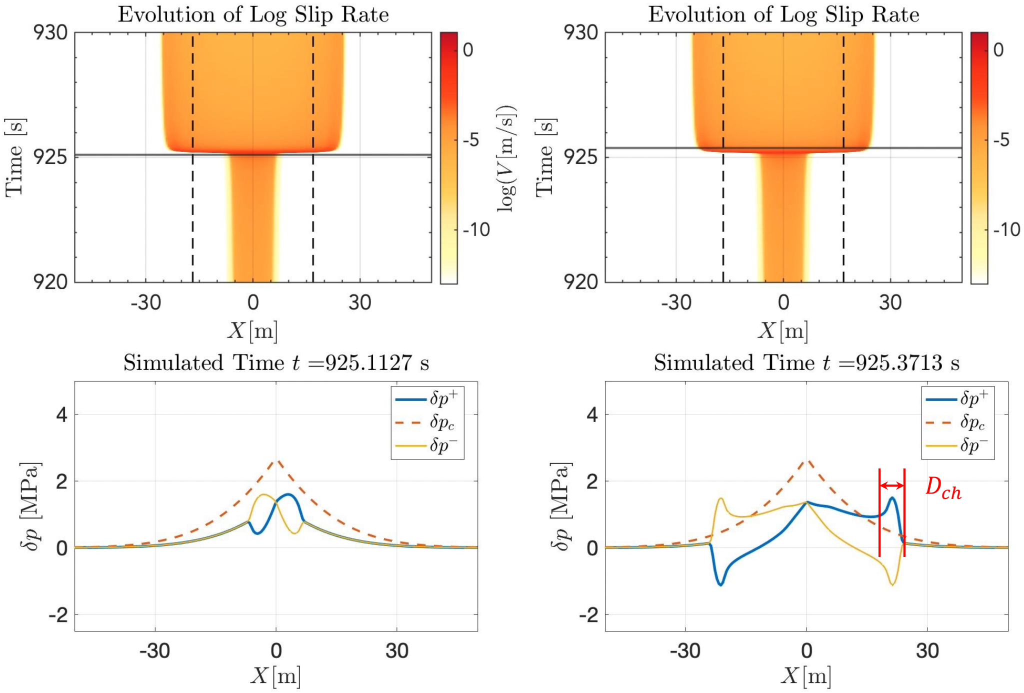

Figure 3.8: The propagation of pore pressure changes due to poroelastic effect during the first dynamic event. (Upper row, left) Evolution of log slip rate along the fault, where the dashed line marks the pressure profile of $\delta p_m = 0.5$ MPa, and the solid line indicates the current plotting time. (Lower row) Pore pressure changes above the shear layer δp^+, in the middle of the shear layer δp_c, and below the shear layer δp^-, at two times during the dynamic event. Note that the difference between δp^+ and δp^- is a poroelastic effect. Within 0.26 s, the pressure front propagates 25 m. The characteristic length scale of the perturbed pressure front is $D_{ch} \approx 6$ m, and the propagation speed of the perturbed pressure feature is $V_{pro} \approx 100$ m/s.

Effects of injection rate and intermittancy

Let us consider how the injection flux affects the stability of fault slip, for a fixed mass of injected fluid. We first change the injection rate (flux) while keeping the flux constant in time. Figure 3.9 shows the comparison of slip rate vs. time along x for an injection at baseline flux, 0.75 of the baseline flux and 0.5 of the baseline flux; note that the injection time changes with the injection flux to result in the same injected fluid mass. The surrounding bulk is poroelastic with properties listed in table B.1. The fault properties are listed in table B.2. We find that a larger injection rate leads to earlier, more frequent dynamic events but with smaller spatial extent. In particular, with the smallest injection rate at 0.5 baseline flux, the dynamic event happens later but expands across the entire simulated fault, while the first dynamic events of cases with higher injection rates are self-contained, i.e., arrest within the simulated fault. The dynamic slip rates are similar for all injection rates once a dynamic event happens (Figure 3.9b) and the friction peak is similar among all three cases because they start from the same initial slip rate and hence the same level of fault healing (Figure 3.9c).

The results are qualitatively similar for elastic, permeable bulk (Figures 3.11 and 3.12). which confirms that for a given total injected mass of fluid, larger injection rate would lead to more frequent but spatially more constrained dynamic slip events. This is because slower injection rates lead to pore fluid pressure diffusing further along the fault (Figure 3.10), both reducing the peak pore fluid pressure and hence slowing down slip at the injection site as well as bringing more of the fault closer to rapid slip, which allows events to grow larger once they nucleate.

Inspired by the fact that a faster injection rate results in smaller events first and hence delays the occurrence of a spatially wide-spread dynamic event, we investigate the effect of intermittent injection rate, while keeping the average injection rate and total amount of injected fluid mass the same (Figure 3.13a). The intermittent injection profile results in earlier and more frequent dynamic events, but they are spatially confined, whereas the constant injection rate results in a later model-spanning event (Figure 3.13b). Figure 3.13 (d) further confirms that the intermittent injection results in smaller total slip. This result suggests that it may be possible to optimize the injection rate-time profile, to achieve more spatially-restricted, smaller dynamic slip events, with a given average injection flux as the constraint.

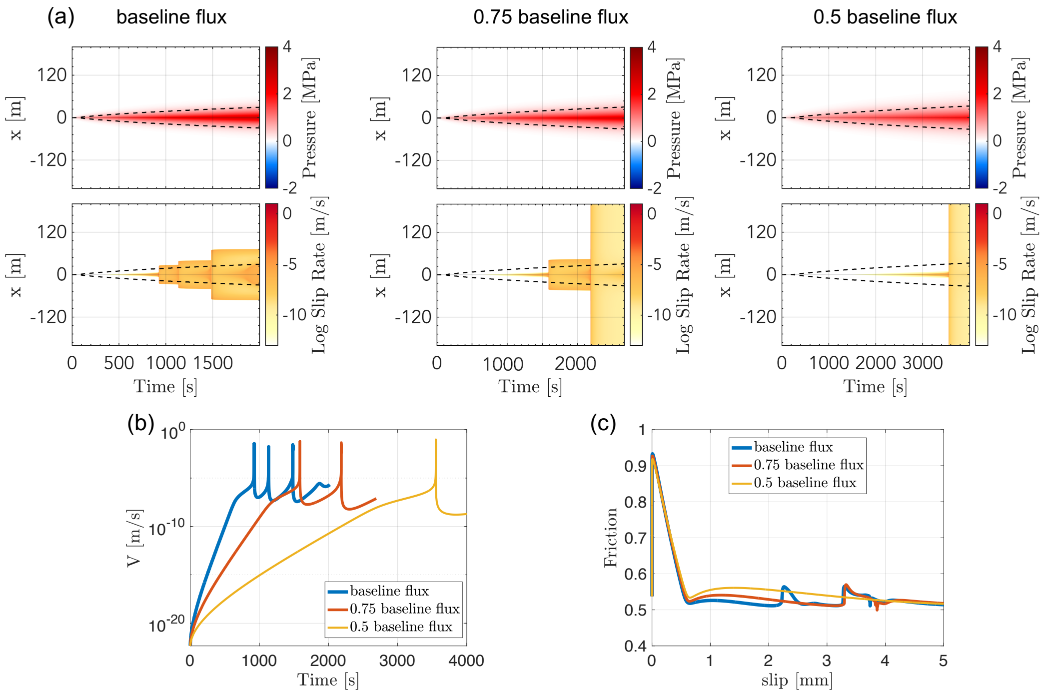

Figure 3.9: The effect of injection rate (flux) on stability of fault slip surrounded by poroelastic bulk. The total injected mass is kept the same for all cases, and thus time is adjusted for different injection rates. Baseline flux is set to be $c_{base} = 1.0 \times 10^{-4}$ Kg/(m · s). (a) Average pore pressure change δp_m (upper row) and slip rate (lower row) vs. time along x for baseline flux (left column), 0.75 baseline flux (middle column) and 0.5 baseline flux (right column). We see that as the flux (injection rate) decreases, the onset of dynamic events gets delayed more than would be expected just based on the ratio of the fluxes, and the spatial extent of the dynamic events becomes larger. (b) Slip rate vs. time at $x = 0$ m for the 3 cases. (c) Friction vs. slip at $x = 0$ m for the 3 cases.

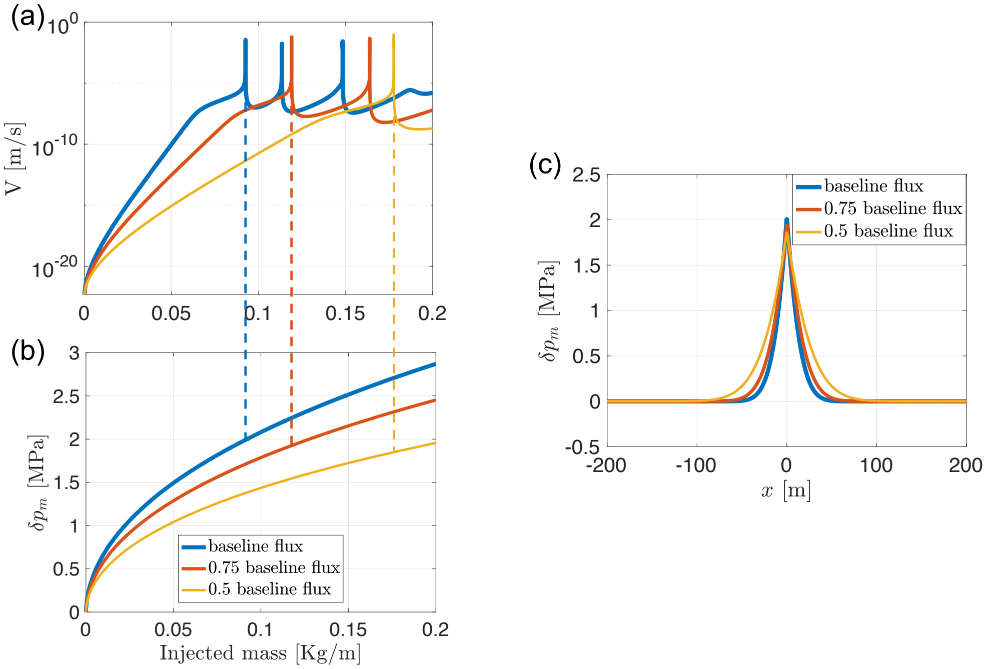

Figure 3.10: The effect of injection rate on stability of fault slip surrounded by poroelastic bulk. (a-b) Slip rate and δp_m vs. injected mass at $x = 0$ m, for the three cases in Figure 3.9. The first dynamic event nucleates at a smaller injection mass for larger injection rates. The average pore pressure at the nucleation of the first dynamic event decreases as injection rate decreases. (c) δp_m along the fault right before the first dynamic event, for the 3 cases. Slower injection rates lead to pore pressure diffusing further along the fault, both reducing the peak pore pressure and bring more of the fault closer to rapid slip, which allows events to grow larger once they nucleate.

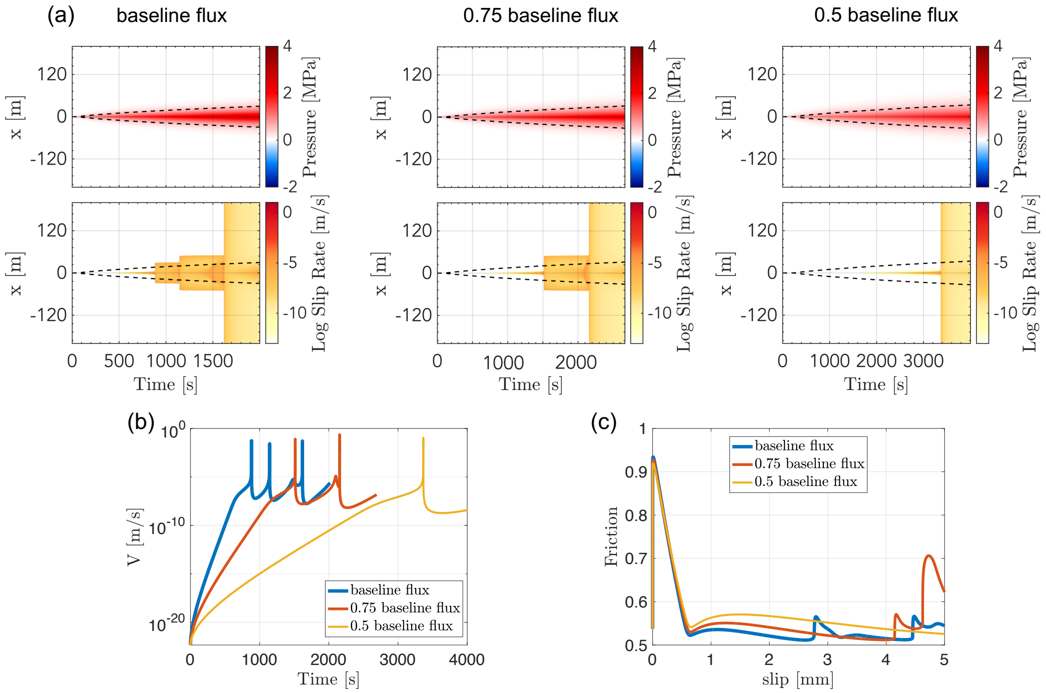

Figure 3.11: The effect of injection rate (flux) on stability of fault slip surrounded by elastic, permeable bulk with $\nu = 0.24$. The total injected mass is kept the same for all cases, and thus time is adjusted for different injection rate. Baseline flux is set to be 1.0×10^{-4} Kg/(m · s). (a) Average pore pressure change δp_m (upper row) and slip rate (lower row) vs. time along x for baseline flux (left column), 0.75 baseline flux (middle column) and 0.5 baseline flux (right column). We see that as the flux (injection rate) decreases, the onset of dynamic events gets more delayed, (b) Slip rate vs. time at $x = 0$ m for the 3 cases. (c) Friction vs. slip at $x = 0$ m for the 3 cases.

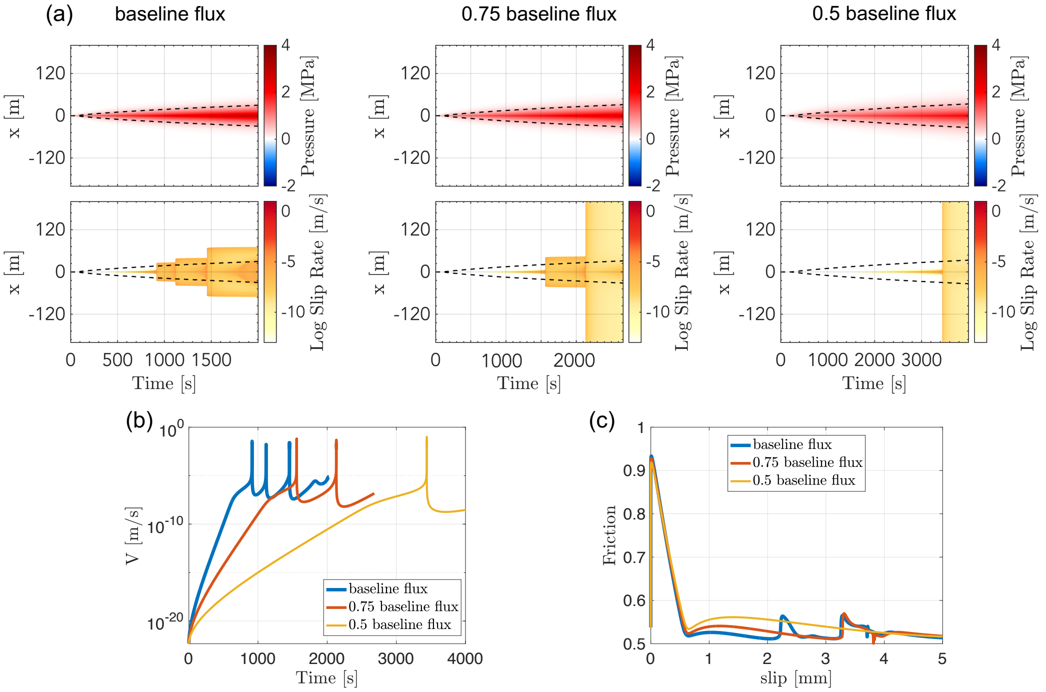

Figure 3.12: The effect of injection rate (flux) on stability of fault slip surrounded by elastic, permeable bulk with $\nu = 0.35$. The total injected mass is kept the same for all cases, and thus time is adjusted for different injection rate. Baseline flux is set to be 1.0×10^{-4} Kg/(m · s). (a) Average pore pressure change δp_m (upper row) and slip rate (lower row) vs. time along x for baseline flux (left column), 0.75 baseline flux (middle column) and 0.5 baseline flux (right column). We see that as the flux (injection rate) decreases, the onset of dynamic events gets more delayed, but the spatial extent of the dynamic events become larger. Besides the case with baseline flux, the other two cases with smaller injection rates both have a dynamic event that spreads across the entire fault. (b) Slip rate vs. time at $x = 0$ m for the 3 cases. (c) Friction vs. slip at $x = 0$ m for the 3 cases.

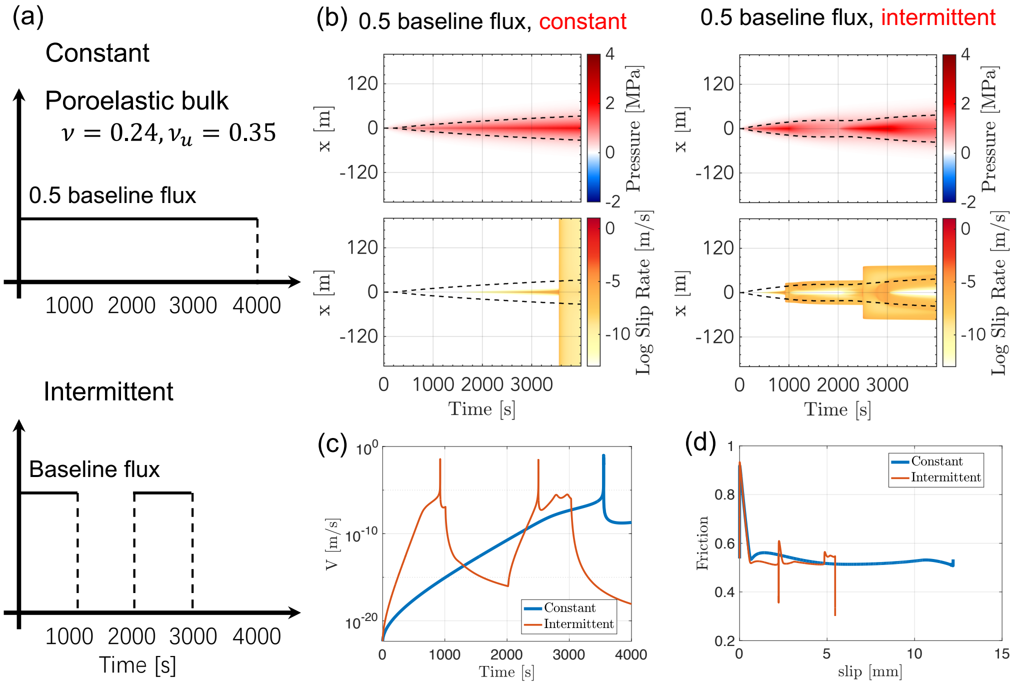

Figure 3.13: Comparison between constant injection rate and intermittent injection rate with poroelastic bulk. (a) Constant (upper) and intermittent (lower) injection rates that we impose as functions of time. (b) Average pore pressure change δp_m (upper row) and slip rate (lower row) vs. time along the fault for constant (left column) and intermittent (right column) injection rate. The average injection rate as well as the total injected mass are kept the same, and thus the simulated time lengths are the same. One can see that the intermittent injection case has earlier and more frequent occurrences of dynamic events, but those dynamic events have much more limited spatial extent. (c) Slip rate vs. time at $x = 0$ m. We see that the dynamic slip rates are similar between the two cases, but once the injection is paused, the slip rate reduces rapidly with time in the intermittent case, potentially contributing to the limited spatial extent of dynamic events. (d) Friction coefficient vs. slip at $x = 0$ m. The small peaks of friction in the intermittent case reflects the healing effect when the injection is paused.

3.4 Conclusions

In this study, we apply and further develop a boundary integral code for simulations of frictional fault slip, with poroelastic surrounding bulk, to study several relevant factors that may affect the stability of fault slip under fluid injection. First, we find that the fault healing, or initial slip rate under rate-and-state friction, affects the stability of fault slip significantly. A change from $V_{ini} = 10^{-22}$ m/s to $V_{ini} = 10^{-13}$ m/s would result in a much earlier nucleation of dynamic events and much larger spatial expansion of them, under the same fluid injection. Second, we further develop the code to allow for purely elastic bulk with the same fluid-transport properties, and confirm that poroelasticity stabilizes fault slip under fluid injection. We also find that with the typical length scales and properties of natural faults as well as injection time scale, poroelastic and elastic bulk with undrained Poisson's ratio have similar effects on dynamic fault slip. This is because the propagation speed of the pore pressure front is much faster than the diffusion speed of the pressure perturbations into the bulk, and thus the bulk s essentially undrained elastic. Finally, we study the effects of injection flux as a function of time on the stability of fault slip. We find that for mass-controlled injection at constant injection rate, higher injection rate leads to earlier and more frequent occurrences of dynamic events. However, these events have smaller spatial extent. Motivated by that, we further change the injection rate from constant to intermittent in time, and find that with the same average injection rate and total injected fluid mass, intermittent injection also leads to earlier, more frequent but more spatially restricted dynamic events. This suggests that with an optimized injection rate-time profile, one can possibly achieve more spatially restricted and less destructive dynamic events at a given average injection rate. In the future, one can formulate an optimization over injection rate-time function, to achieve an objective of more stable, less destructive dynamic fault slip under a given average injection rate.

References

[1] M. Galis et al. "Induced seismicity provides insight into why earthquake ruptures stop." In: *Science Advances* 3.12 (2017), eaap7528. DOI: `10.1126/sciadv.aap7528`.

[2] D. I. Garagash and L. N. Germanovich. "Nucleation and arrest of dynamic slip on a pressurized fault." In: *Journal of Geophysical Research: Solid Earth* 117.B10 (2012). DOI: `https://doi.org/10.1029/2012JB009209`.

[3] E. R. Heimisson et al. “A spectral boundary-integral method for faults and fractures in a poroelastic solid: simulations of a rate-and-state fault with dilatancy, compaction, and fluid injection.” In: *Journal of Geophysical Research: Solid Earth* 127.9 (2022). DOI: `10.1029/2022JB024185`.

[4] N. Lapusta et al. “Elastodynamic analysis for slow tectonic loading with spontaneous rupture episodes on faults with rate- and state-dependent friction.” In: *Journal of Geophysical Research-Solid Earth* 105.B10 (Oct. 2000), pp. 23765–23789. ISSN: 2169-9313. DOI: `10.1029/2000JB900250`.

[5] S. Larochelle et al. “Constraining Fault Friction and Stability With Fluid-Injection Field Experiments.” In: *Geophysical Research Letters* 48.10 (2021). DOI: `10.1029/2020GL091188`.

[6] S. Larochelle et al. “Constraining Fault Friction and Stability With Fluid-Injection Field Experiments.” In: *Geophysical Research Letters* 48.10 (2021), e2020GL091188. DOI: `https://doi.org/10.1029/2020GL091188`.

[7] J. Rice. *Elasticity of Fluid-Infiltrated Porous Solids (Poroelasticity).* Nov. 1998. URL: `http://esag.harvard.edu/rice/e2_Poroelasticity.pdf`.

[8] A. Ruina. “Slip instability and state variable friction laws.” In: *Journal of Geophysical Research* 88.NB12 (1983), pp. 359–370. ISSN: 0148-0227. DOI: `10.1029/JB088iB12p10359`.

[9] K. Sirorattanakul et al. “Sliding and healing of frictional interfaces that appear stationary.” In: *In revision for Nature* (2024).

[10] K. Uenishi and J. R. Rice. “Universal nucleation length for slip-weakening rupture instability under nonuniform fault loading.” In: *Journal of Geophysical Research: Solid Earth* 108.B1 (2003). DOI: `10.1029/2001JB001681`.

Chapter 4

MODELING INTERMITTENT LABORATORY EARTHQUAKES IN ROCK GOUGE USING RATE-AND-STATE FRICTION WITH FLASH HEATING

4.1 Introduction

To study complicated dynamic slip processes in geological faults, Rubino et al. [24] conducted a lab experiment in which a dynamic frictional rupture along a pre-existing interface in an analog material spontaneously propagated into an interface region filled with rock gouge. The rupture was triggered along the interface of two pre-stressed Homalite-100 plates by bursting an electric wire embedded in the interface. The dynamic rupture experiments in Homalite have an important advantage over rocks as they allow to minituarize the dynamic phenomena due to much smaller (about 30 times) critical crack sizes in Homalite compared to rocks. Hence dynamic ruptures can be obtained in Homalite samples of 0.2 m × 0.2 m, whereas one would require rock samples of about 6 m to observe similar phenomena. The experiments feature additional realism in incorporating rock gouge along the interface, which is a highly granulated rock material found in the core of natural faults where fault slip occurs.

In the experiment, the dynamic rupture was arrested upon entering the fault gouge zone, after which intermittent dynamic slip events occurred by both further attempts of slip to enter the fault gouge zone from outside and by self-nucleation of dynamic slip from within the fault gouge zone. These experimental observations imply that the fault gouge exhibits both an initial strengthening effect that allows to arrest dynamic slip as well as a dynamic-weakening mechanism to allow for eventual slip acceleration.

Previous laboratory studies have shown that friction on Homalite-100 and fault gouge interfaces depends on the local slip rate and the slip history, as described by rate-and-state friction laws [9, 15]. More specifically, rate-and-state velocity-strengthening interfaces have increasing steady-state friction coefficient as slip rate increases, which is consistent with the observed initial strengthening effect in the fault gouge in [24], whereas velocity-weakening interfaces decrease their steady-state friction resistance as slip rate increases, which allow for runaway earthquakes and dynamic rupture propagation [9, 26, 21].

As the slip rate along the fault gouge reaches the dynamic seismic level (around 1 m/s), several dynamic-weakening mechanisms can be potentially activated due to shear heating, such as flash heating, thermal pressurization of pore fluids in the ambient gouge and bulk material, as well as melting [30, 7, 4, 29, 18, 10, 11, 8, 13, 6, 17, 5, 22, 20, 16]. The experiment contained no pore fluids and there was no evidence of macroscopic melting after the experiment. Hence the mechanism of flash heating, together with the initial strengthening effect due to rate-and-state velocity-strengthening friction properties, may explain the observed intermittent dynamic slip processes observed in [24]. During flash heating, the micrometre-scale tips of contacting asperities heat and weaken for large enough slip rates, resulting in a marked drop in frictional strength with a pronounced $1/V$ dependence on the slip rate V. Owing to the highly local and transient nature of the process, frictional strength is quickly recovered when the slip rate subsides.

Motivated by the experiment in [24], in this study, we conduct Finite Element (FE) simulations to model intermittent laboratory earthquakes in rock gouge using rate-and-state friction with flash heating dynamic-weakening mechanism. We explore the interface properties and / or loading conditions that can reproduce the experimental observations.

Section 2 introduces the problem setup and modeling approach we use to simulate the intermittent earthquakes triggered in the lab experiment. Section 3 presents the numerical results of several representative cases using our modeling, with different interface properties as well as loading conditions, and discusses possible explanations of the intermittent dynamic events observed in the lab experiment, including their arrest and re-nucleation. Finally, section 4 summarizes the main findings of this study and discussesfuture directions of simulating intermittent lab earthquakes in fault gouges.

4.2 Problem Setup and Modeling

In the experimental study on intermittent lab earthquakes [24], two pre-cut Homalite-100 blocks are compressed together at an angle as shown in Figure 4.1(a) and Figure 4.2(a)(b). Part of the contact interface has fine-particle rock gouge material inserted into it, to study the response of this fault-relevant material to dynamic rupture. The gouge particles are contained in a groove made on each of the Homalite-100 blocks at the gouge region. Therefore there is 1 mm Homalite wall surrounding the gouge region, as shown in Figure 4.2(b). Two wires are put on the interface to trigger dynamic slip events by electrical discharge, as shown in Figure 4.1(a), and they are used to trigger two ruptures one after the other. In this study, we focus on the sequence of events after the first rupture initiation, using the wire placed at 85 mm from the left edge of the interface. The experimental measurements are done using dynamic DIC within a field of view around the rock gouge portion of the interface.

The evolution of slip rates along the interface with time inferred from experimental measurements is shown in Figure 4.1(b). The color scale ranges from black at 0 m/s, to red at 1 m/s and finally blue at 2 m/s or higher. We can see dynamic rupture arriving at the interface at around 40 μs in two branches, one inter-sonic and one sub-Rayleigh. They both get arrested at around $x_1 = 15$ mm. Then another self-contained event nucleates at around 85 μs, $x_1 = 15$ mm, and is arrested shortly after. The self-nucleated rupture initiates at where the first ruptures entering from the Homalite interface get arrested, potentially due to stress concentration formed locally. In the experiments described in [24], they initiated a second sequence of ruptures on the same specimen, and they still observed that there is a self-nucleated rupture starting at where the first ruptures get arrested, even if the exact location of the self-nucleation is no longer $x_1 = 15$ mm.

In our simulations, we would like to reproduce the arrival of the two branches of the initial rupture, their arrest, and the re-nucleation and arrest of the second rupture in the gouge.

The experiment also reveals first strengthening and then dynamic weakening of friction in the gouge (Figure 4.1c). At the location of $x_1 = 8$ mm in the gouge zone, the friction at the interface first increases as the initial rupture arrives, and then decreases dramatically as slip rate goes above 2 m/s. This indicates that the friction of the gouge region first increases as the slip rate increases and then dynamically weakens as slip rate stays high.

Homalite-100 blocks: Linear elastic material

While Homalite-100 is a viscoelastic strain-rate-dependent material, its response during dynamic rupture can be well approximated by treating it as a linear elastic material with appropriately chosen elastic constants [23].

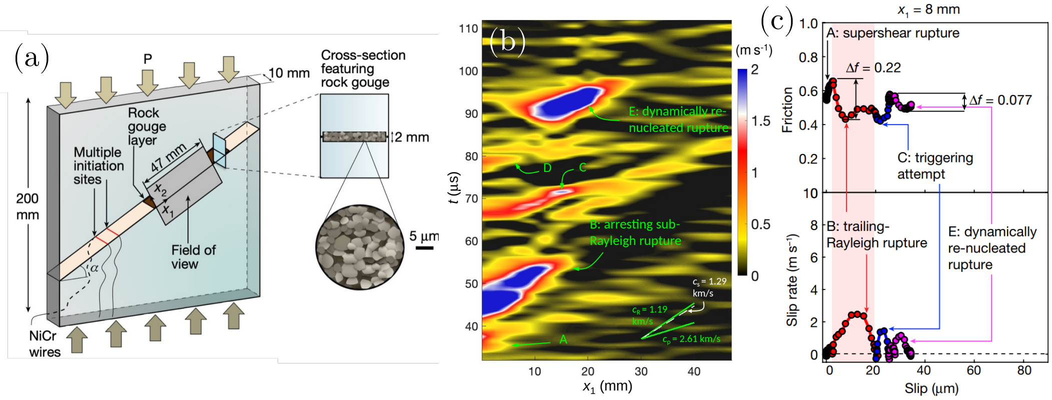

Figure 4.1: Experimental setup and results from [24]. (a) A faulted Homalite-100 plate with part of the interface containing a rock gouge layer with the mean particle size less than 5 microns. The measurements of the response of the gouge layer to the incoming dynamic rupture are done through dynamic DIC with the indicated field of view. (b) Evolution of slip rates inferred along the interface within the field of view as a function of time. After the initial rupture arrives and gets arrested (40 to 50 μs) at around $x_1 = 15$ mm, dynamic slip re-nucleates in the gouge layer at the same location, $t = 80$ μs. (c) Friction coefficient and slip rate in the gouge layer at the location of $x_1 = 8$ mm show the initial strengthening effect as the slip rates increase with rupture arrival, and then dynamic-weakening effect after the slip rate exceeds 2 m/s, which within a similar range as previous studies on flashing heating slip rates of fault gouge [11, 13].

Then the governing equations of the Homalite-100 blocks are:

$$G\boldsymbol{\nabla}^2\boldsymbol{u}(\boldsymbol{x},t) + \frac{G}{1-2\nu}\boldsymbol{\nabla}(\boldsymbol{\nabla}\cdot\boldsymbol{u}(\boldsymbol{x},t)) = \rho\frac{d^2\boldsymbol{u}(\boldsymbol{x},t)}{dt^2}, \text{for } \boldsymbol{x} \in \Omega,, \tag{4.1}$$

where $\boldsymbol{u}(\boldsymbol{x},t)$ is the displacement at location $\boldsymbol{x}$ and time t, ρ is the mass density, G is the shear modulus, and ν is the Poisson's ratio. The parameters we use in the simulations are listed in Table C.1.

Fault constitutive model: Rate-and-state friction with flash heating effect

Previous studies have determined that Homalite-100 interfaces have rate-and-state frictional properties with flash-heating dynamic-weakening effect ([31, 14, 20]). In general, friction laws with rate-and-state dependence can be formulated by

$$\tau(\boldsymbol{x},t) = f\left(V(\boldsymbol{x},t),\theta(\boldsymbol{x},t)\right)\sigma(\boldsymbol{x},t), \text{for } \boldsymbol{x} \in I, \tag{4.2}$$

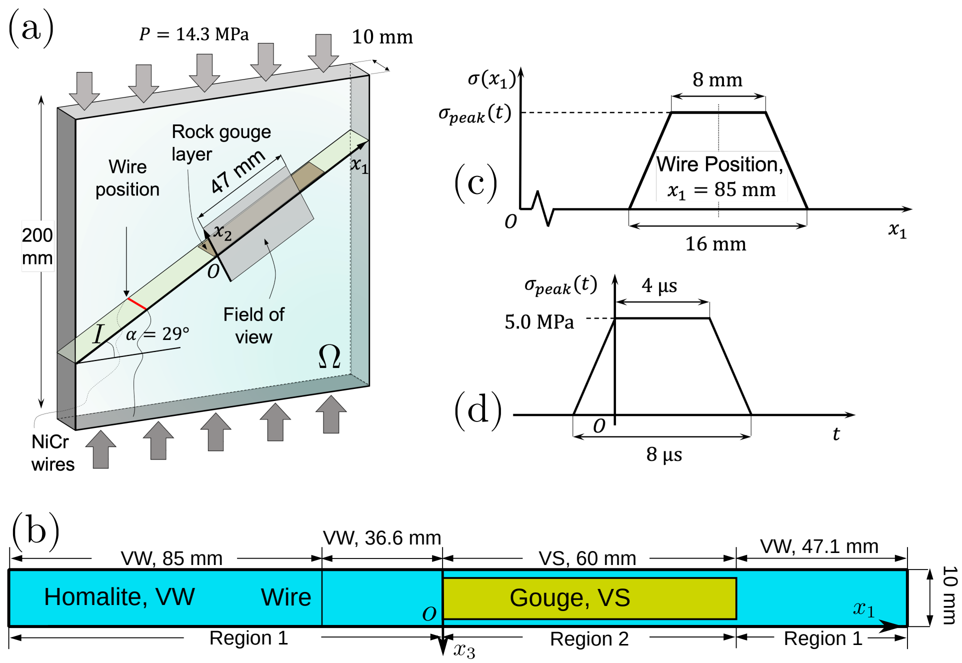

Figure 4.2: Setup for the numerical modeling of the experiments. (a) 3D finite element model inspired by the lab experiment in [24]. 2 pieces of Homalite-100 (Ω) are pressed together by unaxial load $P = 14.3$ MPa via a frictional interface (I). The part of the interface with the rock gouge layer is modeled with different frictional properties than Homalite-100. Dynamic rupture is triggered by introducing a normal stress perturbation along the interface motivated by wire explosion in the experiment. (b) Schematics of the frictional interface with the locations of the wire and rock gouge. The Homalite-100 and rock-gouge portions of the interface are modeled with velocity-weakening (VW) and velocity-strengthening (VS) rate-and-state friction, respectively. Region 1 is Homalite-100 only while region 2 has gouge embedded in Homalite. Note that the gouge zone is surrounded by a thin wall of Homalite at the front and back surfaces. (c) Normal-stress perturbation as a function of position (x_1) along the fault at time t. The symmetric trapezoid is centered at the wire position. (d) Peak value of normal stress perturbation as a function of time t. The effective wire explosion time ($t = 0\ \mu$s) is modeled as the first time σ_{peak} reaches its maximum. Note that we do not have measured data for the explosion and,unless specified otherwise, we adjust the explosion parameters to match the arrivel of the initial rupture arrives at the edge of the field of view at around 40 μs.

where $\tau(\boldsymbol{x}, t)$ is the shear stress, $\sigma(\boldsymbol{x}, t)$ is the corresponding normal stress, $V(\boldsymbol{x}, t)$ is the slip rate, and $\theta(\boldsymbol{x}, t)$ is the state variable at $\boldsymbol{x}$ and t. The friction coefficient formulation $f(V, \theta)$ can include both rate-and-state dependence and flash heating effect. We adopt the formulation of rate-and-state friction by Dieterich [9, 25].

$$f_{RS}(V, \theta) = f_* + a \log\left(\frac{V}{V_*}\right) + b \log\left(\frac{V_* \theta}{D_{RS}}\right), \tag{4.3}$$

where f_*, V_* are the reference friction coefficient and slip rate, D_{RS} is the characteristic slip distance, a and b are non-dimensional rate-and-state parameters.

For the evolution law of the state variable θ, we consider boht the aging law [9]:

$$\frac{d\theta}{dt} = 1 - \frac{V\theta}{D_{RS}} \tag{4.4}$$

and the slip law [25]:

$$\frac{d\theta}{dt} = -\frac{V\theta}{D_{RS}} \log\left(\frac{V\theta}{D_{RS}}\right). \tag{4.5}$$

We start by conducting simulations with the aging law and then compare selected results with those for the slip law, explicitly identifying the simulations with the slip law. The steady-state friction behavior, i.e., when $d\theta/dt = 0$, is the same for both aging and slip law:

$$\theta^{ss} = \frac{D_{RS}}{V_{ss}}, \tag{4.6}$$

$$f_{RS}^{ss} = f_* + (a-b)\log\left(\frac{V^{ss}}{V_*}\right). \tag{4.7}$$

In the steady state, when $a - b > 0$, f_{RS}^{ss} increases with V^{ss}, which is known as velocity-strengthening (VS) friction. Similarly, if $a - b < 0$, the steady-state friction is velocity-weakening (VS). In the following, when refering to VW or VS rate-and-state properties, steady-state properties are implied.

Flash heating effect dynamically weakens the fault interface when it is slipping at high enough slip rates to just weaken the tips of contacting asperities without macroscopic melting [30, 20, 4, 11]. In this study, we use the same flash heating formulation as in [28]:

$$f(V,\theta) = f_w + \frac{f_{RS}(V,\theta) - f_w}{1 + D_{RS}/(\theta V_w)}, \tag{4.8}$$

where V_w is the slip rate at which flash heating becomes important and f_w is the limit of the lowest friction coefficient due to flash heating. The friction parameters used for Homalite-100 interfaces are listed in Table C.2, while the friction parameters for the gouge zone are different in different simulated cases and will be discussed in the Results section.

Numerical implementation of the physical modeling

We build our finite-element numerical model within the framework of PyLith, an open source Finite Element Library software with user interface for new material and interface constitutive models [3, 1, 2]. For the elastic bulk, weak form of (4.1) is solved explicitly under finite-element spatial discretization, with lumped mass matrix. The unknown tractions at the fault interface are solved essentially as the Lagrangian multipliers to ensure both non-penetration condition in the fault-normal direction and friction constitutive relations in the fault-tangential directions.

Denote the displacement at two sides of the interface of I as $\boldsymbol{u}_+$ and $\boldsymbol{u}_-$. To advance the solution from t_n to $t_{n+1} = t_n + \Delta t$, PyLith uses a prediction-correction scheme to enforce that the fault constitutive formulation is satisfied along the interface. First, it makes an initial attempt step with $\boldsymbol{u}^*(t_{n+1})$ solved with $\boldsymbol{u}^*_+(t_{n+1}) - \boldsymbol{u}^*_-(t_{n+1}) = 0$, i.e., no additional slip happens. That gives the required traction at the interface, both the shear component τ^* and the normal component σ^*, if no additional slip occurs. Then the governing equations of the fault interface, i.e., (5.1, 4.4, 4.8) are applied to modify the shear stress τ^*, such that it satisfies the friction constitutive relations of the interface. Next, the displacement field is updated to reconcile the change in τ^* due to the modification step. The updated displacement field would change the required traction at I to satisfy balance of linear momentum (4.1), and also the friction coefficient if the friction coefficient depends on the slip history. PyLith loops the above process until both (4.1) in Ω and (5.1, 4.3, 4.8) are satisfied and reports the corresponding displacement field as $\boldsymbol{u}(t_{n+1})$ [1, 2].

When the rate-and-state aging law for the evolution of the state variable θ is used, PyLith follows the scheme proposed by Kaneko et al. [12, 1] to advance θ from t to $t + \Delta t$, :

$$\theta(t_{n+1}) = \theta(t_n) \exp\left(\frac{-V(t_n)\Delta t}{D_{RS}}\right) + \frac{D_{RS}}{V(t_n)}\left[1 - \exp\left(\frac{-V(t_n)\Delta t}{D_{RS}}\right)\right], \tag{4.9}$$

which essentially integrates (4.4) from t_n to $t_{n+1} = t_n + \Delta t$, assuming that V is constant through the step at $V(t_n)$.

4.3 Results and discussion

In the simulations, we explore and identify the parameters and conditions of the fault gouge that would lead to the following experimental observations as shown in Figure 4.1: Initial super-shear and sub-Rayleigh rupture fronts arrives at the edge of the gouge region at around 36, 40 μs, and gets arrested at $x_1 \approx 15$ mm; Then, a secondary dynamic rupture self nucleates at around 85 μs within the gouge region, and it is self-contained.

We start with a baseline model in which the entire interface has the friction and flash heating properties of Homalite-100, to verify that our finite element model is working properly, and that we get the expected rupture propagation within the Homalite-100 interface. Then, we consider velocity-strengthening friction with flash-heating parameters in the fault gouge zone, chosen based on point-wise measurements of slip rate and friction shown in Figure 4.1(b).

Baseline: Through-going rupture for pure Homalite-100 interface with VW rate-and-state friction and flash heating

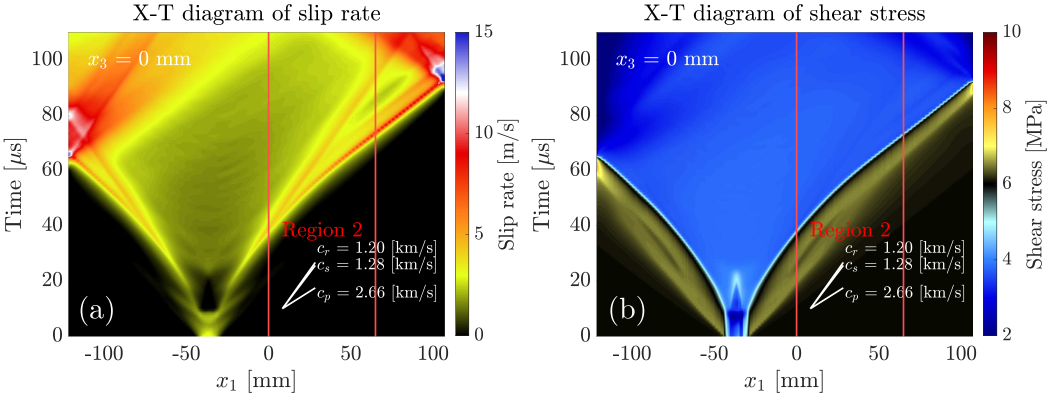

Figure 4.3: Case 1: The fault interface has uniform Homalite-100 friction properties (no fault gouge is involved). Evolution of (a) slip rate and (b) shear stress. The initial slip rate over the entire interface is set to be $V_{initial} = 10^{-7}$ m/s. The interface has uniform friction parameters and initial condition. Shear, pressure and Rayleigh wave speeds are marked as c_s, c_p and c_r, respectively. Note that the results plotted are at the front surface $x_3 = 0$ mm where they are observed in the experiment. We see that rupture propagates over the entire pure Homalite interface as expected based on prior experiments. The rupture starts as sub-Rayleigh and then transitions into intersonic rupture speeds (often called super-shear), with the propagating Rayleigh signature as the remnant of the original sub-Rayliegh front, consistent with observations in Figure 4.1(b) of two fronts arriving at the gouge portion of the interface.

As a baseline for further comparison, we first simulate a dynamic rupture on purely Homalite interface, with no rock gouge, and observe that the initiated rupture propagates through the entire interface (Figure 4.3) as expected based on prior experiments [23]. After the rupture is initiated at the location of the wire explosion, it first propagates in both directions at a sub-Rayleigh wave speed. Then, after around 30 μs, the rupture transitions to intersonic rupture speeds. The two rupture fronts with different wave speeds arrive at the edge of region 2 where the rock gouge is in the experiment at approximately $36, 40$ μs, consistent with events "A" and "B" in the experiment (Figure 4.1). Eventually, the rupture gets reflected at the two lateral of the sample in x_1 direction.

In the shear stress plot, we observe that at any location x_1 along the interface, the shear stress first rises when the rupture arrives, which is consistent with stress concentration at the rupture front and matches the rate-and-state direct effect [9, 19]. Then the shear stress drops significantly first due to the rate-and-state weakening and then due to the flash heating (FH) dynamic-weakening mechanism imposed by (4.8).

Arrest of rupture in the velocity-strengthening rock gouge

To start considering the effect of the gouge zone, we introduce velocity-strengthening friction (first without flash heating) for Region 2. Experiments on nominally stationary frictional interfaces loaded in compression and shear [27] suggest that, depending on how long the Homalite-100 plates have been held together before the rupture is initiated in the experimental setting, the initial slip rate $V_{initial}$ ranges from 10^{-9} m/s to 10^{-7} m/s. Here we set $V_{initial}$ to be 10^{-7} m/s. The specific parameters are listed in Table C.3.

We can see that dynamic rupture gets arrested in the velocity-strengthening region of the interface that represents rock gouge. Then later at around 80 μs, another rupture enters the gouge region from the Homalite-100 region and is arrested again by the fault gouge. This second rupture is caused by the continuing slip away from the gouge region. The shear stress plot shows that the ruptured region experiences flash-heating weakening. When the shear stress is plotted at the front surface $x_3 = 0$ mm, where the material is Homalite-100 throughout the sample, we see weakening after the rupture front even in Region 2. To see the effect of the VS properties, we plot shear stress along the centerline of the fault $x_3 = -5$ mm, in the middle of the Homalite plate. Indeed, the stress goes up significantly in that portion of the interface, arresting the rupture. At the same time, the slip rate does not vary much in x_3 direction, as expected in this nearly 2D experimental configuration.

We find that the velocity-strengthening fault gouge can indeed arrest the initial dynamic rupture as expected. However, for the purely VS properties, there is no re-nucleation of slip. Next, we incorporate flash-heating-like dynamic-weakening

(a) X-T diagram of slip rate (b) X-T diagram of shear stress

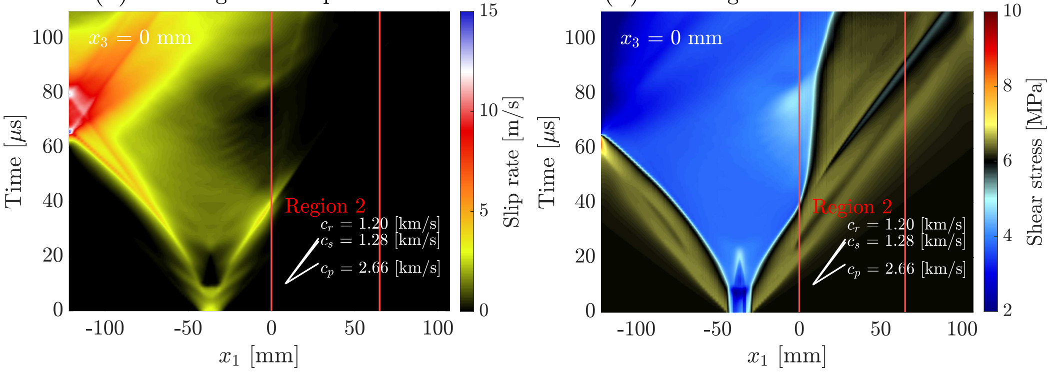

(c) X-T diagram of slip rate difference (d) X-T diagram of shear stress

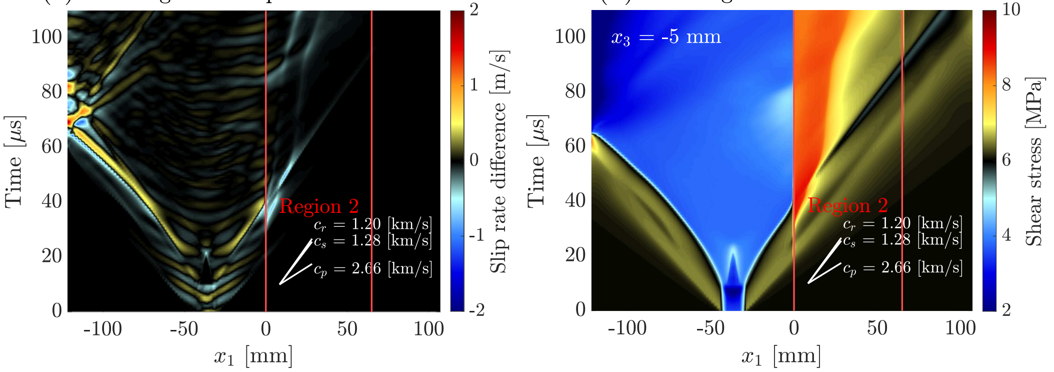

Figure 4.4: Case 2: Homalite-100 interface with VS fault gouge (no flash heating). (a) x_1-Time diagram of slip rate, measured at $x_3 = 0$ mm (the surface of the sample). (b) x_1-Time diagram of shear stress, measured at $x_3 = 0$ mm. (c) x_1-Time diagram of slip rate differences between $x_3 = -5$ mm (the center line of the 2D interface) and $x_3 = 0$ mm, note that the color scale is changed to $[-2, 2]$ m/s to show that the difference is small. (d) x_1-Time diagram of shear stress, measured at $x_3 = -5$ mm. The initial slip rate over the entire interface is set to be $V_{initial} = 10^{-7}$ m/s. The plot marking are similar to Figure 4.3. The gouge layer with VS friction arrests the initial rupture upon its arrival. A secondary rupture arrives at the gouge layer at around 80 μs. We also notice that the slip-rate difference in x_3 direction is not significant compared to its magnitude, while the difference in shear stress is significant due to the transition from velocity-weakening Homalite to velocity-strengthening gouge, as x_3 decreases from 0 mm to -5 mm.

mechanism into the fault-gouge region.

Velocity-strengthening gouge region with dynamic weakening due to flash heating

As we further include flash-heating dynamic-weakening effect in the gouge zone (Figure 4.5), we find that the arrest of the initial rupture can still be reproduced for the appropriately chosen flash-heating parameters. Note that in (a), we see some intermittent increase and decrease in the slip rate, and this is due to the waves transversing in the x_3 direction, which will clear later from a comparison with a 2D simulation. The secondary rupture still comes back to the gouge zone at around 80 μs from the Homalite region of the interface, and this time the rupture is not arrested but rather propagates through due to activated flash heating. Hence this model succeeds in reproducing some intermittency of slip in the gouge portion of the interface, but not the kind that occurs in the experiment.

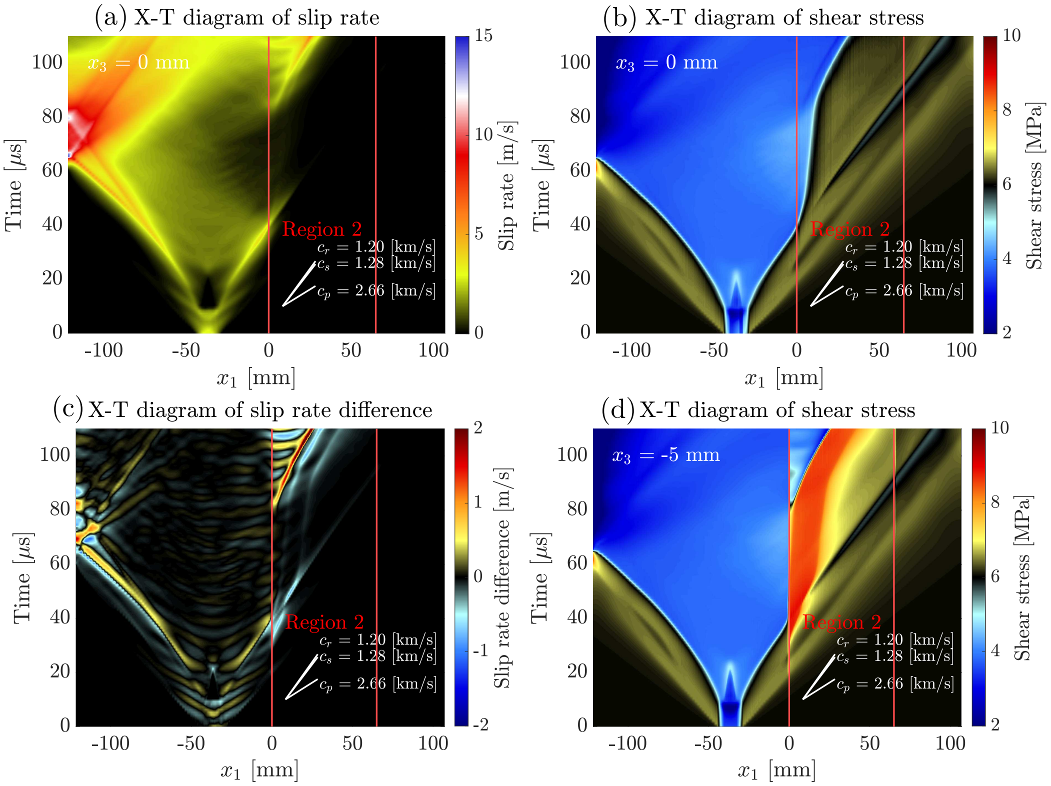

Figure 4.5: Case 3: Homalite-100 interface with VS and FH fault gouge. (a) x_1-Time diagram of slip rate, measured at $x_3 = 0$ mm. (b) x_1-Time diagram of shear stress, measured at $x_3 = 0$ mm. (c) x_1-Time diagram of slip rate differences between $x_3 = -5$ mm and $x_3 = 0$ mm, note that the color scale is changed to $[-2, 2]$ m/s to show that the difference is small. (d) x_1-Time diagram of shear stress, measured at $x_3 = -5$ mm. The initial slip rate over the entire interface is set to be $V_{initial} = 10^{-7}$ m/s. The plots have markings similar to Figure 4.4. We observe that adding flash-heating (FH) dynamic-weakening effect to the VS region allows for the secondary rupture at around 80 μs to propagate into the gouge layer.. In (d) we see that the shear resistance of the gouge layer first strengthens and then dynamically weakens due to the imposed FH effect, producing the intermittancy in slip.

For a more detailed comparison between the experiment and the simulated cases, let us consider slip rates within the experimental field of view and at the same slip-rate scale (Figure 4.6). In the simulation with uniform Homalite interface (no gouge), the arrival time of the rupture at the edge of the observation window is reproduced. With gouge modeled as a VS region, we are able to reproduce the arrival and arrest of the initial rupture around 40 μs; furthermore, we also reproduce a subsequent attempt for slip to penetrate from Homalite into the gouge (at around 80 μs), but it is much stronger and somewhat later than the corresponding attempts in the experiment (events C and D in panel a). Further, with velocity-strengthening plus flash-heating gouge friction properties, we are able to obtain a secondary rupture in the gouge — and hence some slip intermittancy — that has the same slip rate as the experiment. However, the simulated second rupture arrives from the Homalite zone (rather than nucleates from within the gouge) and it is not self-contained.

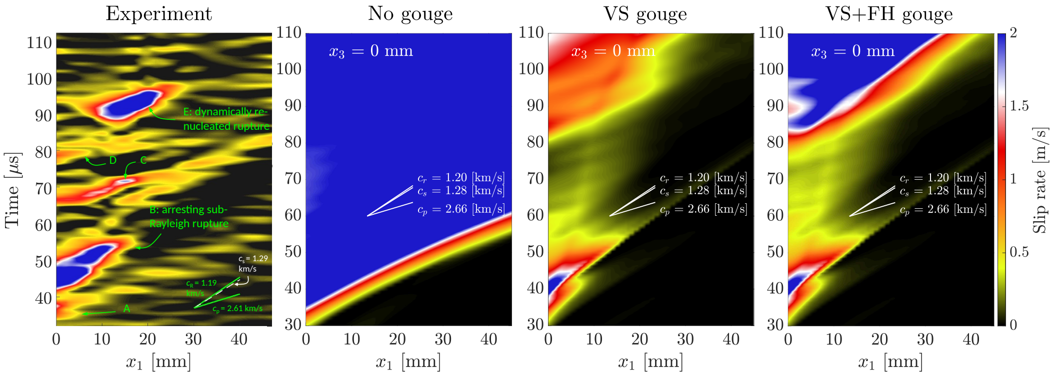

Figure 4.6: x_1-Time diagrams of slip rates along the interface within the field of View from (left to right) the experiment; Homalite-only interface (case 1) Homalite with velocity-strengthening (VS) gouge (case 2); and Homalite with VS and flash-heating (FH) gouge (case 3). Note that here, the color scale for slip rates is $[0, 2]$ m/s as in the experimental measurements. The simulation of case 2 reproduces several features of the experiment but does not reproduce a self-nucleating seclf-contained event E observed in the experiment.

As already mentioned, the shear stress on the interface varies significantly with x_3 (the thickness of the plate) because of the transitioning from Homalite to gouge at $x_3 = -1$ mm. Let us compare shear stress between the experimental measurements and simulated values at $x_3 = \{0, -2, -5\}$ mm for case 3 (Figure 4.7). Note that the initial shear stress is 6.06 MPa. In the simulations, the shear stress changes at at $x_3 = 0$ mm are largely negative, consistent with weakening in Homalite. The shear stress changes deeper into the interface are strengthening due to the VS nature of the interface.

However, the experimental shear stress measurements indicate both negative and positive shear stress changesk, despite the measurements being done at $x_3 = 0$ mm. This implies that the experimental results of shear stress is some average of the shear stress through the thickness of the interface. Such averaging can be explained by the fact that the DIC uses a finite-size pixel set to estimate displacements and that size is 51×51 pixels in the experimental study. Note that the slip rates are nearly uniform across the thickness, so such averaging is not an issue for them.

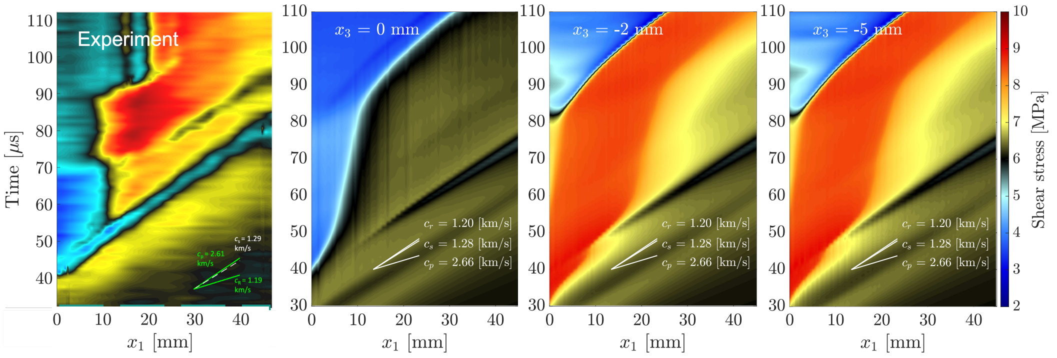

Figure 4.7: x_1-Time diagrams of shear stress along the interface within the field of view from the experiment and for case 3 at different x_3. The experimental measurement is likely some average of the shear stress at different x_3's, as a result of the DIC algorithm used to estimate displacements.

To check the numerical convergence of our simulations, and in particular that the small-scale oscillations in case 3 (right-most panel in Figure 4.6) are physical rather than numerical, we simulate case 3 with three different meshes of edge lengths $2, 0.5, 0.1$ mm, respectively (Figure 4.8). We see that the results do not appreciably change with the mesh refinement and that the oscillations in the results are indeed physical, due to the good mesh convergence shown. The plots also illustrate how the friction coefficient first increases due to the velocity-strengthening rate-and-state properties of the gouge, and then decreases due to flash-heating dynamic-weakening mechanism.

To check whether using slip law for the evolution of state variable θ would give us qualitatively different results, we run case 3 with the slip law (4.5) instead of the aging law of the state variable evolution.. We find that the rupture behavior is qualitatively similar (Figure 4.12). Note that, under the same explosion condition, the case with slip law requires much larger D_{RS} to result in similar rupture propagation, as also found by [28].

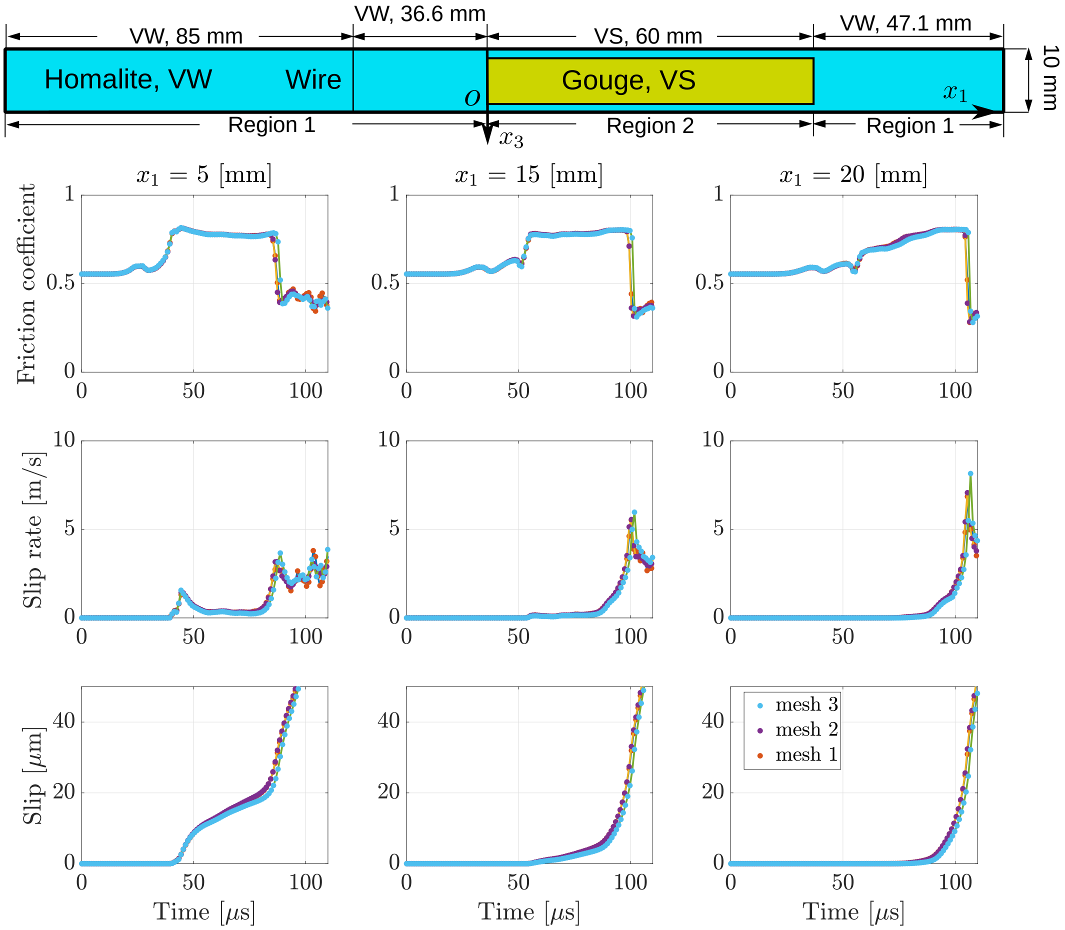

Figure 4.8: Friction coefficient, slip rate, and slip vs. time at $x_3 = -5$mm, three locations along the field of view, and three meshes with edge lengths of around $2, 0.5, 0.1$ mm. The results show convergence with the mesh refinement.

The behavior of the secondary rupture depends on the initial slip rate over the interface

We test the sensitivity of our simulations results to the initial conditions over the interface, specifically the initial slip rate that indicates the degree of healing based on interface-holding experiments ([27]). In addition to case 3 with $V_{initial} = 10^{-7}$ m/s, we simulate two more cases with $V_{initial} = 10^{-8}$ m/s and $V_{initial} = 10^{-9}$ m/s. From the rate-and-state formulation (4.3), we can compute the corresponding initial value for the state variable θ by

$$\theta_{initial} = \frac{D_{RS}}{V_*} \exp\left(\frac{\tan(\alpha) - f_* - a\log(V_{initial}/V_*)}{b}\right). \tag{4.10}$$

Let us first keep the parameters of the initiation explosion unchanged. With the

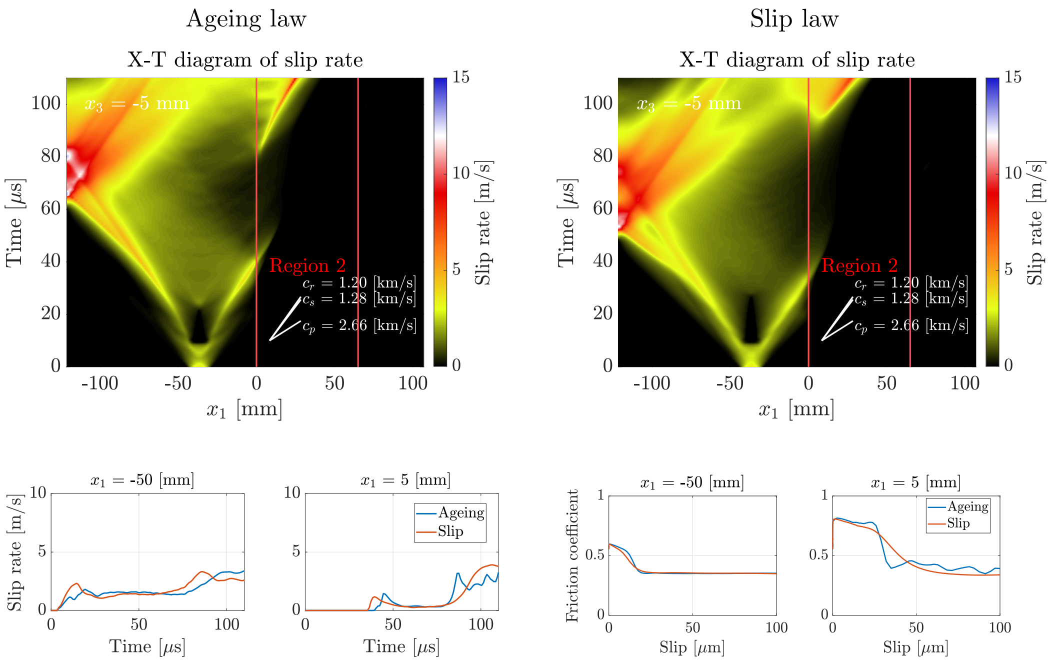

Figure 4.9: Comparison between aging and slip law for case 3. (Top row) x_1-Time plots of slip rates with the same parameters as case 3, except the value of D_{RS} (1.5 μm for the ageing law, 8 μm for the slip law). (Bottom row) Slip rate vs. time (left) and friction coefficient vs. slip (right) in the Homalite ($x_1 = -50$ mm) and gouge ($x_1 = 5$ mm) portions of the interface. The results with the two laws are qualitatively similar.

same explosion, reducing the initial slip rate would significantly delay the arrival of the initial rupture (Figure 4.10), consistent with the notion that lower initial slip rates correspond to more healed interface.

Let us now adjust the parameters of the explosion, as we change the initial slip rates on the interface, to match the first rupture arrival at the gouge layer at around 40 μs (Figure 4.11).

For both aging and slip laws, the second rupture becomes much less dynamic as the initial slip rate reduces from 10^{-7} to 10^{-9} m/s. The ageing and slip laws produce qualitatively similar results, with the slip law having more smooth profiles because of larger D_{RS}. We also notice that even if the second rupture is significantly impaired by the reduced slip rate, in all the cases it starts re-entering the gouge zone at around 80 μs.

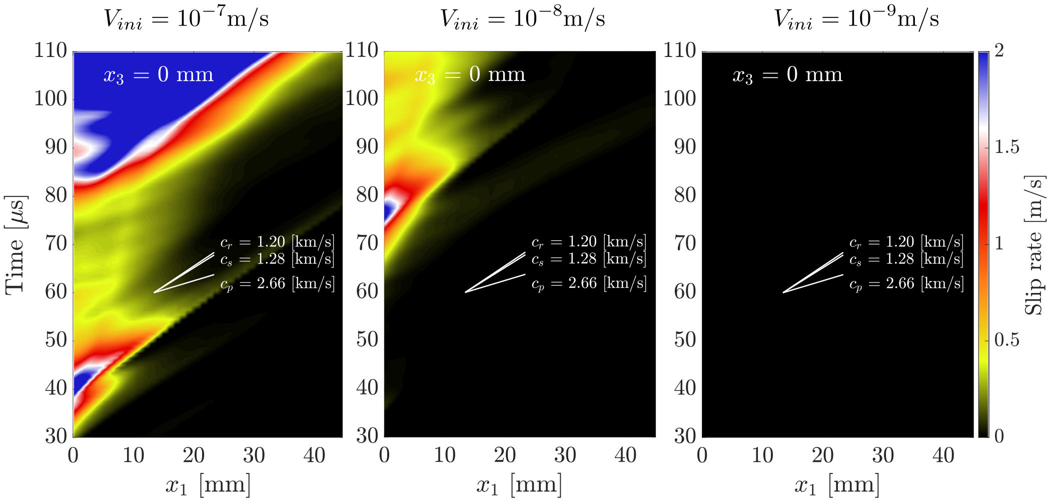

Figure 4.10: Evolution of slip rates with time over the interface within the field of view for case 3 ($V_{initial} = 10^{-7}$ m/s), and two more initial slip rates, $V_{initial} = 10^{-8}$ m/s, $V_{initial} = 10^{-9}$ m/s. All the other parameters are the same.. We can see that under the same explosion, reducing the initial slip rate would delay the arrival time of the initial rupture, consistent with more healed interfaces.

Self-nucleation by introducing a more efficient weakening patch in the gouge zone

From the cases shown above, we find that gouge with velocity-strengthening plus flash heating friction properties is able to arrest the first rupture arriving at the interface at around 40 μs, and then a second rupture enters from the Homalite region into the gouge at around 80 μs, and it is never arrested. However, in the experimental result shown in Figure 4.1, the prominent second rupture self-nucleates within the gouge zone, and it is arrested shortly after nucleated. We have considered cases with different explosion parameters, friction parameters, initial conditions, etc., and find that, with uniform friction properties in the Homalite and gouge zone and with our formulation of (4.3, 4.8), the second rupture always initiates from the Homalite at around 80 μs instead of self-nucleating in the gouge. Furthermore, the flash heating by (4.8) makes the second rupture difficult to be arrested once initiated.

To illustate what kind of feature could nucleate a self-contained second rupture at where the first ruptures get arrested, i.e., around $x_1 = 15$ mm, we introduce a patch in the gouge zone that develops enhanced flash heating with slip and then reverts back to the original flash-heating properties (Figure 4.12). Specifically, the characteristic slip rate for flash heating, V_w, first reduces with slip from the characteristic value for gouge of 2 m/s to a much smaller value of 0.1 m/s or 0.01 m/s more appropriate

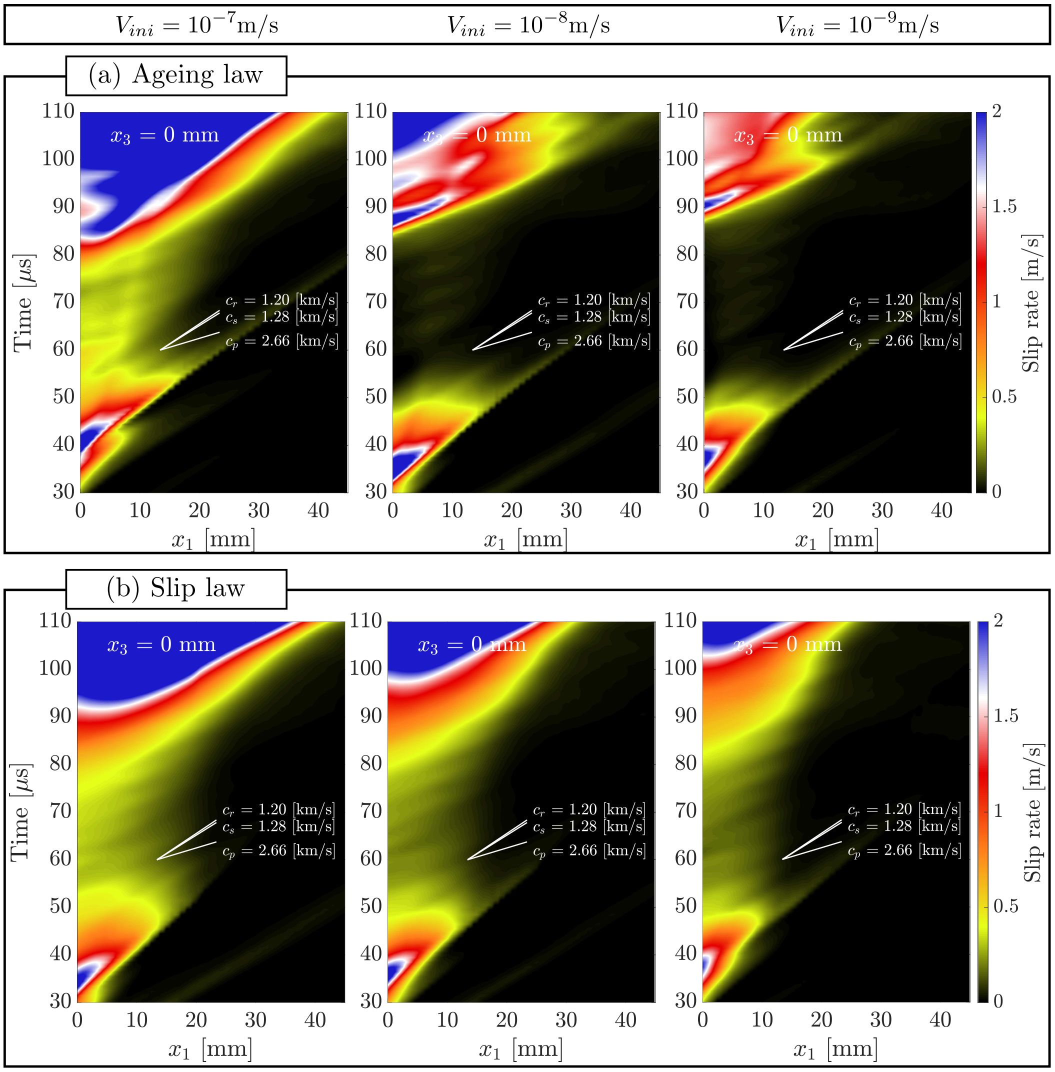

Figure 4.11: Evolution of slip rates with time over the interface within the field of view for case 3 ($V_{initial} = 10^{-7}$ m/s), and two more initial slip rates, $V_{initial} = 10^{-8}$ m/s, $V_{initial} = 10^{-9}$ m/s, for both ageing (a) law and (b) slip law, while tuning the explosion parameters such that the initial rupture arrives in the gouge zone at around 30 to 40 μs as in the experiment. Reducing the initial slip rate over the interface makes the secondary rupture significantly less dynamic. However, the secondary rupture still enters the field of view at around 80 90 μs in all six cases. Slip law has more smooth ruptures because the suitable D_{RS} is larger.

for bare rock surfaces ([20]) and then recovers back to its original value. Physically, this would correspond to shear localizing to nearly a single slip surface in the gouge and then delocalizing to a more finite-width shear layer. Based on the flash-heating formulation (4.8), such a variation in V_w would first make friction coefficient $f(V, \theta)$ decrease to the flash-heating weakened value f_w for much lower values of slip rate but then would remove this feature.

Since the uniform velocity-weakening Homalite interface always result in a strong coming-back rupture at around 80 μs which would interfere with the self-nucleation we are trying to reproduce, we further introduce a region in Homalite to the left of the wire (Figure 4.12a) that has different rate-and-state properties to impair sliding in Homalite that causes the rupture to come back to the gouge at 80 μs.

With these modifications, we can reproduce the self-nucleation and arrest of an event in the fault gouge for both aging and slip laws (Figure 4.12c).. The simulated events are qualitative similar to the experimental result in Figure 4.1(a). The needed reduction of V_w is 0.1 m/s for the slip law and 0.01 m/s for the aging law, and the latter value is potentially too small to be realistic (Rice, 2006 [20]; Goldsby and Tullis, 2011 [11]); in that sense, the slip law is doing a better job. Figure 4.12(d) and (e) shows the nucleation and arrest process within the patch for slip law. We clearly see that a dynamic event nucleates within the thickness of the interface and then spreads to the lateral surfaces. As the enhanced flash heating disappears, shear stress recovers and slip rate drops down. This result suggests that a localization-delocalization process in the gouge region possibly causes the self nucleation and arrest observed in the experiment. The process occurs at the location of shear stress concentration left by the arrest of the initial rupture, where there is constant creep with non-negligible slip rates potentially contributing to this process.

An important remark here is that the Homalite wall surrounding the the gouge zone is important in the self-nucleation, because for V_w to decrease to its low value, the cumulative slip at the location needs to reach several microns, and the surrounding Homalite region fosters slip in the patch. We have run a case without the surrounding Homalite region and under the same explosion, initial condition and friction parameters, and no self-nucleation is achieved.

Comparing 3D and 2D simulations

Since the specimen is 200 mm long and wide, but only 10 mm thick, a natural question to ask is how much feature we will be able to capture just with a 2D simulation in plane-stress. We here run a case with the same material parameters and initial condition as case 3 in 2D. However, in 2D simulation there will be no Homalite region surrounding the gouge zone as the 3D simulation, since x_3 direction does not exist. It turns out that the surrounding Homalite region makes it easier for the rupture to propagate, and the difference is noticable.

Figure 4.13 (a) and (b) shows the x_1-Time diagrams of case 3 (3D) and its corresponding 2D case. The 3D case is plotted at $x_3 = -5$ mm. The initial slip rate over the interface is set to be $V_{initial} = 10^{-7}$ m/s. From (a)(b) we see that the 3D case and 2D case have the same rupture propagation patterns, while the slip rate is higher. Figure 4.13 (c) shows the friction coefficient vs. time, as well as slip rate vs. time. We observe that the friction coefficient is similar within the Homalite ($x_1 = -5$ mm) and the gouge ($x_1 = 5$ mm). However, the slip rate is usually higher in the 3D case. We conjecture that there are two main factors that causes the slip rate in 3D simulations to be more dynamic. First, the 3D case has free surfaces at $x_3 = -10$ mm and 0 mm, while the 2D plane stress case assumes uniform affine deformation in x_3 direction, which is putting more constraints than the 3D case. Second, the 3D case has a thin wall of Homalite surrounding the gouge region, and Homalite is velocity-weakening.

To verify that both factors contribute to more dynamic slip in the 3D case, we run a 3D case but without the Homalite wall surrounding the gouge region. Figure 4.13(d) shows the x_1-Time diagrams of 3D, 3D without Homalite wall and 2D case. We see that the 3D case without the Homalite wall has lower slip rate in the “Field of View", and the second rupture arrives later. This confirms that the Homalite wall contributes to the more dynamic slip. Comparing the 3D case without the wall to the 2D plane stress case, we see that the first rupture is less dynamic in the 2D case, and the slip rate between 40 and 80 μs is lower. This signifies that the free surface also makes the slip more dynamic. To further verify that the free surface fosters more dynamic slip, Figure 4.13(e) compares the snapshots of slip rates on the interface. From it we can see that when the slip front is still in the Homalite, the 3D cases, with or without the Homalite wall, both have a rupture front that is convex, i.e., the front travels faster close to the boundaries of $x_3 = -10$ mm and 0 mm. We also notice that there is a higher peaker slip rate in the 3D cases than in the 2D case. When the rupture front enters the gouge zone (marked by Region 2 in (e)), Since the original 3D case has a thin Homalite wall at the boundaries, the front becomes even more convex. The 3D case without the Homalite wall still has a convex front, while the 2D case, by construction can only have a flat front. After the rupture enters the gouge zone, the 2D case has the lowest slip rate, while the original 3D case has the highest slip rate. This comparison confirms that both the free surface and the Homalite wall surrounding the Homalite region contribute to the fact that 3D case has more dynamic rupture propagation. Given the significant difference of the 3D versus 2D simulations, we conclude that it is necessary to conduct 3D simulations, not only so that we do not under estimate the slip rates, but also for slip front that is non-planar in the x_3 direction.

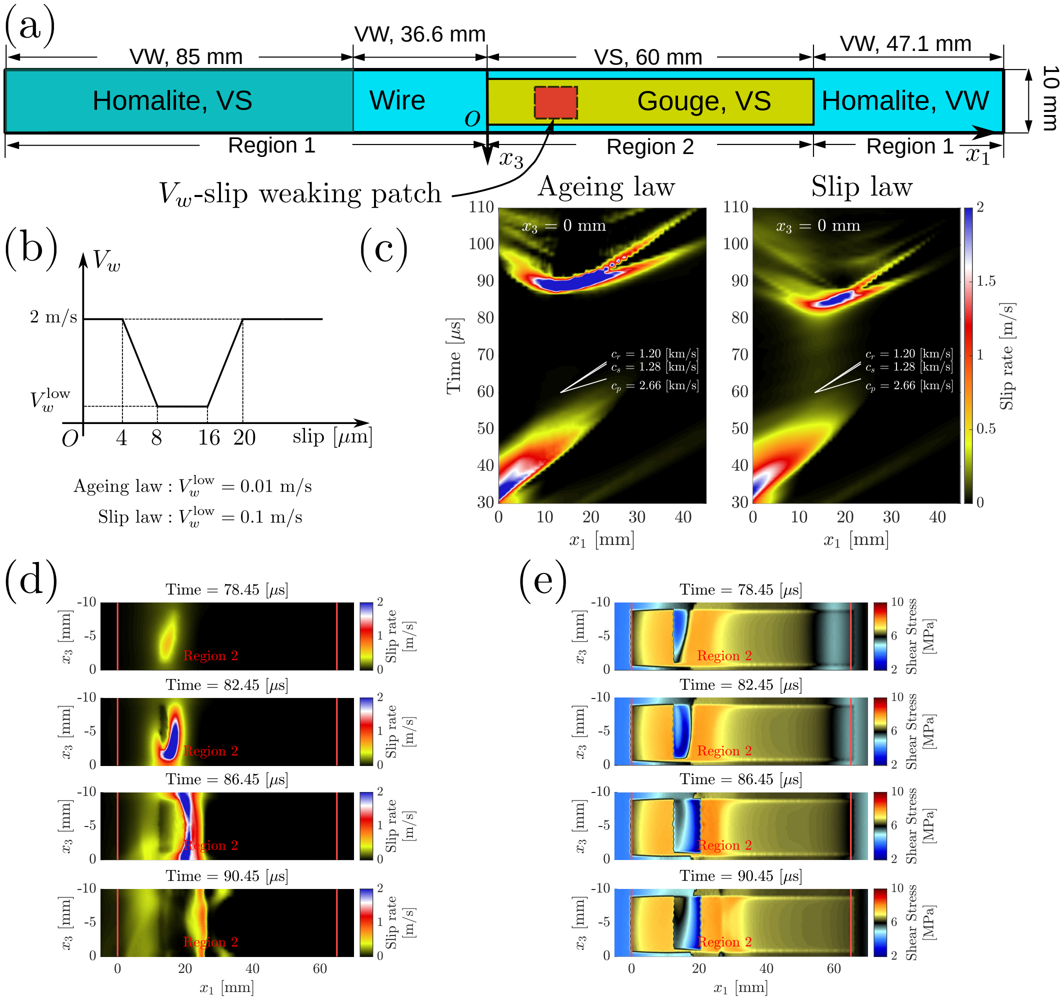

Figure 4.12: Self nucleation can be achieved by introducing a more efficient V_w-slip weakening patch within the gouge layer. We also eliminate the come-back rupture at 80 microseconds by modifying properties of the Homalite interface away from the gouge. (a) The Homalite section to the left of the wire is set to be velocity-strengthening, to impair slip there that causes a come-back rupture. A patch with variable flash-heating properties is put in the gouge zone, around $x_1 = 15$ mm, i.e., where the first ruptures get arrested. (b) The decrease and increase of V_w vs. slip in the patch is piecewise linear, going from values appropriate for gouge layer to values characteristic of bare surfaces. (c) The X-T diagrams of slip rate for cases without and with the slip-weakening patch. The case without the patch shows that the VS Homalite section is able to prevent the secondary rupture from entering the gouge zone at around 90 μs, while the case with the patch achieves self-nucleation by its more efficient weakening. (d) Snapshots of slip rate at the interface at $78.45, 82.45, 86.45, 90.45$ μs, for the case with the slip law, clearly showing the self-nucleation process and rupture arrest later. (e) Snapshots of shear stress at the interface at $78.45, 82.45, 86.45, 90.45$ μs, for the case with **slip law**. Shear stress first decreases in the patch and then recovers, due to the evolution of V_w with slip as in (b).

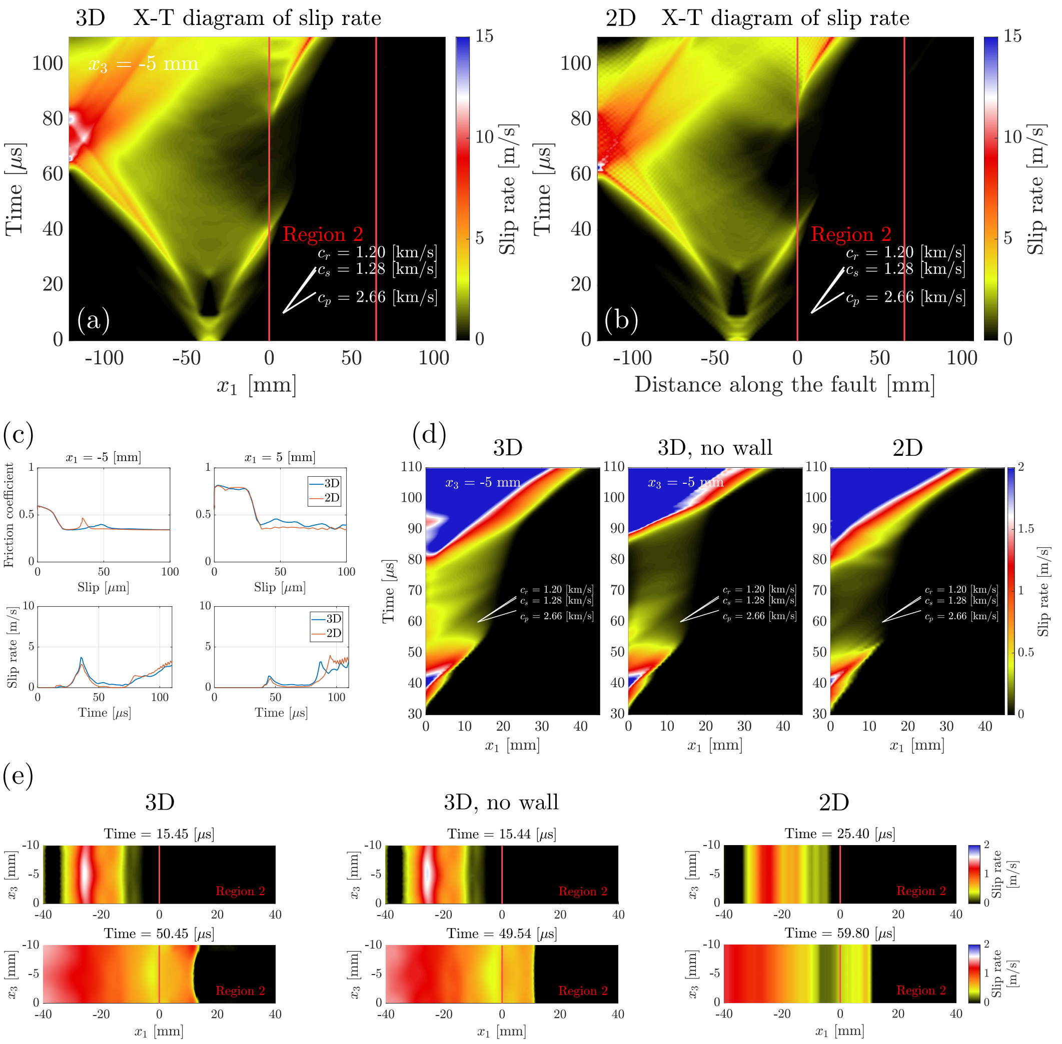

Figure 4.13: Comparison between 3D and 2D simulations with velocity-strengthening plus flash-heating gouge. (a-b) x_3-Time diagram of slip rates along the entire interface with $V_{initial} = 10^{-7}$ m/s with 3D and 2D simulations. Note that here the slip rate for the 3D simulations are plotted at $x_3 = -5$ mm. They look largely similar. (c) Friction vs. Slip and Slip rate vs. Time for 3D and 2D simulations at $x_1 = -5$ mm (in the Homalite) and $x_1 = -5$ mm (in the gouge). The friction coefficient is largely similar between 3D and 2D cases, while the 3D case has in general larger slip rate as the rupture first arrives. (d) x_3-Time diagram of slip rates in “Field of View" between 3D case, 3D with out the 1 mm Homalite wall surrounding the gouge in x_3 direction, and 2D case. We see that the first rupture becomes less and less profound. (e) Snapshots of slip rate over the interface between 3D case, 3D without the 1 mm Homalite wall surrounding the gouge in x_3 direction, and the 2D case. Notice that The shape of rupture front of the 3D case is the most convex, and then the 3D case without the wall is also convex. The 2D case has a straight rupture front. The 3D case without the 1 mm Homalite wall surrounding the gouge in x_3 direction already has a rupture with higher peak slip rate than the 2D case, because the rupture propagates more easily at the free surface. Then adding the Homalite surrounding in x_3 direction (the 3D case) further fosters higher slip rate, because the Homalite region has lower shear resistance.

4.4 Conclusions

In this study, we have developed a 3D dynamic finite element (FE) model for simulating dynamic rupture propagation in pre-existing fault interfaces embedded in elastic solid. We first implement a modified fault constitutive model with both rate-and-state friction and flash heating dynamic-weakening mechanism in the open source finite element software PyLith [2]. The friction formulation can be applied to non-planar fault interfaces within the finite element framework of PyLith, and also allows for heterogeneous friction properties along the fault, due to the nature of finite-element formulations. Then we apply our modeling capability to study a complicated lab experiment that has intermittent dynamic lab earthquakes on a non-homogeneous fault interface.

We find that velocity-strengthening fault gouge equipped with flash-heating dynamic weakening mechanism can first arrest the initial rupture as it arrives at the interface, and later allows for a second rupture to propagate in the gouge zone at dynamic slip rates. However, the typical formulation of flash-heating with uniform friction properties in the gouge cannot reproduce the self-nucleation at the specific spot observed in the experiment. By further introducing a patch of variable dynamic weakening at the specific spot, we are able to get a self-nucleated and then self-contained event. The variation in dynamic weakening corresponds to parameters changing from the ones appropriate to distributed sliding in gouge to the ones appropriate for localized slip on a surface, suggestion that the self-nucleating event could be due to shear-localization and then de-localization processes in the rock gouge. .

We also find that the rupture behavior depends on the initial slip rate of the interface, and the rupture becomes much less dynamic or even not cannot nucleate under the same explosion when the initial slip rate decreases from 10^{-7} m/s to 10^{-9} m/s. To further constrain future experiments and modeling, it would be important to conduct holding experiments before triggering the lab earthquakes ([27]) to measure the initial conditions over the fault.

Finally we compare 3D with 2D plane-stress simulations. The results show that 3D simulations have more dynamic ruptures and higher slip rates under the same explosion, due to free surfaces and Homalite wallaround the gouge zone in the 3D simulations. Also 3D simulations allow for non-uniform rupture front in the thickness direction, which is important for ruptures nucleating in the middle of the thickness direction. We conclude that 3D simulations are necessary to reproduce the full set of experimental observations and study the rupture behavior as well as nucleation processes in detail.

In the future, the FE model we have developed can be extended to study other complicated dynamic rupture propagation problems happening at pre-existing fault interfaces, to better understand the underlying physics of lab and natural earthquakes.

References

[1] B. Aagaard, M. Knepley, and C. Williams. *PyLith User Manual, Version 2.2.2*. http://www.geodynamics.org/cig/software/pylith/pylith_manual-2.2.2.pdf. Computational Infrastructure for Geodynamics (CIG). University of California, Davis, 2017.

[2] B. Aagaard, M. Knepley, and C. Williams. *PyLith v2.2.2*. Computational Infrastructure for Geodynamics (CIG). University of California, Davis, 2017. DOI: `10.5281/zenodo.886600`.

[3] B. T. Aagaard, M. G. Knepley, and C. A. Wiliams. “A domain decomposition approach to implementing fault slip in finite-element models of quasi-static and dynamic crustal deformation.” In: *Journal of Geophysical Research Solid Earth* 118 (2013), pp. 3059–3079. DOI: `10.1002/jgrb.50217`.

[4] N. Beeler, T. Tullis, and D. Goldsby. “Constitutive relationships and physical basis of fault strength due to flash heating.” In: *Journal of Geophysical Research-Solid Earth* 113.B1 (Jan. 2008). ISSN: 2169-9313. DOI: `10.1029/2007JB004988`.

[5] C. Boulton et al. “High-velocity frictional properties of Alpine Fault rocks: Mechanical data, microstructural analysis, and implications for rupture propagation.” In: *Journal of Structural Geology* 97 (Apr. 2017), pp. 71–92. ISSN: 0191-8141. DOI: `10.1016/j.jsg.2017.02.003`.

[6] K. Brown and Y. Fialko. “’Melt welt’ mechanism of extreme weakening of gabbro at seismic slip rates.” In: *Nature* 488.7413 (Aug. 2012), pp. 638–+. ISSN: 0028-0836. DOI: `10.1038/nature11370`.

[7] G. Di Toro, D. Goldsby, and T. Tullis. “Friction falls towards zero in quartz rock as slip velocity approaches seismic rates.” In: *Nature* 427.6973 (Jan. 2004), pp. 436–439. ISSN: 0028-0836. DOI: `10.1038/nature02249`.

[8] G. Di Toro et al. “Fault lubrication during earthquakes.” In: *Nature* 471.7339 (Mar. 2011), pp. 494–+. ISSN: 0028-0836. DOI: `10.1038/nature09838`.

[9] J. Dieterich. “Modeling of rock friction .1. experimental results and constitutive equations.” In: *Journal of Geophysical Research* 84.NB5 (1979), pp. 2161–2168. ISSN: 0148-0227. DOI: `10.1029/JB084iB05p02161`.

[10] D. Faulkner et al. “Stuck in the mud? Earthquake nucleation and propagation through accretionary forearcs.” In: *Geophysical Research Letters* 38 (Sept. 2011). ISSN: 0094-8276. DOI: `10.1029/2011GL048552`.

[11] D. Goldsby and T. Tullis. “Flash Heating Leads to Low Frictional Strength of Crustal Rocks at Earthquake Slip Rates.” In: *Science* 334.6053 (Oct. 2011), pp. 216–218. ISSN: 0036-8075. DOI: `10.1126/science.1207902`.

[12] Y. Kaneko, N. Lapusta, and J. Ampuero. “Spectral element modeling of spontaneous earthquake rupture on rate and state faults: Effect of velocity-strengthening friction at shallow depths.” In: *Journal of Geophysical Research-Solid Earth* 113.B9 (Sept. 2008). ISSN: 2169-9313. DOI: `10.1029/2007JB005553`.

[13] H. Kitajima, F. Chester, and J. Chester. “Dynamic weakening of gouge layers in high-speed shear experiments: Assessment of temperature-dependent friction, thermal pressurization, and flash heating.” In: *Journal of Geophysical Research-Solid Earth* 116 (Aug. 2011). ISSN: 2169-9313. DOI: `10.1029/2010JB007879`.

[14] X. Lu, N. Lapusta, and A. Rosakis. “Pulse-like and crack-like ruptures in experiments mimicking crustal earthquakes.” In: *Proceedings of the National Academy of Sciences of the United States of America* 104.48 (Nov. 2007), pp. 18931–18936. ISSN: 0027-8424. DOI: `10.1073/pnas.0704268104`.

[15] C. Marone. “Laboratory-derived friction laws and their application to seismic faulting.” In: *Annual Review of Earth and Planetary Sciences* 26 (1998), pp. 643–696. ISSN: 0084-6597. DOI: `10.1146/annurev.earth.26.1.643`.

[16] H. Noda, E. Dunham, and J. Rice. “Earthquake ruptures with thermal weakening and the operation of major faults at low overall stress levels.” In: *Journal of Geophysical Research-Solid Earth* 114 (July 2009). ISSN: 2169-9313. DOI: `10.1029/2008JB006143`.

[17] B. Proctor et al. “Dynamic weakening of serpentinite gouges and bare surfaces at seismic slip rates.” In: *Journal of Geophysical Research-Solid Earth* 119.11 (Nov. 2014), pp. 8107–8131. ISSN: 2169-9313. DOI: `10.1002/2014JB011057`.

[18] Z. Reches and D. Lockner. “Fault weakening and earthquake instability by powder lubrication.” In: *Nature* 467.7314 (Sept. 2010), 452–U102. ISSN: 0028-0836. DOI: `10.1038/nature09348`.

[19] J. Rice, N. Lapusta, and R. Kunnath. “Rate and state dependent friction and the stability of sliding between elastically deformable solids.” In: *Journal of the Mechanics and Physics of Solids* 49 (Sept. 2001), pp. 1865–1898. DOI: `10.1016/S0022-5096(01)00042-4`.

[20] J. Rice. “Heating and weakening of faults during earthquake slip.” In: *Journal of Geophysical Research-Solid Earth* 111.B5 (May 2006). ISSN: 2169-9313. DOI: `10.1029/2005JB004006`.

[21] J. Rice and A. Ruina. “Stability of steady friction slipping.” In: *Journal of Applied Mechanics-Transactions of the ASME* 50.2 (1983), pp. 343–349. ISSN: 0021-8936. DOI: `10.1115/1.3167042`.

[22] C. Rowe et al. “Earthquake lubrication and healing explained by amorphous nanosilica.” In: *Nature Communications* 10 (Jan. 2019). ISSN: 2041-1723. DOI: `10.1038/s41467-018-08238-y`.

[23] V. Rubino, A. Rosakis, and N. Lapusta. “Understanding dynamic friction through spontaneously evolving laboratory earthquakes.” In: *Nature Communcations* 8 (June 2017). ISSN: 2041-1723. DOI: `10.1038/ncomms15991`.

[24] V. Rubino, N. Lapusta, and A. J. Rosakis. “Intermittent lab earthquakes in dynamically weakening fault gouge.” In: *Nature* 606.7916 (June 2022), pp. 922–929. DOI: `10.1038/s41586-022-04749-3`.

[25] A. Ruina. “Slip instability and state variable friction laws.” In: *Journal of Geophysical Research* 88.NB12 (1983), pp. 359–370. ISSN: 0148-0227. DOI: `10.1029/JB088iB12p10359`.

[26] C. H. Scholz. *The Mechanics of Earthquakes and Faulting*. 3rd ed. Cambridge University Press, 2019. DOI: `10.1017/9781316681473`.

[27] K. Sirorattanakul et al. “Sliding and healing of frictional interfaces that appear stationary.” In: *In revision for Nature* (2024).

[28] Y. Tal et al. “Illuminating the physics of dynamic friction through laboratory earthquakes on thrust faults.” In: *Proceedings of the National Academy of Sciences* 117.35 (2020), pp. 21095–21100. DOI: `10.1073/pnas.2004590117`.

[29] W. Tanikawa and T. Shimamoto. “Frictional and transport properties of the Chelungpu fault from shallow borehole data and their correlation with seismic behavior during the 1999 Chi-Chi earthquake.” In: *Journal of Geophysical Research-Solid Earth* 114 (Jan. 2009). ISSN: 2169-9313. DOI: `10.1029/2008JB005750`.

[30] A. Tsutsumi and T. Shimamoto. “High-velocity frictional properties of gabbro.” In: *Geophysical Research Letters* 24.6 (Mar. 1997), pp. 699–702. ISSN: 0094-8276. DOI: `10.1029/97GL00503`.

[31] K. Xia, A. Rosakis, and H. Kanamori. “Laboratory earthquakes: The sub-Rayleigh-to-supershear rupture transition.” In: *Science* 303.5665 (Mar. 2004), pp. 1859–1861. ISSN: 0036-8075. DOI: `10.1126/science.1094022`.

Chapter 5

LEARNING A POTENTIAL FORMULATION FOR RATE-AND-STATE FRICTION WITH RECURRENT NEURAL OPERATORS (RNOS)

5.1 Introduction

In this study, we adopt the Coulomb friction formulation, where the shear traction τ over a point of a frictional interface X is related to the applied normal traction σ through friction coefficient f. The friction coefficient, in a general setting, would depend on the slip history of that location $\{x(X,t') : t' \in [0,t]\}$, i.e.,

$$\tau(t,X) = \sigma(t,X) f\left(\{x(X,t') : t' \in [0,t]\}\right). \tag{5.1}$$

Rate-and-state friction

Building on the general friction formulation given by (5.1), rate-and-state friction further assumes that the dependency on slip history $\{x(X,t') : t' \in [0,t]\}$ is restricted to dependencies on the current slip rate, $V = \dot{x}(X,t)$ and a state variable $\theta(X,t)$. Inspired by experimental observations [4, 7, 10], rate-and-state friction law postulates that the friction coefficient

$$f^{RS}(X,t) = f_* + a\log\left(\frac{V(X,t)}{V_*}\right) + b\log\left(\frac{V_*\theta(X,t)}{D_{RS}}\right), \tag{5.2}$$

where f_* is reference friction coefficient, V_* is reference slip rate, D_{RS} is characteristic slip distance and a, b are dimensionless rate-and-state parameters, and θ is a state variable that evolves with time. The evolution of θ is given by the Dieterich ageing law [4, 10]:

$$\theta(X,t) = 1 - \frac{V(X,t)\theta(X,t)}{D_{RS}}. \tag{5.3}$$

Since the formulation of rate-and-state friction only has local dependency on X, i.e., no ∇X involved, the computation of f_{RS} is local and point-wise, and thus usually X is omitted without ambiguity. Further, at steady state ($\dot{\theta} = \dot{V} = 0$), one can further get

$$f_{ss}^{RS} = f_* + (a-b)\log\left(\frac{V_{ss}}{V_*}\right). \tag{5.4}$$

If $a - b > 0$, steady rate-and-state friction coefficient f^{RS} increases as slip rate increase, and the friction is rate-strengthening. If $a - b < 0$, the friction is rate-weakening. Rate-weakening rate-and-state friction has been widely applied to the modeling of dynamic earthquakes, since it can potentially be unstable under perturbations in slip rate [4, 7, 10, 9, 11].

It can be checked that there is no potential associated with the original rate-and-state formulation, i.e., we cannot find scalar potential functions whose gradients would yield both the friction coefficient f^{RS} and the evolution law of θ. This property raises challenges in numerically solving dynamic boundary value problems with rate-and-state friction law. While if the friction formulation has associated potentials, the implicit solving process will be equivalent to a minimization problem, which can be easier and more robust to solve implicitly. The goal of this study is thus to find a friction law with a potential that not only has similar rate-and-state behaviors, but also facilitates the fast and stable numerical solution of dynamic friction problems in application.

5.2 Formulation

Following the formulation of general history-dependent given by (5.1), we still further assume that the dependence on the slip history can be modeled as dependence on hidden variables $\boldsymbol{\xi} \in \mathbb{R}^d$. We introduce three potentials, $W(x)$, $D^\dagger(\dot{x}, \boldsymbol{\xi})$ and $D(\dot{\boldsymbol{\xi}})$, whose derivatives give rise to the friction coefficient and evolution law of $\boldsymbol{\xi}$, i.e.,

$$f^P(\dot{x}, \boldsymbol{\xi}) = \frac{dW}{dx}(x) + \frac{\partial D^\dagger}{\partial \dot{x}}(\dot{x}, \boldsymbol{\xi}), \tag{5.5}$$

$$\frac{dD}{d\dot{\boldsymbol{\xi}}}(\dot{\boldsymbol{\xi}}) + \frac{\partial D^\dagger}{\partial \boldsymbol{\xi}}(\dot{x}, \boldsymbol{\xi}) = 0, \tag{5.6}$$

where f^P is the potential formulation friction coefficient. x is local slip and $V = \dot{x}$ is local slip rate, $\boldsymbol{\xi} \in \mathbb{R}$ is a d dimensional vector of internal variables that encodes the local slip history.

The advantage of this potential formulation is that the solution of an incremental problem with such friction are equivalent to the stationary point of a scalar function $J(x, \boldsymbol{\xi})$. Take an example of the spring slider configuration under displacement-control as shown in Figure 5.1. The system is driven by prescribing $x_p(t)$, and the force of the spring is linearly dependent on its elongation with spring constant k. There is history-dependent friction between the mass block and the ground, gravity

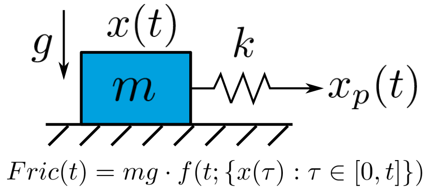

Figure 5.1: Example: spring slider under displacement-control driving force.

acceleration is g. Assuming that the history-dependent friction can be represented in the above potential form, the equations of motion of the system is

$$\begin{aligned} m\ddot{x} - k(x_p(t) - x(t)) + mg\left(\frac{dW}{dx} + \frac{\partial D^\dagger}{\partial \dot{x}}\right) &= 0 \\ \frac{dD}{d\dot{\boldsymbol{\xi}}}(\dot{\boldsymbol{\xi}}) + \frac{\partial D^\dagger}{\partial \boldsymbol{\xi}}(\dot{x}, \boldsymbol{\xi}) &= 0. \end{aligned} \tag{5.7}$$

Given the solution at current time $x_n, \boldsymbol{\xi}_n$, and the time increment $\Delta t = t_{n+1} - t_n$, define

$$E^{sp}(x) = \frac{1}{2}\left(x(t) - x_p(t)\right)^2 \tag{5.8}$$

$$E^{in}(x) = \frac{1}{2}\left(\frac{x - 2x_n + x_{n-1}}{\Delta t}\right)^2, \tag{5.9}$$

as the spring potential and the inertia potential, and

$$J(x, \boldsymbol{\xi}; \Delta t, x_n, \boldsymbol{\xi}_n) = E^{sp}(x) + E^{in}(x) + W(x) + \Delta t D^\dagger\left(\frac{x - x_n}{\Delta t}, \boldsymbol{\xi}\right) + \Delta t^2 D\left(\frac{\boldsymbol{\xi} - \boldsymbol{\xi}_n}{\Delta t}\right) \tag{5.10}$$

as the system potential. Then it is straight-forward too see that the backward Euler implicit update is

$$x_{n+1}, \boldsymbol{\xi}_{n+1} = \arg\min_{x,\boldsymbol{\xi}} J(x, \boldsymbol{\xi}; \Delta t, x_n, \boldsymbol{\xi}_n). \tag{5.11}$$

This is well-posed if J is convex in $(x, \boldsymbol{\xi})$. Convexity of J is trivial if $W, D^\dagger, D$ are all convex in $(x, \boldsymbol{\xi})$. However, usually not all of $W, D^\dagger, D$ are convex, especially $D^\dagger$, since if friction coefficient decreases with slip rate, i.e.,

$$\frac{\partial f}{\partial \dot{x}} = \frac{\partial^2 D^\dagger}{\partial \dot{x}^2} < 0. \tag{5.12}$$

In such cases, one needs to adjust Δt such that E^{in} dominates and J is convex.

In summary, by developing such a potential formulated friction, the implicit solving process of dynamic problems are turned into a convex optimization problem, which would guarantee us the existence of a unique solution for $(x_{n+1}, \boldsymbol{\xi}_{n+1})$. This would facilitate implicit solution which is usually difficult with the original rate-and-state friction. Since the original rate-and-state friction given by (5.2) is able to fit experimental data well with 4 parameters, it is crucial to verify that the potential-formulated friction specified by (5.5) can replicate rate-and-state friction sequences, with some selected $W, D^\dagger$ and D.

In practice, it is useful to work with the dual formulation. Let $D^*(\dot{\boldsymbol{d}})$ be the Legendre transform of $D(\dot{\boldsymbol{\xi}})$,

$$D^*\left(\dot{\boldsymbol{d}}\right) = \sup_{\dot{\boldsymbol{\xi}} \in \mathbb{R}^d} \left\{ \left\langle \dot{\boldsymbol{d}}, \dot{\boldsymbol{\xi}} \right\rangle - D(\dot{\boldsymbol{\xi}}) \right\}. \tag{5.13}$$

The advantage of using D^* instead of D is that instead of solving the non-linear equation for $\dot{\boldsymbol{\xi}}$ given by (5.6), it is equivalent to computing $\dot{\boldsymbol{\xi}}$ by

$$\dot{\boldsymbol{\xi}} = \frac{d\tilde{D}^*}{d\dot{\boldsymbol{d}}} \left(-\frac{\partial \tilde{D}^\dagger}{\partial \boldsymbol{\xi}} \right), \tag{5.14}$$

if $D\left(\dot{\boldsymbol{\xi}}\right)$ is convex in $\dot{\boldsymbol{\xi}}$.

5.3 Neural Network and training

We use Neural Networks to approximate the above potentials within the deeping learning environment PyTorch [8], i.e.,

$$W(x) \approx W_{NN}(x; w_W), D^\dagger(\dot{x}, \boldsymbol{\xi}) \approx D^\dagger_{NN}(\dot{x}, \boldsymbol{\xi}; w_{D^\dagger}), D^*\left(\dot{\boldsymbol{d}}\right) \approx D^*_{NN}\left(\dot{\boldsymbol{d}}, w_{D^*}\right), \tag{5.15}$$

and we call the resulting architecture a Recurrent Neural Operator (RNO) following [6, 2].

To find proper $W, D^\dagger$ and D that give f^{NN} similar enough to f^{RS} under a set of rate-and-state parameters, we generate a synthetic dataset of f^{RS}'s by prescribing the slip histories $\{V = \dot{x}(t) : t \in [0, T]\}$. We then fit f^{NN}'s to f^{RS}'s by optimizing over the parameters of $W_{NN}, D^\dagger_{NN}$ and D_{NN}, as shown in Figure 5.2. And the loss function we use for training of the potentials is relative L_p error, i.e.,

$$w^*_W, w^*_{D^\dagger}, w^*_D = \arg\min_{w_W, w_{D^\dagger}, w_D} \frac{1}{N} \sum_{i=1}^{N} \frac{\|f_i^{NN}(t) - f_i^{RS}(t)\|_{L_p}}{\|f_i^{RS}(t)\|_{L_p}}. \tag{5.16}$$

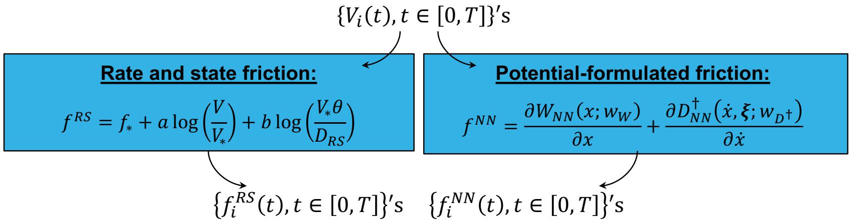

Figure 5.2: Training of W, $D^\dagger$ and D through fitting f^{NN} to f^{RS}.

In this study, the rate-and-state friction parameters are chosen to be

$$\begin{aligned} a &= 0.011, \\ b &= 0.016, \\ V_* &= 1 \times 10^{-6} \text{ m/s}, \\ D_{RS} &= 1 \times 10^{-8} \text{ m}, \\ f_* &= 0.5109, \end{aligned}$$

such that we do examine the ability of potential formulated friction to fit rate-weakening ($a - b < 0$) rate-and-state friction, which is more challenging to solve numerically. Regarding the specific choices of $V_i(t)$'s, we take inspiration from both velocity jump tests for rate-and-state friction [10], as well as continuous variation sequences from the previous studies of RNO [6, 2]. For the velocity jump sequences, $V_i(t)$'s are simple functions, i.e., the sum of a finite number of Heaviside functions, as shown by the first example in Figure 5.3. Note that the prescribed velocity jumps have to be on the log scale to cause significant changes in f^{RS}. While for the continuous variation sequences, $V_i(t)$'s vary continuously with t and change their monotonicity at randomly-sampled times, as shown by the second example in Figure 5.3. The range of prescribed $V_i(t)$'s is set such that $V_i(t)/V_* \in [10^{-3}, 10^{1}]$ for both types of sequences. For easier plotting of displacements, we define

$$D_* = V_* \cdot 1 \text{ s} = 1 \times 10^{-6} \text{ m}.$$

Within the training process, we apply Optuna [1] optimization package for hyper-parameter tuning of the Recurrent Neural Operators (RNO). Those hyper-parameters include learning rate, depth of the Neural Network, number of neurons within each layer, p value for the L_p norm, as well as the batch size in the training dataset. Detailed algorithm regarding the training process can be found in Algorithm 1.

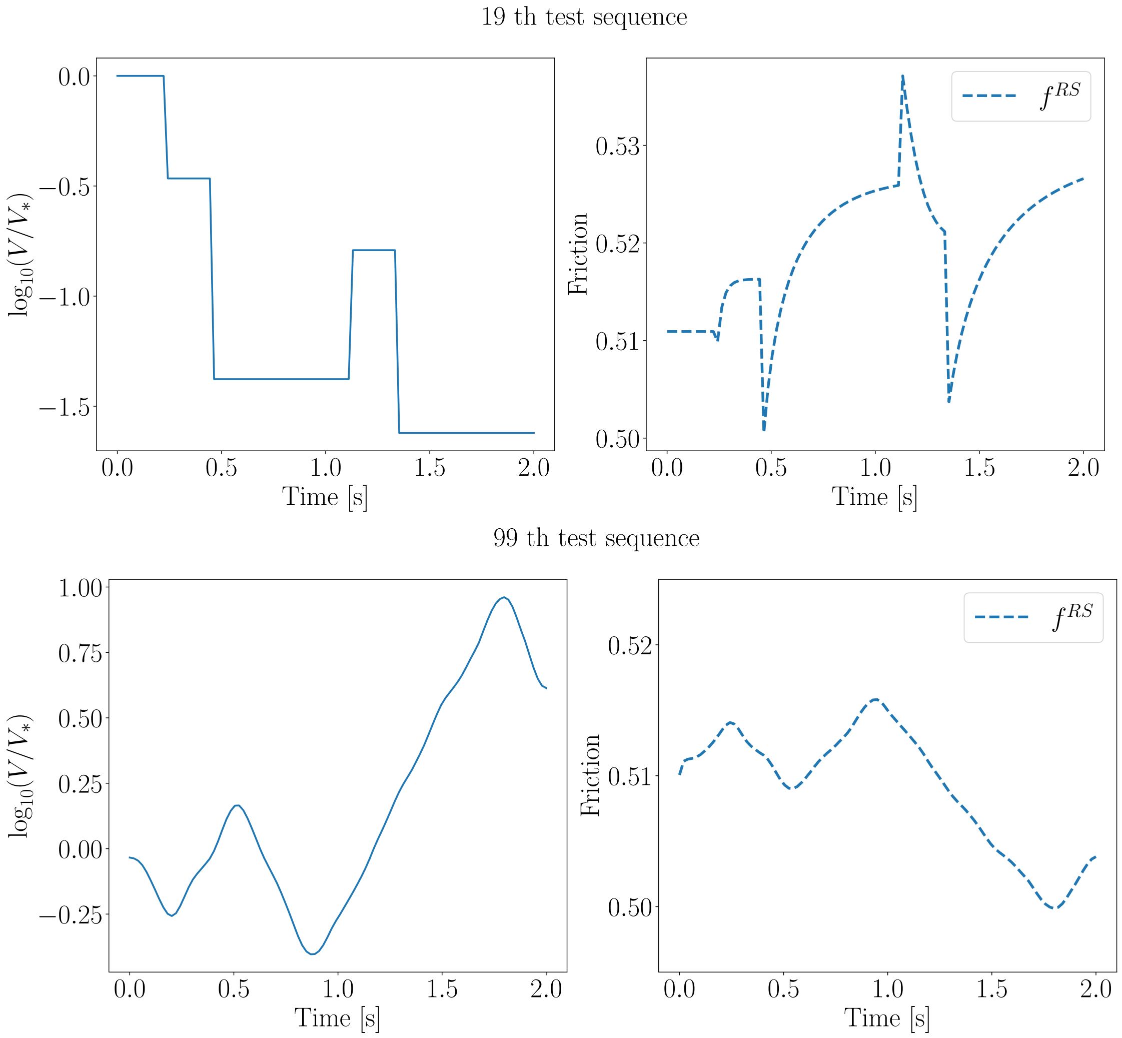

Figure 5.3: Examples of velocity jump $V_i(t)$ (upper, sequence 19), continuous variation $V_i(t)$ (lower, sequence 99) and their corresponding f^{RS}s in the synthetic dataset.

Algorithm 1 Training $W_{NN}(x; w_W)$, $D^{\dagger}_{NN}(\dot{x}, \boldsymbol{\xi}; w_{D^{\dagger}})$ and $D^{*}_{NN}(\dot{\boldsymbol{d}}; w_D)$

```
Require: training sequences $\left\{\dot{x}_i = V_i(t), f_i^{RS}(t) : t \in [0, T]\right\}_{i=0}^{N}$.
Require: $N_{epochs}$
  $epoch = 0$
  while $epoch < N_{epochs}$ do
      for $i \in \{0, 1, \dots, N\}$ do            ▷ In practical sequences are passed in batches.
          Fix $w_W, w_{D^{\dagger}}, w_D$
          for $n = 1, 2, \dots, N^{(i)}$ do         ▷ $N^{(i)}$ is number of time steps of sequence $i$.
              $\xi_n \leftarrow \xi_{n-1} + (t_n - t_{n-1})\dot{\boldsymbol{\xi}}_{n-1}$
              $f_n^{NN} \leftarrow \frac{\partial W_{NN}}{\partial x}(x_n) + \frac{\partial D^{\dagger}_{N}N}{\partial \dot{x}}(\dot{x}_n, \boldsymbol{\xi}_n)$
              $\dot{\boldsymbol{\xi}}_n \leftarrow$ solution of $\frac{dD_{NN}}{d\dot{\boldsymbol{\xi}}}(\dot{\boldsymbol{\xi}}) + \frac{\partial D^{\dagger}_{NN}}{\partial \boldsymbol{\xi}}(\dot{x}_n, \boldsymbol{\xi}_n) = 0$      ▷ In practical
  $\dot{\boldsymbol{\xi}}_n = \frac{dD^{*}_{NN}}{d\dot{\boldsymbol{d}}}\left(-\frac{\partial D^{\dagger}_{NN}}{\partial \boldsymbol{\xi}}(\dot{x}_n, \boldsymbol{\xi}_n)\right)$
          end for
          Compute Loss $L(w_W, w_{D^{\dagger}}, w_D) = \|f^{RS} - f^{NN}(w_W, w_{D^{\dagger}}, w_D)\|_{L^p} / \|f^{RS}\|_{L^p}$
          Update $w_W, w_{D^{\dagger}}, w_D$ based on the gradient of $L$ w.r.t. $w_W, w_{D^{\dagger}}, w_D$
      end for
      $epoch \leftarrow epoch + 1$
  end while
```

5.4 Results and discussion

In this section, we present how well the proposed RNO based potential formulated friction can fit the original rate-and-state friction, and also whether or not it facilitates implicit solution of dynamic problems through solving the spring slider example.

Fitting results to original rate-and-state friction

After 100 epochs of training under the optimal Neural Network structure given by OPTUNA, the RNO potentials are able to fit the original rate-and-state sequences well. Figure 5.4 shows the fitting results of the two example sequences early mentioned in Figure 5.3. Note that these two sequences are in the test dataset and have not been used for training the potentials. After training of the potentials $W_{NN}, D^{\dagger}_{NN}$ and D^{*}_{NN}, we can obtain f^{NN}s that are fairly close to f^{RS}s. Table 5.1 confirms that the error between f^{NN} and f^{RS} is small, and that there needs to be at least 1 hidden variable ($\dim(\boldsymbol{\xi})$) to achieve small error. Since further increasing the number of hidden variables does not reduce the error, the results shown next are all based on $\dim(\boldsymbol{\xi}) = 1$. The fact that it suffices to use $\dim(\boldsymbol{\xi}) = 1$ makes intuitive sense since the original rate-and-state friction has only one state variable θ.

Due to limited access to experimental data with the same rate-and-state friction properties, we cannot compare the error of f^{RS} and f^{NN} both fitted to experimental sequences f^{EXP}. We here include a typical rate-and-state fitted experimental sequence from (Kim et al., in preparation, 2024), which is shown by Figure 5.5. The best fit rate-and-state sequence achieves an relative L_2 error of 0.0015, which is two orders of magnitude higher than the average relative L_2 of fitting f^{NN} to f^{RS}. This implies that the fitting error between f^{NN} and f^{RS} is negligible compared with fitting f^{RS} to noisier f^{EXP}, and thus f^{NN} has comparable ability to explain the history dependencies in the empirical observations.

$\dim(\boldsymbol{\xi})$	0	1	2
Training error (L_2)	0.18 ± 0.01	0.0004 ± 0.0004	0.0007 ± 0.0006
Testing error (L_2)	0.18 ± 0.01	0.0005 ± 0.0004	0.0007 ± 0.0006

Table 5.1: Training and testing relative L_2 error for $\dim(\boldsymbol{\xi}) = 0, 1, 2$, averaged over 160 test sequences. Error decreases significantly after introducing one hidden variable $\dim(\boldsymbol{\xi}) = 1$, while introducing more hidden variables do not further reduce the error.

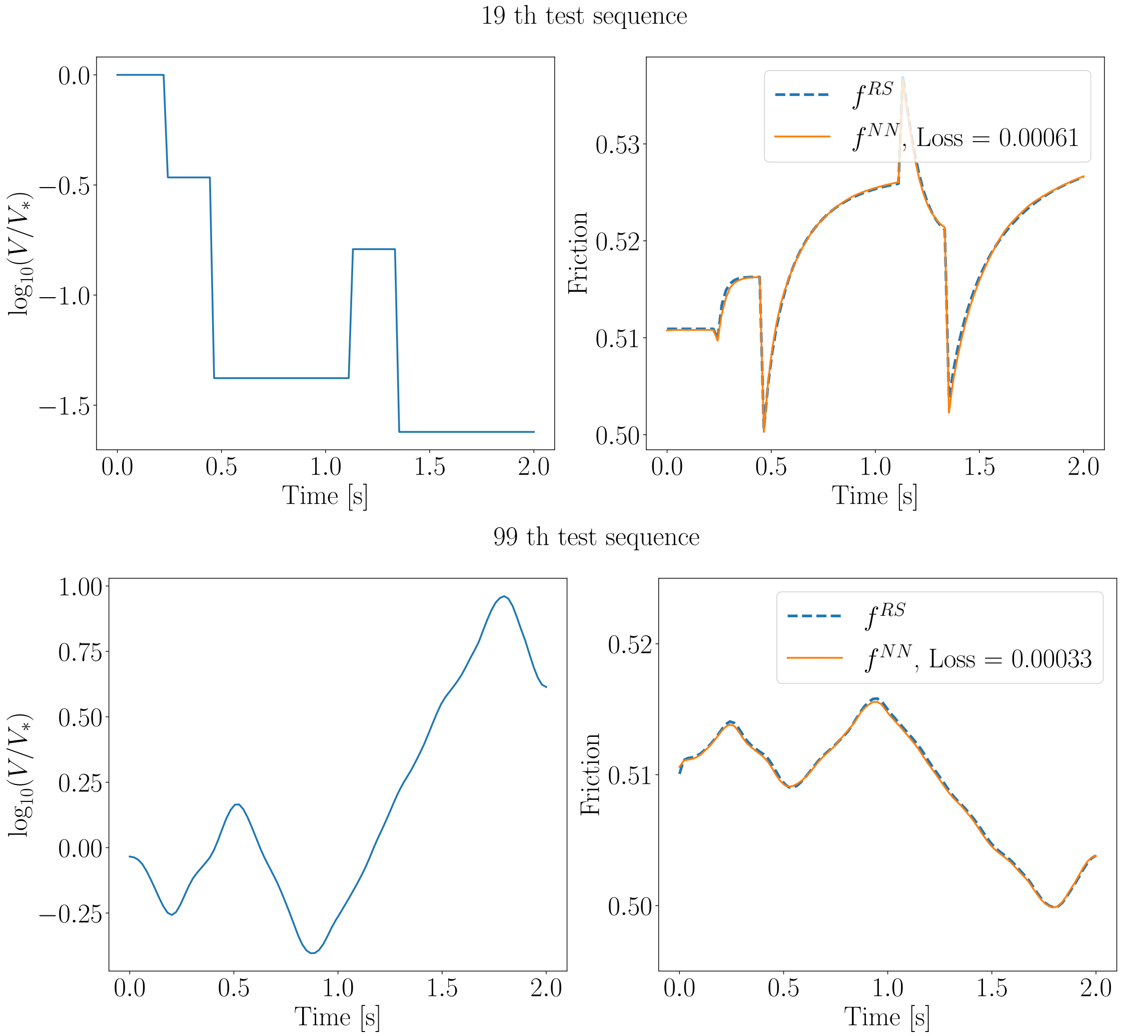

19 th test sequence

99 th test sequence

Figure 5.4: Examples of trained f^{NN} vs. f^{RS} for both velocity jump (upper) and continuous variation (lower) sequences. Loss here refers to relative L_2 error as defined by (5.16). These two sequences are from the test dataset and are not used for training the potentials.

The trained potentials $W, D^\dagger$ and D^*

To make (5.11) a convex minimization problem, we need to confirm convexity of J in (x, ξ). Figure 5.6 shows that the learnt W is linear in x, and thus also convex. The fact that W is linear makes sense because of material frame indifference. D^* is convex in $\dot{d}$, which is consistent with its definition as the Legendre transform of D. Figure 5.7 plots $D^\dagger(\dot{x}, \xi)$, and it is not convex because $\partial^2 D^\dagger / \partial \dot{x}^2 < 0$. To ensure convexity of J in (x, ξ), we need the Hessian of J to be positive semi-definite for all

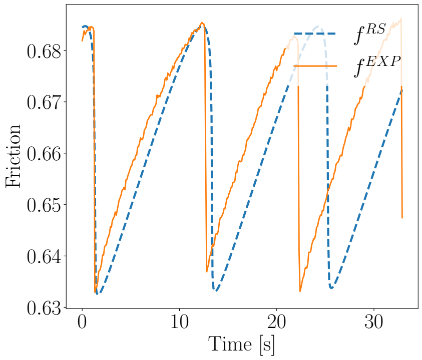

Figure 5.5: A typical fit of rate-and-state friction to experimental data, the relative L_2 error of f^{RS} against f^{EXP} is 0.0015. Data provided by Taeho Kim.

(x, ξ), which ends up posing a constraint on Δt:

$$1 \cdot m + \Delta t \left(\frac{\partial^2 D^\dagger}{\partial \dot{x}^2} \right) + O(\Delta t^2) \geq 0, \tag{5.17}$$

$$\begin{aligned} &1 \cdot m \frac{d^2 D}{d\dot{\xi}^2} + \Delta t \left(\frac{\partial^2 D^\dagger}{\partial \dot{x}^2} \frac{d^2 D}{d\dot{\xi}^2} + m \frac{\partial^2 D^\dagger}{\partial \xi^2} \right) \\ &+ \Delta t^2 \left[\left(k + \frac{d^2 W}{dx^2} \right) \frac{d^2 D}{d\dot{\xi}^2} + \frac{\partial^2 D^\dagger}{\partial \dot{x}^2} \frac{\partial^2 D^\dagger}{\partial \xi^2} - \frac{\partial^2 D^\dagger}{\partial \dot{x} \partial \xi} \right] \\ &+ \Delta t^3 \left[\left(k + \frac{d^2 W}{dx^2} \right) \frac{\partial^2 D^\dagger}{\partial \xi^2} \right] \geq 0. \end{aligned} \tag{5.18}$$

Equation (5.17) can be satisfied with Δt smaller than an upper bound, since then the m term will dominate even if $\partial^2 D^\dagger / \partial \dot{x}^2 < 0$. (5.18) also reduces to an upper bound constraint on Δt, since $d^2 D / d\dot{\xi}^2 > 0$ based on the assumption. In practical it is also convex because it is the Legendre transform of the learnt $D^*(\dot{d})$.

In summary, we find that of the three learnt potentials, W is linear in x, consistent with material-frame indifference; D^* is convex in $\dot{d}$, consistent with its definition by Legendre transform; while $D^\dagger$ is not convex in $(\dot{x}, \xi)$. However, one can still achieve convexity of $J(x, \xi)$ in (5.10) with an upper bound constraint on Δt, and thus it is legitimate to write (5.11) as a convex minimization problem.

Uniqueness of the hidden variable ξ

One important property of the hidden variable ξ is that since we cannot attach a concrete physical meaning to it, it is possibly non-unique. In practice, even different training runs can possibly lead to different ξ's that all fit the training dataset well. However, in our potential formulation an underlying assumption is that D is only a

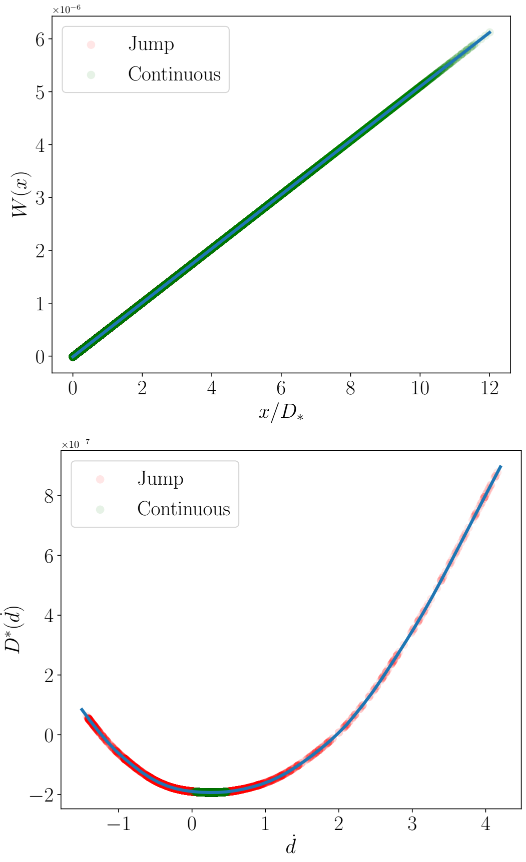

Figure 5.6: Learned $W(x)$ (left) and $D^*(\dot{d})$ (right). W is linear in x corresponding to the reference friction coefficient, D^* is convex, which complies with the definition as the Legendre transform of D.

function of $\dot{\xi}$. Then if there exists $\eta = f(\xi)$ as a different hidden variable with f and f^{-1} being smooth, we have

$$D^{\eta}\left(\dot{\eta}\right) = D^{\eta}\left(f'(\xi)\dot{\xi}\right) = D^{\xi}\left(\dot{\xi}\right), \tag{5.19}$$

which implies that $f'(\xi)$ is a constant, and thus ξ is unique up to affine transformations.

We verify the above-discussed uniqueness of ξ by training three different models on three datasets generated similarly using the same rate-and-state friction model. Then we obtain the trajectories of ξs of the three trained model on the same test dataset. After performing linear regression of $\xi^{(3)}$ and $\xi^{(2)}$s on $\xi^{(1)}$, i.e. the hidden variable from the first trained model, we check their regression coefficient as a reflection of how linearly correlated the ξs are.

Figure 5.8 shows that the regression coefficient is > 0.98 and thus the different ξs

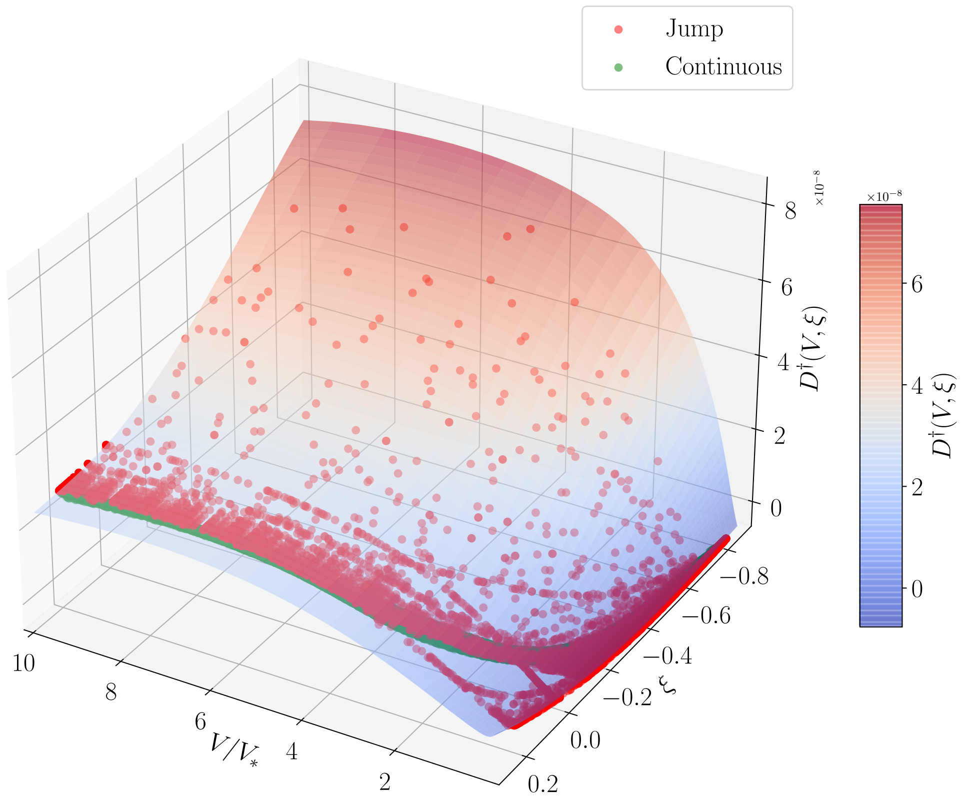

Figure 5.7: Learned $D^\dagger(\dot{x}, \boldsymbol{\xi})$, $D^\dagger$ is not convex in $(\dot{x}, \xi)$. The red dots show the trajectories of velocity-jump dataset, while the green dots show the trajectories of continuous variation dataset.

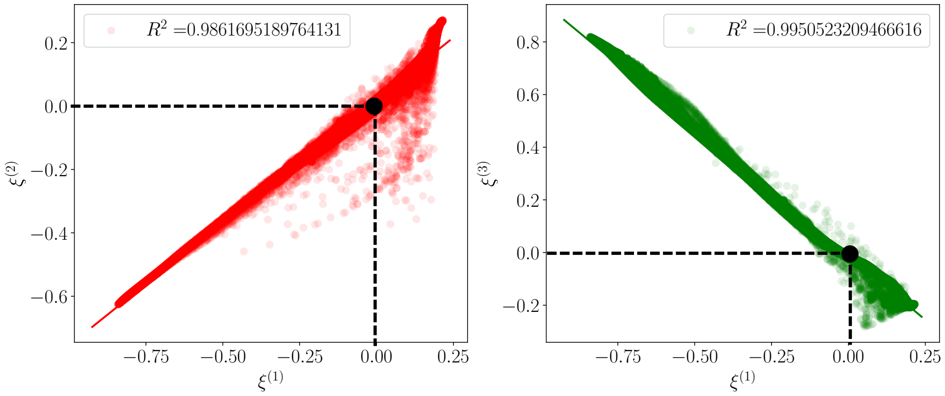

Figure 5.8: Linear regression of $\xi^{(3)}$ and $\xi^{(2)}$s on $\xi^{(1)}$. Red and green dots are the data points while the solid lines are the regression result. $(0, 0)$ should be a fixed point since all sequences start with $\xi = 0$ as their initial condition.

are indeed unique up to linear transform.

Example: solving spring slider under displacement control loading

As stated above, the potential formulated friction should facilitate implicit solution of dynamic initial value problems, because advancing the solution to the next time step can be written as a convex minimization problem given by (5.11). Here we try to verify that by considering the spring-slider problem with displacement-control loading. As shown by Figure 5.1, friction between the mass block and the ground is modeled with either original rate-and-state friction or trained potentials with the same rate-and-state properties. We testify the two friction formulations with both explicit (4th order Runge Kutta) and implicit (Adams) solvers trying to solve the same spring-slider problem. The solvers are imported from a standard ODE solver package torchdiffeq [3]. Spring constant k is randomly sampled within a range that covers both $k < k_{crit}$ and $k > k_{crit}$, where k_{crit} is the critical stiffness for unstable stick-slip events to happen under constant loading speed $\dot{x}_p(t)$ [9, 5]. and we create a dataset of 77 loading sequences with different velocity-jump-like $x_p(t)$s.

We first notice that since the training dataset of the potentials does not include these spring-slider sequences of $V(t), f(t)$, the error between the potential friction and the original rate-and-state friction is large. To resolve this, we generate 200 sequences from solving the spring-slider problem with rate-and-state friction and different loadings, and further train our potentials on these 200 sequences for 400 epochs. Indeed the further-trained NN potentials (denoted as NN') reduce the error between $f^{NN'}$ and f^{RS} when solving spring-slider sequences.

Table 5.2 shows that after further training the potentials on spring-slider solutions by rate-and-state friction, the relative L_2 error on $x(t), \dot{x}(t), f(t)$ decreases by more than 50%. Figure 5.9 plots an example spring-slider sequence. It is clear that further trained NN' agrees better with the solution obtained by the original rate-and-state friction. Another example sequence is shown by Figure D.1. The results and discussions next will all be based on the solution of NN'.

The potential formulated friction is that it can solve all the sequences, with either explicit or implicit solver. In contrast the original rate-and-state friction fails to solve over 60% of the sequences at even the finest Δt with the implicit solver, and over 40% with the explicit solver. Table 5.3 lists the ratio of sequences that cannot be solved by each (NN/RS, ex/implicit) pair.

The fact that rate-and-state friction does not converge with the implicit solver is

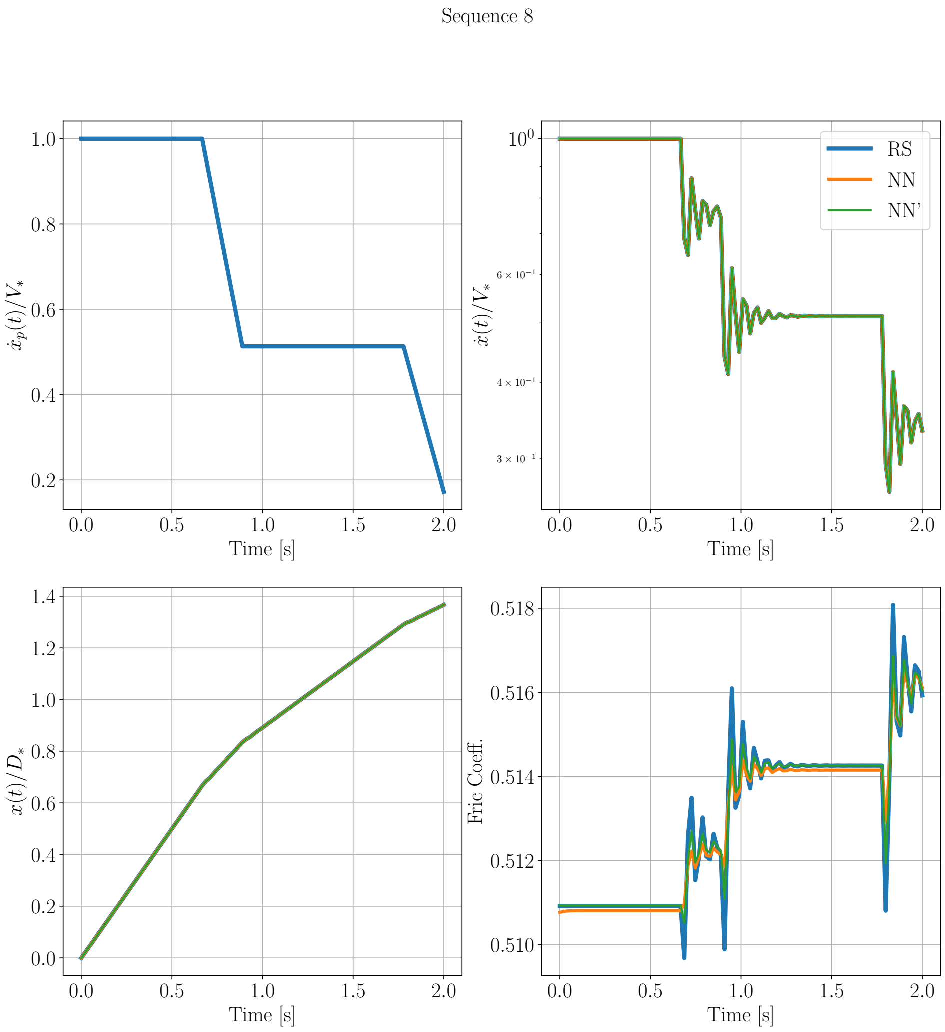
Sequence 8

Figure 5.9: An example sequence of spring-slider solution with original rate-and-state friction, NN potentials, and NN potentials further trained on spring-slider sequences

Solution term	NN	NN’
$x(t)$	$(1.9 \pm 1.8) \times 10^{-5}$	$(5.4 \pm 4.4) \times 10^{-6}$
$\dot{x}(t)$	$(2.7 \pm 3.6) \times 10^{-4}$	$(1.6 \pm 2.2) \times 10^{-4}$
$f(t)$	0.030 ± 0.024	0.016 ± 0.016

Table 5.2: Testing relative L_2 error for the original potentials only trained on velocity-jump and continuous variation dataset (NN), updated potentials further trained on 200 spring-slider like dataset (NN’). averaged over 10 test spring-slider sequences.

non-surprising given that it does not have an associated energy formulation. The fact that the potential formulated friction works well with the implicit solver is

Δt [s]	$2^{-13.5}$	$2^{-13.0}$	$2^{-12.5}$	$2^{-12.0}$	$2^{-11.5}$	$2^{-11.0}$
NN, implicit	0.000	0.000	0.000	0.000	0.000	0.000
NN, explicit	0.000	0.000	0.000	0.000	0.000	0.000
RS, implicit	0.506	0.571	0.623	0.623	0.675	0.727
RS, explicit	0.455	0.455	0.455	0.455	0.455	0.455

Table 5.3: Ratio of sequences that cannot be solved by NN, RS models with implicit, explicit solvers.

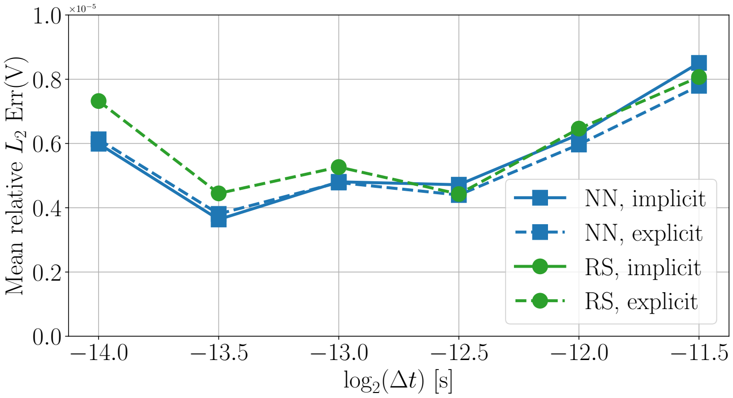

Figure 5.10: Growth of relative L_2 error in $\dot{x}(t)$ as Δt increases. Note that since (RS, implicit) cannot solve some of the sequences that the other three pairs can solve, its error is not plotted here.

consistent with (5.11) being a convex minimization problem.

Next, we check the growth of error as Δt increases for those sequences that (NN, implicit), (NN, explicit) and (RS, explicit) can all solve. Since we do not have analytical solutions for the sequences, Error is computed against the solve with the finest $\delta t = 2^{-14}$ s, for each (model, ex/implicit) pair. Figure 5.10 shows that the error in $\dot{x}(t)$ is on the order of 10^{-5}, while further increasing Δt would result in (RS, explicit) not solving some of the sequences listed here. We conclude that within this range of Δt such that all the three pairs can solve these sequences, their error growth is comparable and small, since the fitting error between potential formulated friction and rate-and-state friction is already on the order of 10^{-4}. For the sequences that (RS, explicit) cannot solve, further decreasing the time step to $\Delta t = 2^{-19} \approx 10^{-6}$ s still will not solve them, while further decreasing Δt is of little practical value since that is close to the precision of float tensors on GPUs.

Detailed error can be found in Table D.1 and D.2.

5.5 Conclusions

In this study, we have developed a potential-formulated friction that resembles the widely-used rate-and-state friction law. By constructing the potentials using Recurrent Neural Operators (RNOs) and training them on generated rate-and-state slip-friction sequences, we have verified that the potential friction formulation can capture the history dependencies well in rate-and-state friction, which is widely observed from experimental data. This suggests that there exists a potential-formulated friction law of our specific form that approximates the empirical rate-and-state friction well, with a relative L_2 error in friction coefficient of 2×10^{-4}. This is 2 orders of magnitude lower than the error between the best rate-and-state friction fit to real experimental data, which implies that they likely will fit the experimental data similarly well. We testify through different training runs that in our potential formulation, hidden variable ξ is unique up to affine transformations.

We have also confirmed by solving spring-slider systems that the potential friction formulation can facilitate implicit solution of initial value problems with rate-and-state frictional interfaces, since the propagation of solution to the next time step can be written as a convex minimization problem. We test whether or not the proposed potential formulation facilitates implicit solution of initial value problems by solving spring-slider dynamic problems under displacement-control loading. We sample 77 sequences with different spring constants and loading, and out of them rate-and-state friction cannot solve over 50% of the sequences with implicit solver, 46% of the sequences with explicit solver. While potential-formulated friction can solve all of these sequences, with either implicit or explicit solver. For the explicit solver, rate-and-state friction still cannot solve those sequences with a time step $1/256$ of that of the potential-formulated friction. (2^{-19} vs 2^{-11} s). Within the sequences that both explicit rate-and-state and implicit potential friction can solve, they achieve similar accuracy as time step increases.

With all the advantages of the potential formulation for rate-and-state friction, there is one drawback worth mentioning. The potentials require a large number of sequences in the training dataset to achieve good test error. Since compared to the original rate-and-state friction law, there are much more parameters in the potentials from their Neural Network structure, hundreds of sequences are required to avoid over-fitting and achieve good test error. In practice, it is sometimes difficult to obtain hundreds of sequences from experiments done on the same frictional interface, while the original rate-and-state friction law in general requires a handful of sequences to fit the four parameters.

In the future, we would work on finding closed-form approximations to the learnt potentials, such that taking their gradients can be done more time-efficiently. Right now since the potentials are still neural networks, the differentiation process is time consuming. We would work on fitting the potential formulations directly to experimental measurements and compare the fitting error with the original rate-and-state formulation.

References

[1] T. Akiba et al. *Optuna: A Next-generation Hyperparameter Optimization Framework*. 2019. arXiv: `1907.10902 [cs.LG]`.

[2] K. Bhattacharya et al. "Learning Markovian homogenized models in viscoelasticity." In: *Multiscale Modeling & Simulation* 21.2 (2023), pp. 641–679. DOI: `10.1137/22M1499200`. eprint: `https://doi.org/10.1137/22M1499200`.

[3] R. T. Q. Chen. *torchdiffeq*. 2018. URL: `https://github.com/rtqichen/torchdiffeq`.

[4] J. Dieterich. "Modeling of rock friction .1. experimental results and constitutive equations." In: *Journal of Geophysical Research* 84.NB5 (1979), pp. 2161–2168. ISSN: 0148-0227. DOI: `10.1029/JB084iB05p02161`.

[5] J.-C. Gu et al. "Slip motion and stability of a single degree of freedom elastic system with rate and state dependent friction." In: *Journal of the Mechanics and Physics of Solids* 32.3 (1984), pp. 167–196. ISSN: 0022-5096. DOI: `10.1016/0022-5096(84)90007-3`.

[6] B. Liu et al. "Learning macroscopic internal variables and history dependence from microscopic models." In: *Journal of the Mechanics and Physics of Solids* 178 (2023), p. 105329. ISSN: 0022-5096. DOI: `10.1016/j.jmps.2023.105329`.

[7] C. Marone. "Laboratory-derived friction laws and their application to seismic faulting." In: *Annual Review of Earth and Planetary Sciences* 26 (1998), pp. 643–696. ISSN: 0084-6597. DOI: `10.1146/annurev.earth.26.1.643`.

[8] A. Paszke et al. *PyTorch: An Imperative Style, High-Performance Deep Learning Library*. 2019. arXiv: `1912.01703 [cs.LG]`.

[9] J. Rice and A. Ruina. "Stability of steady friction slipping." In: *Journal of Applied Mechanics-Transactions of the ASME* 50.2 (1983), pp. 343–349. ISSN: 0021-8936. DOI: `10.1115/1.3167042`.

[10] A. Ruina. “Slip instability and state variable friction laws.” In: *Journal of Geophysical Research* 88.NB12 (1983), pp. 359–370. ISSN: 0148-0227. DOI: `10.1029/JB088iB12p10359`.

[11] C. H. Scholz. *The Mechanics of Earthquakes and Faulting*. 3rd ed. Cambridge University Press, 2019. DOI: `10.1017/9781316681473`.

Chapter 6

CONCLUSIONS AND FUTURE WORK

6.1 Summary of findings

Rate-and-state friction has been widely used In this thesis, we investigate various factors that affect the stability of frictional fault slip, under different scenarios such as fluid injection and laboratory earthquakes, with different numerical methods of Boundary Integral method and Finite Element method. In Chapter 2 we present a Boundary Integral method applicable to frictional problems over a fault embedded in plane-strain linear poroelastic solid. We develop a code implementation of a rate-and-state frictional fault that also incorporates inelastic dilatancy and fluid transport both within the fault shear layer and outside into the surrounding poroelastic bulk. We apply the code to model a fluid injection problem motivated by injection data from a previous field experiment. We explore the role of poroelastic and diffusion properties of the bulk both with and without inelastic dilatancy of the fault shear layer. We find that the diffusion and poroelastic properties can qualitatively affect the stability and propagation of fault slip. Furthermore, the stabilization by bulk diffusion and poroelastic properties can be comparable to the stabilizing dilatancy mechanism. In Chapter 3 we apply and further develop the boundary integral code for frictional fault slip to allow for the comparison between poroelastic bulk and purely elastic, permeable bulk with the same fluid transport properties. We find that poroelastic bulk stabilizes fault slip under fluid injection, when compared with elastic bulk with the drained Poisson's ratio. We also find that with typical length scales and properties of natural faults, as well as typical injection scale, poroelastic and elastic bulk with undrained Poisson's ratio have similar effects on the stability of dynamic fault slip. Besides, we find that the fault healing extent, or initial slip rate under rate-and-state friction affects the stability of fault slip significantly, which is consistent with previous studies. We also find that for mass-controlled injection at constant injection rate, higher injection rate leads to earlier and more frequent occurrences of dynamic events. However, these events have smaller spatial extent. Motivated by that, we further modify the injection rate from constant to intermittent in time, and find that with the same average injection rate and total injected mass of fluid, intermittent injection also leads to earlier, more frequent but more spatially restricted dynamic events.

In Chapter 4, we develop a 3D dynamic finite element model for simulating rupture propagation in pre-existing fault interfaces embedded in elastic bulk. We implement a modified fault constitutive model with both rate-and-state friction and flash heating dynamic weakening mechanism. Through modeling of the laboratory earthquake in a previous experimental study, we find that velocity-strengthening fault gouge equipped with flash-heating mechanism can reproduce qualitatively the observations in the experiment, in which the first rupture is arrested and later a second rupture can propagate in the gouge zone at dynamic slip rates. However, to achieve the experimentally observed self-nucleation at the specific spot, we have to introduce a weakening-healing patch locally there. Physically this suggests that at the nucleation spot there is possibly shear-localization and de-localization processes due to the complicated behavior of gouge particles Besides, we also find that the rupture behavior is significantly dependent on the initial slip rate of the fault.

After noticing the difficulties in implicit solution of dynamic problems with rate-and-state friction, in Chapter 5 we present a potential formulation for rate-and-state friction, under with the incremental implicit solution is equivalent to a convex minimization problem, which is easier to solve. By constructing the potentials using Re- current Neural Operators (RNOs) and training them on generated rate-and-state slip-friction sequences, we have verified that the potential friction formulation can capture the history dependencies well in rate-and-state friction, which is widely observed from experimental data. This suggests that there exists a potential-formulated friction law of our specific form that approximates the empirical rate-and-state friction well, with a relative L_2 error in friction coefficient of 2×10^{-4}. This is 2 orders of magnitude lower than the error between the best rate-and-state friction fit to real experimental data, which implies that they likely will fit the experimental data similarly well. We have also confirmed by solving spring-slider systems that the potential friction formulation can facilitate implicit solution of initial value problems with rate-and- state frictional interfaces. The one major drawback of the potential formulation is that it requires a large number of sequences in the training dataset to achieve good test error.

6.2 Future directions

This thesis presents numerical modeling of frictional fault slip with rate-and-state friction in various scenarios, including fluid injection into fault embedded in poroelastic solid and laboratory earthquakes propagating into fault gouge, and have discussed a series of factors that affects the stability of dynamic frictional fault slip.

However, there are still several areas where continued development is necessary. For the developed Boundary Integral method of frictional fault slip in poroelastic solid, still a further numerical parametric study is needed to fully characterize the different stability regimes, especially on the poroelastic properties of the bulk material, as well as different configurations of the relationship between bulk and fault diffusivities, both with and without inelastic dilatancy in the fault shear layer. Besides, alternative representations of the fault shear layer that assumes localization of slip instead of distributive slip along the thickness are also worth exploring. For a given average injection flux, it is worth exploring the optimal injection flux - time profile, to achieve an objective of more stable, less destructive dynamic fault slip.

For modeling laboratory earthquakes over frictional interfaces, a more complicated fault constitutive model with flash heating and rate-and-state parameters evolving with the slip history will be more likely to capture the shear-localization phenomenon and also re-nucleate a dynamic rupture.

To better apply the potential formulation for rate-and-state friction, it is necessary to find closed-form approximations to the learnt potentials, such that taking their gradients can be done more time-efficiently. The closed-form potentials should have fewer parameters to fit than the RNOs, and thus require fewer sequences for the training or fitting process. Another direction worth exploring is to directly fit the potential formulation to experimental data, and compare the fitting results with those from the original rate-and-state friction.

BIBLIOGRAPHY

[1] A. H.-D. Cheng. *Poroelasticity.* Vol. 877. Springer, 2016.

[2] E. Detournay and A. H.-D. Cheng. “Fundamentals of poroelasticity.” In: *Analysis and Design Methods.* Elsevier, 1995, pp. 113–171.

[3] E. R. Heimisson. “Crack to pulse transition and magnitude statistics during earthquake cycles on a self-similar rough fault”. In: *Earth and Planetary Science Letters* 537 (2020), p. 116202. ISSN: 0012-821X. DOI: `https://doi.org/10.1016/j.epsl.2020.116202`.

[4] E. R. Heimisson. *eliasrh/Poro_SBIM: Poro_SBIM_v1.0.* Version v1.0. Feb. 2022. DOI: `10.5281/zenodo.6010353`. URL: `https://doi.org/10.5281/zenodo.6010353`.

[5] E. R. Heimisson, E. M. Dunham, and M. Almquist. “Poroelastic effects destabilize mildly rate-strengthening friction to generate stable slow slip pulses.” In: *Journal of the Mechanics and Physics of Solids* (2019). DOI: `10.1016/j.jmps.2019.06.007`.

[6] E. R. Heimisson, J. Rudnicki, and N. Lapusta. “Dilatancy and Compaction of a Rate-and-State Fault in a Poroelastic Medium: Linearized Stability Analysis.” In: *Journal of Geophysical Research: Solid Earth* 126.8 (2021), e2021JB022071. DOI: `https://doi.org/10.1029/2021JB022071`.

[7] Y. Kaneko, J.-P. Ampuero, and N. Lapusta. “Spectral-element simulations of long-term fault slip: Effect of low-rigidity layers on earthquake-cycle dynamics.” In: *Journal of Geophysical Research: Solid Earth* 116.B10 (2011). DOI: `https://doi.org/10.1029/2011JB008395`.

[8] N. Lapusta et al. “Elastodynamic analysis for slow tectonic loading with spontaneous rupture episodes on faults with rate- and state-dependent friction.” In: *Journal of Geophysical Research: Solid Earth* 105.B10 (2000), pp. 23765–23789. DOI: `https://doi.org/10.1029/2000JB900250`.

[9] S. Larochelle et al. “Constraining Fault Friction and Stability With Fluid-Injection Field Experiments.” In: *Geophysical Research Letters* 48.10 (2021), e2020GL091188. DOI: `https://doi.org/10.1029/2020GL091188`.

[10] M. F. Linker and J. H. Dieterich. “Effects of variable normal stress on rock friction: Observations and constitutive equations.” In: *Journal of Geophysical Research: Solid Earth* 97.B4 (1992), pp. 4923–4940. ISSN: 2156-2202. DOI: `10.1029/92JB00017`.

[11] V. Rubino, N. Lapusta, and A. J. Rosakis. “Intermittent lab earthquakes in dynamically weakening fault gouge.” In: *Nature* 606.7916 (June 2022), pp. 922–929. DOI: `10.1038/s41586-022-04749-3`.

[12] P. Segall and J. R. Rice. "Dilatancy, compaction, and slip instability of a fluid-infiltrated fault." In: *Journal of Geophysical Research: Solid Earth* 100.B11 (1995), pp. 22155–22171. DOI: `10.1029/95JB02403`.

[13] Y. Song and J. W. Rudnicki. "Plane-Strain shear dislocation on a leaky plane in a poroelastic solid." In: *Journal of Applied Mechanics* 84.2 (2017), p. 021008.

[14] A. Talbot. "The Accurate Numerical Inversion of Laplace Transforms". In: *IMA Journal of Applied Mathematics* 23.1 (Jan. 1979), pp. 97–120. ISSN: 0272-4960. DOI: `10.1093/imamat/23.1.97`.

[15] K. Torberntsson et al. "A finite difference method for earthquake sequences in poroelastic solids". In: *Computational Geosciences* 22.5 (July 2018), pp. 1351–1370. ISSN: 1573-1499. DOI: `10.1007/s10596-018-9757-1`.

Appendix A

APPENDIX FOR CHAPTER 2

A.1 Parameter values

Here we briefly explain how the parameter values, listed in the table below, are set. Parameters G, ν, and all friction and loading parameters in Table A.1 are from [9]. Compressibilities $\beta_f^p, \beta_f^\sigma, \beta_n^p, \beta_n^\sigma, \beta_g^p, \beta_g^\sigma$ in addition to ϕ_0 and ϵ are selected as in [6] and listed in Table A.1. The compressibilities quantify the change in densities and void volume around a reference state. For example in Equation (2.22), we use ρ_f, but we wish to understand how the density changes with pressure and normal stress, so we expand the fluid density around a reference state $\rho_f = \rho_{f0}$ and $\sigma = \sigma_0$. We write $\rho_f = \rho_{f0} + \rho_{f0}(\beta_f^p p + \beta_f^\sigma \sigma)$ where $\beta_f^p = \frac{1}{\rho_{f0}}(\frac{\partial \rho_f}{\partial p})|_{\rho_f=\rho_{f0},\sigma=\sigma_0}$ and thus represents normalized change in fluid density when pore-fluid pressure is changed at the reference state but at fixed normal stress. Similarly $\beta_f^\sigma = \frac{1}{\rho_{f0}}(\frac{\partial \rho_f}{\partial \sigma})|_{\rho_f=\rho_{f0},p=p_0}$ represents change in fluid density from uniaxial normal stress change, but at the fixed equilibrium background pore pressure p_0. We note that fluid density is changed by normal stress because the normal stress changes the pressure. This can be seen in poroelasticity in the so-called Terzaghi's Consolidation Problem, e.g., [1]. Thus an alternative way here would be to relate pressure change to change in normal stress and work only with β_f^p but introduce another equation for how $\dot{p}$ depends on σ. After linearizing, the two approaches lead to a mathematically identical model. Through equivalent linearization as for the fluid density, we can obtain the compressibilities of the void volume as $\beta_n^p = \frac{1}{\phi_0}(\frac{\partial n}{\partial p})|_{n=\phi_0,\sigma=\sigma_0}$ and $\beta_n^\sigma = \frac{1}{\phi_0}(\frac{\partial n}{\partial \sigma})|_{n=\phi_0,p=p_0}$. Again through equivalent linearization, the compressibilities of the intact gouge material are $\beta_f^p = \frac{1}{\rho_{g0}}(\frac{\partial \rho_g}{\partial p})|_{\rho_g=\rho_{g0},p=p_0}$ and $\beta_f^\sigma = \frac{1}{\rho_{g0}}(\frac{\partial \rho_g}{\partial \sigma})|_{\rho_g=\rho_{g0},\sigma=\sigma_0}$.

We compute uniaxial compressibilities by multiplying the isotropic compressibilities by a factor of 5/9, which is only true for linear elastic material. As the stability analysis of [6] indicated, the uniaxial compressibilities become important for much thicker shear zones than we explored here. This is seen in how they only show up in correction factors to the stability metrics that scale with layer thickness. Thus, in application to problems with thick shear zones, a more careful determination of these compressibilities might be warranted.

Skempton's coefficient B is fixed and set to 0.85. This value is representative of Westerly granite as well as certain types of sandstone and other rocks. The undrained Poisson's ratio is, on one hand, set to 0.35 to reflect the approximate value of Westerly granite and on the other hand to 0.262 to represent the undrained value of Charcoal granite. We note that Charcoal granite has $\nu = 0.270$ and $\nu_u = 0.292$ [1]. However, we wish to fix ν such that we do not have multiple parameters varying each simulation. Thus only the range $\nu_u - \nu$ is the same as for Charcoal granite albeit the Poisson's ratios are similar in absolute terms. Further, Charcoal granite has a substantially lower Skempton's coefficient $B = 0.454$, but we still use $B = 0.85$ again to limit the number of varying parameters. We, therefore, do not recommend using this paper as a reference for poroelastic parameters, but rather look at the overview of [2, 1], which we used, and references therein for more information on error and methods for measuring. Here we simply want to explore two cases where $\nu_u - \nu$ are small and large, but at the same time make sure that the ranges reflect real values measured in rocks.

As explained in the main text, the range of the dilatancy coefficient is selected to reflect three different styles of ruptures. First we set $\gamma = 0$ and $\gamma = 1.7 \cdot 10^{-4}$ as trial values where the latter is the standard value used and was identified by [12]. We observe that the two values would typically render either highly unstable or very stable slip. Thus the value of $\gamma = 1.7 \cdot 10^{-5}$ is used to consider an intermediate regime, and shown to produce sustained slow slip migration.

The two mobilities κ_{cx}, κ_{cy} and the bulk hydraulic diffusivity c are determined by trial and error to approximately match the pore pressure evolution in [9]. We highlight that due to the heterogeneous permeability structure, the fact that we treat the pore pressure as non-constant in the shear zone, and other coupling mechanisms that alter the pore pressure, we cannot simply select parameters that give exactly the same pore pressure evolution as in [9].

Table A.1: Parameter values in the study

Symbol	Description	Value
Bulk and gouge material properties		
G	Shear modulus	10 GPa
B	Skempton's coefficient	0.85
ν	Drained Poisson's ratio	0.24
ν_u	Undrained Poisson's ratio	0.35, 0.262
β_f^p,β_f^σ	Isotropic and uniaxial fluid compressibility	$0.44 \cdot 10^{-9}$ Pa^{-1}, $0.24 \cdot 10^{-9}$ Pa^{-1},
β_n^p,β_n^σ	Isotropic and uniaxial pore volume compressibility	$6.0 \cdot 10^{-9}$ Pa^{-1}, $3.3 \cdot 10^{-9}$ Pa^{-1},
β_g^p,β_g^σ	Isotropic and uniaxial solid gouge compressibility	$0.020 \cdot 10^{-9}$ Pa^{-1}, $0.011 \cdot 10^{-9}$ Pa^{-1},
ϕ_0	Reference porosity	0.068
γ	Diltancy coefficient [12]	0, $1.7{\cdot}10^{-5}$, $1.7{\cdot}10^{-4}$
ϵ	Shear-zone half thickness	1.0 mm
c	Bulk hydraulic diffusivity	$4{\cdot}10^{-8}$, $4{\cdot}10^{-7}$ m^2/s
κ_{cx}	Along shear-zone mobility	$8.7584{\cdot}10^{-11}$ m^2/(Pa s)
κ_{cy}	Across shear-zone mobility	$8.7584{\cdot}10^{-20}$ m^2/(Pa s)
Friction and loading parameters		
D_{RS}	Characteristic state evolution distance	16.75 μm
a	Direct rate dependence of friction	0.01125
b	State dependence of friction	0.016
α_{LD}	[10] constant	0.0
V_0	reference slip rate	10^{-6} m/s
f_0	reference friction	0.55
τ_0	Initial shear stress	2.15 MPa
σ_0	Initial effective normal stress	4 MPa

A.2 Time-stepping

Here we describe the time-stepping scheme to simulate slow and fast slip with dilatancy and fluid injection into the faults. The scheme builds on the predictor-corrector schemes of [8] and [3]. However, several significant modifications have been introduced to resolve fluid diffusion. Below we shall describe the stages of a single time-step by the algorithm. We also refer the reader to the source code [4] for a more explicit implementation of the time-stepping scheme.

1. Initial explicit Euler prediction is made for time $t^{n+1} = t^n + \Delta t$ for δ_x^*, δ_y^*, p_c^*, V^*, where the asterisk represents the prediction of the next time-step.

2. Fourier coefficients are computed corresponding to the prediction values δ_x^*, δ_y^*, p_c^*, that is $D_{x,n}^*$, $D_{y,n}^*$, P_n^* using a Fast-Fourier Transform (FFT).

3. Using equations (2.52), (2.54), and (2.55) the Fourier coefficients for changes

in shear stress, normal stress and boundary pore pressure are computed and an inverse FFT is used to sum all Fourier modes.

4. Prediction for shear stress τ^* and effective normal stress $(\sigma - p)^*$ is computed. In the results, we use the average pore pressure $\langle p \rangle$; however, we note that p could here represent any number of pore pressure values, e.g. $p^\pm$ or p_c, depending on what assumptions are made about the relevant pore pressure in the shear localization region. In our numerical implementation [4], the user sets which pore pressure to use.

5. Prediction of the updated state-variable is computed using the analytical integration of the aging law by [7] which assumes constant slip speed from t to $t + \Delta t$

$$\theta^* = \theta^p \exp\left(-\frac{\Delta t}{2D_{RS}}(V^n + V^*)\right) + \frac{2D_{RS}}{(V^n + V^*)}\left(1 - \exp\left(-\frac{\Delta t}{2D_{RS}}(V^n + V^*)\right)\right), \tag{A.1}$$

where we have taken the slip speed as the average $(V^p + V^*)/2$ between the slip speed at time t^n and $t^{n+1} = t^n + \Delta t$. Here we use the superscript ^{n} to represent the fields at the previous time step, that is at time t^n.

6. Via an algebraic manipulation of the rate-and-state friction law (2.17) and (2.19) a correction for the slip speed is computed

$$V^{**} = 2V_0 \sinh\left(\frac{\tau^* - \eta V^*}{a(\sigma - p)^*} \exp\left(-f_0/a - \frac{b}{a}\log(V_0\theta^*/D_{RS})\right)\right). \tag{A.2}$$

However, for locations along the fault where the slip speed exceeds a threshold value (here set to 1 cm/s) the previous expression is found to lead to numerical dispersion and the slip speed is obtained by solving the following non-linear equation as done by [3]:

$$\left|V^{**} - 2V_0 \sinh\left(\frac{\tau^* - \eta V^*}{a(\sigma - p)^*} \exp\left(-f_0/a - \frac{b}{a}\log(V_0\theta^*/D_{RS})\right)\right)\right| = 0. \tag{A.3}$$

7. Using the new slip speed correction V^{**} the state variable is also updated

$$\theta^{**} = \theta^p \exp\left(-\frac{\Delta t}{2D_{RS}}(V^n + V^{**})\right) + \frac{2D_{RS}}{(V^n + V^{**})}\left(1 - \exp\left(-\frac{\Delta t}{2D_{RS}}(V^n + V^{**})\right)\right), \tag{A.4}$$

and from equation (2.27) $\langle \phi \rangle_{pl}^{**}$ is computed using θ^{**}.

8. Updating p_c: for the sake of brevity, we will only refer to the code [4], see also data availability statement, for a detailed implementation of this time-step, but a summary follows. In equation (2.28) (after substituting with equation (2.18) for $\langle p \rangle$) we approximate the $\partial^2/\partial x^2$ derivative with second-order finite difference approximation. The time-integral is discretized using a trapezoidal rule. Predictions from step 1 and 3 are used to compute the various fields at time t^{n+1} except we solve for p_c^{**} (the prediction of p_c for time t^{n+1}) implicitly by solving a system of linear equations.

9. Finally p_c^{**} is used to update δ_y^{**}, $\langle p \rangle^{**}$, and $\delta_x^{**} = \delta_x^n + \Delta t(V^n + V^{**})/2$.

After the steps above, the algorithm determines if it will proceed to the next time-step or reiterate following these rules.

- A minimum of one iteration is used. If the algorithm finishes the aforementioned steps for the first time at the current time then it must iterate again. The algorithm moves back to step 1, but instead of explicit guesses for the new time step it uses previous updates. That is $\delta_x^{**} \to \delta_x^*$, $\delta_y^{**} \to \delta_y^*$, and $p_c^{**} \to p_c^*$.

- If a minimum one iteration has been done, the algorithm checks for absolute and relative error in the estimate of p_c. That is if $\max(|p_c^{**} - p_c^*|)/(a\sigma_0) > \xi/10$ (where a is the direct effect parameter) or $||p_c^{**} - p_c^*||_1/||p_c||_1 > \xi/10$ is violated then a new time-step is selected $\Delta t \to \Delta t/2$ and the algorithm proceeds to step 1 using the following initial predictions $(\delta_x^{**} + \delta_x^n)/2 \to \delta_x^*$, $(\delta_y^{**} + \delta_y^n)/2 \to \delta_y^*$, and $(p_c^{**} + p_c^n)/2 \to p_c^*$. Here ξ is a factor that controls the accuracy of the solution, in simulations shown later this is set to $\xi = 1/32$, see Appendix C for more discussion of ξ.

- If both a minimum of one iteration has been carried out and the error tolerances are satisfied, the algorithm proceeds to a new time step and ** predictions are assigned as field values are time t^{n+1}. Finally, the new initial time-step is selected $\Delta t \to \min(\xi V^{n+1}/D_{RS}, 1.1 \cdot \Delta t)$ where first we make sure that the state evolution is well resolved, by picking ξ sufficiently small. Second, we make sure not to grow the time-step too much if the pore pressure evolution requires a smaller time-step than indicated by $\xi V^{n+1}/D_{RS}$.

A.3 Method validation

The spectral boundary-integral method, in addition to the rate-and-state fault slip simulations, couples together several physical processes that could not be simulated with another individual code. Further, no analytical solutions are available that also couple all these processes. It is, therefore, nearly impossible to benchmark and test all capabilities of the code and implementation simultaneously. However, here we list to provide an overview of the tests and validation we carried out.

- As was reported in Figure 2.2 the SBI solutions for τ' and $p^{\pm}$ were tested against the solutions of [13].
- The analytical inversion of the Laplace transform was in all cases tested by also numerically inverting the Laplace transform numerically using the Talbot method [14]
- Using p^{+} as the relevant pore pressure when computing the effective normal stress, we reproduced the results of [5], which were done with a different code [15]. We, for example, reproduced the spontaneously occurring instabilities at mildly rate-strengthening friction that give rise to slow-slip pulses, which only occur in a limited parameter regime. Our results were consistent with the spatial dimension of the instabilities and the pulse propagation speeds as reported by [5].
- Using the linearized stability analysis of [6] we identified the critical wavenumber for many different regimes, such as high diffusivity, low diffusivity, intermediate diffusivity as well as thicker and thinner shear zones. In the code, a fully non-linear implementation, we induced a critical wavelength perturbation, as determined by the linearized analysis, by introducing a small perturbation in the initial state around steady-state sliding. We found in all cases that the perturbation in the slip speed oscillated without growing or decaying.

The tests and benchmarking above do validate most aspects of the implementation and method we have introduced in this paper. However, none test the injection into the fault and fluid propagation as a result of the injection. In order to check the robustness of the algorithm in this regard, we set up a problem with injection and delayed nucleation with dilatancy. The simulations are run until the slip speed reaches 1 cm/s, which we take as the instability time. This setup thus tests how well the pore pressure injection and subsequent diffusion is resolved as it promotes instability. We generate a manufactured solution with the error tolerance and state integration parameter set to $\xi = 1/4096$ (see section A.2). Then setting $\xi \in \{1/4, 1/8, 1/16, 1/32, 1/64\}$ and investigating the L_1 norm error of the manufactured solution and the less accurate solutions plotted against the total number of iterations (which scales with the computational time) we see a second-order convergence. Where we look at the time of instability, the slip speed profile at the instability time, the p_c value at the instability time, and the slip profile at that time. $\xi = 1/32$ roughly correspond to a relative error of 10^{-3} in all the fields we looked at, but we stress that the magnitude of the relative error depends on the problem and the simulation time. For simulations we favor using $\xi = 1/32$ and one minimum iteration (see section A.2 for discussion on iterations). If smaller values than $\xi = 1/64$ are compared to the manufactured solution, the convergence gets more complicated but tends to improve to the first order with the iteration number. Using no minimum iteration or 2 minimum iterations also works and gives consistent results. We suggest 1 minimum iteration is most efficient in terms of obtaining a stable convergent solution at the fewest total iterations.

Finally, we note that Figure 2.4c demonstrates, by chance, that the simulations are well resolved and accurate. A careful inspection of the figures shows that the last event is not one event but two events nucleating at exactly the same time around $x \approx \pm 30$ m and then coalescing. While such a high degree of symmetry is not physically realistic, it is a strong indication of well-resolved simulations in time and space, especially when it occurs not at the first simulated event. The same phenomenon also occurs in Figure 2.4b, but it is not as clear.

Appendix B

APPENDIX FOR CHAPTER 3

B.1 Values of material properties used in the simulations

G [GPa]	ν	α	M [GPa]	κ [$\mathrm{m}^2/(\mathrm{Pa}\cdot\mathrm{s})$]	c[m^2/s]
10	0.24	0.5530	0.35	2.1688×10^{-19}	1.0×10^{-8}

Table B.1: Linear poroelastic material properties of the bulk material

f_*	V_* [m/s]	a	b	D_{RS} [m]	κ_{cx} [$\mathrm{m}^2/(\mathrm{Pa}\cdot\mathrm{s})$]	κ_{cy} [$\mathrm{m}^2/(\mathrm{Pa}\cdot\mathrm{s})$]
0.55	1.0×10^{-6}	0.0112	0.0160	16.75×10^{-6}	8.75834×10^{-11}	8.75834×10^{-20}

Table B.2: Friction and diffusivity properties of the fault interface

Appendix C

APPENDIX FOR CHAPTER 4

C.1 Values of material properties used in the simulations

ρ [Kg/m^3]	G [GPa]	ν
1200	1.963	0.35

Table C.1: Linear elastic material properties of Homalite-100

f_*	V_* [m/s]	a	b	D_{RS} [m]	V_w [m/s]	f_w
0.58	1.0×10^{-6}	0.003	0.008	1.5×10^{-6}	0.2	0.33

Table C.2: Rate-and-state friction and flash heating properties of the Homalite-100 interface

Case	f_*	V_* [m/s]	a	b	D_{RS} [m]	V_w [m/s]	f_w	$V_{initial}$ [m/s]	$\theta_{initial}$ [s]
1	0.58	1.0×10^{-6}	0.003	0.008	1.5×10^{-6}	0.2	0.33	–	0.006
2	0.58	1.0×10^{-6}	0.016	0.002	1.5×10^{-6}	2.0	0.1	10^{-12}	–
3	0.58	1.0×10^{-6}	0.016	0.002	1.5×10^{-6}	2.0	0.1	10^{-11}	–
4	0.58	1.0×10^{-6}	0.016	0.002	1.5×10^{-6}	2.0	0.1	10^{-10}	–
5	0.58	1.0×10^{-6}	0.016	0.002	1.5×10^{-6}	2.0	0.1	10^{-9}	–
6	0.58	1.0×10^{-6}	0.016	0.002	1.5×10^{-6}	–	–	10^{-9}	–
7	0.58	1.0×10^{-6}	0.016	0.002	1.5×10^{-6}	2.0	0.1	–	10^{6}
8	0.58	1.0×10^{-6}	0.016	0.002	1.5×10^{-6}	2.0	0.1	–	10^{6}

Table C.3: Rate-and-state friction, flash heating properties and initial condition of the Fault gouge region vs. Cases. $V_{initial}$ and $\theta_{initial}$ are dependent on each other so only one should be specified for each case.

Appendix D

APPENDIX FOR CHAPTER 5

D.1 Supplementary figures and tables

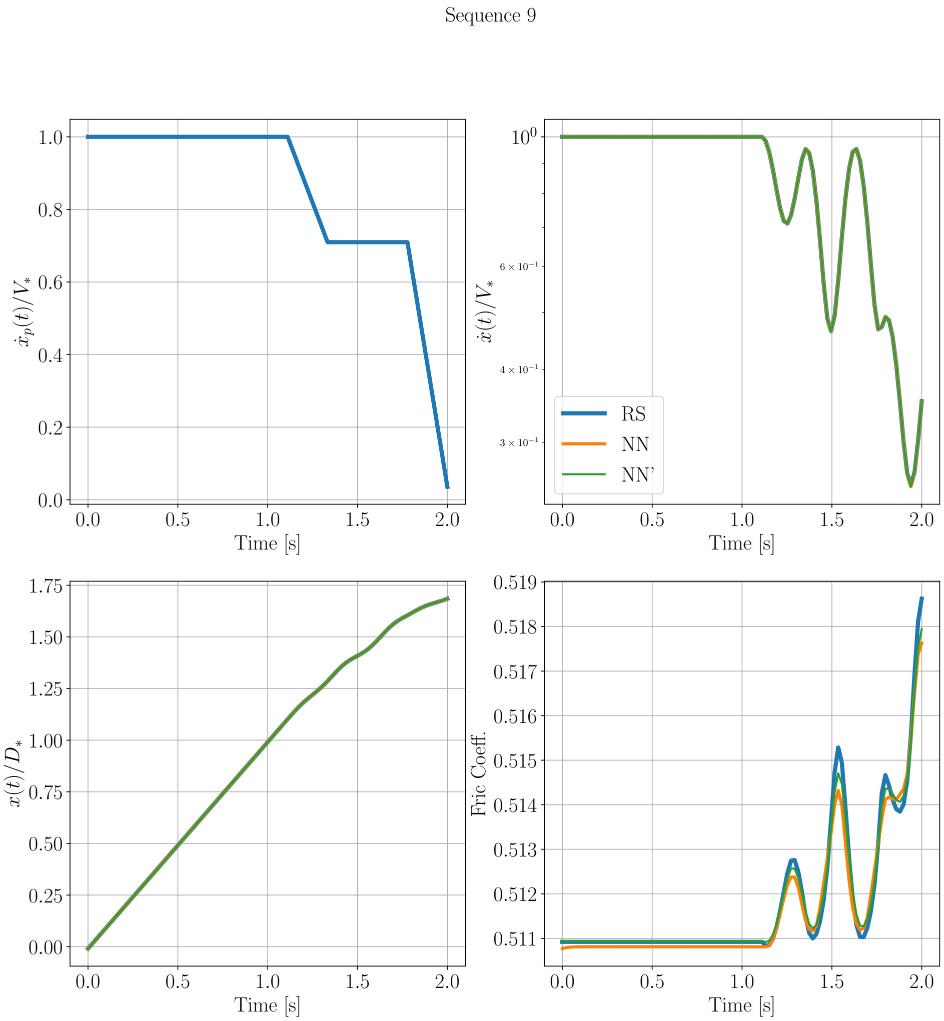

Figure D.1: An example sequence of spring-slider solution with original rate-and-state friction, NN potentials, and NN potentials further trained on spring-slider sequences

Δt [s]	$2^{-13.5}$	$2^{-13.0}$	$2^{-12.5}$	$2^{-12.0}$	$2^{-11.5}$	$2^{-11.0}$
NN, implicit	5.993e-06	3.636e-06	4.807e-06	4.716e-06	6.282e-06	8.508e-06
NN, explicit	6.130e-06	3.808e-06	4.786e-06	4.397e-06	5.968e-06	7.795e-06
RS, implicit	nan	nan	nan	nan	nan	nan
RS, explicit	7.321e-06	4.447e-06	5.267e-06	4.426e-06	6.464e-06	8.069e-06

Table D.1: Mean relative L_2 error in $\dot{x}(t)$ averaged over 77 sequences, for NN, RS models with implicit, explicit solvers.

Δt [s]	$2^{-13.5}$	$2^{-13.0}$	$2^{-12.5}$	$2^{-12.0}$	$2^{-11.5}$	$2^{-11.0}$
NN, implicit	5.799e-06	5.390e-06	5.575e-06	7.069e-06	6.384e-06	1.033e-05
NN, explicit	6.241e-06	5.766e-06	5.844e-06	6.887e-06	6.572e-06	9.639e-06
RS, implicit	nan	nan	nan	nan	nan	nan
RS, explicit	9.601e-06	6.886e-06	5.541e-06	5.597e-06	6.845e-06	1.017e-05

Table D.2: Standard deviation of relative L_2 error in $\dot{x}(t)$ over 77 sequences, for NN, RS models with implicit, explicit solvers.

INDEX

POCKET MATERIAL: MAP OF CASE STUDY SOLAR SYSTEMS